AN EXPERIMENTAL INVESTIGATION OF NEWTONIAN AND NON-NEWTONIAN SPRAY INTERACTION WITH A MOVING SURFACE

by

Daniel Mervin Dressler

B.A.Sc., University of Saskatchewan, 2003

A THESIS SUBMITTED IN PARTIAL FULFILMENT OF

THE REQUIREMENTS FOR THE DEGREE OF

MASTER OF APPLIED SCIENCE

in

The Faculty of Graduate Studies

(Mechanical Engineering)

THE UNIVERSITY OF BRITISH COLUMBIA

October 2006

© Daniel Mervin Dressler, 2006

Abstract

As a logical extension of previous work conducted into viscoelastic atomization, initially motivated by the need to improve spray coating transfer efficiencies, an experimental investigation into the spray-surface interaction for a number of Newtonian and non-Newtonian substitute test liquids is presented. Three model elastic liquids of varying polymer molecular weight and three inelastic liquids of varying shear viscosity were sprayed upon a moving surface to isolate the effect of elasticity and shear viscosity, respectively, on spray impaction behavior. In addition, two liquids exhibiting shear thinning behavior and an industrial top of rail liquid friction modifier, KELTRACK®, for use in the railroad industry, were included in the spray tests. High-speed photography was used to examine the impingement of these liquids on the surface.

Ligaments, formed as a consequence of a liquid's viscoelasticity, were observed impacting the surface for 300K PEO, 1000K PEO, and KELTRACK. These ligaments were broadly classified into four groups, based on their structure. Splashing of elastic liquid ligaments and droplets led to filamentary structures being expelled from the droplet periphery, which were then carried away by the atomizing air jet, leading to reductions in transfer efficiency. The effect of increasing elasticity amongst the three varying molecular weight elastic solutions was shown to increase the splash threshold; a similar effect was noted with increasing shear viscosity.

Attempts were made at quantifying a critical splash-deposition limit for all test liquids however due to imaging system limitations, no quantitative conclusions could be made.

For KELTRACK, both droplets and ligaments spread and deposited on the rail surface upon impact, with no observed splash or rebound. Splash was only noted when droplets impinged directly on a previously deposited liquid film and even then, splashing was well contained. Thus, KELTRACK's current rheological formulation proved to be very effective in ensuring high coating transfer efficiencies.

Table of Contents

Abstract ii
Table of Contents iii
List of Tables vii
List of Figures viii
List of Symbols x
Acknowledgements xii
Chapter 1: The Use and Application of Friction Modifiers in the Railway Industry 1
1.1 Introduction 1
1.2 Friction Control 2
1.3 Friction Modifiers 3
1.4 Application Methods of LFM's 4
1.5 Research Objectives 4
1.6 Summary 5
Chapter 2: Spray Impact on a Surface 7
2.1 Introduction 7
2.2 Spray Interaction with a Surface 8
2.3 Newtonian Droplet Impact 10
2.4 Non-Newtonian Effects 15
2.5 Droplet Impaction on a Moving Surface 17
2.6 Summary 18
Chapter 3:Experimental Setup and Methodology 20
3.1 Linear Traverse 20
3.2 Projectile Surface 22
3.3 Spray Setup 23
3.4 Test Liquids 24
3.5 Imaging Setup 29
3.6 Summary 31
Chapter 4: Experimental Results and Discussion 33
4.1 Spray Impact Analysis 33
4.1.1 Impinging Droplet Parameters 33
4.1.2 Splashing Considerations 36
4.1.3 Splashing Behavior of Inelastic Liquids 38

4.1.3.1 Distilled Water 39
4.1.3.2 50 wt. % Glycerin 39
4.1.3.3 80 wt. % Glycerin 40
4.1.3.4 Inelastic Splashing Conclusions 40
4.1.4 Splashing Behavior of Elastic Liquids 41
4.1.4.1 100K PEO 42
4.1.4.2 300K PEO 44
4.1.4.3 1000K PEO 45
4.1.4.4 Elastic Splashing Conclusions 45
4.1.5 Splashing Behavior of Shear-Thinning Liquids 46
4.1.5.1 Carbopol® 47
4.1.5.2 Xanthan Gum 48
4.1.5.3 Shear-Thinning Splashing Conclusions 48
4.1.6 KELTRACK 48
4.1.7 Spray Impact Conclusions 49
4.2 Viscoelastic Effects 50
4.2.1 Ligaments and Filamentary Structures 50
4.2.2 Ligament Classification 51
4.2.3 Ligament Impaction 53
4.2.3.1 KELTRACK 53
4.2.3.2 300K PEO 54
4.2.3.3 1000K PEO 55
4.2.4 Elastic Liquid Impingement Conclusions 58
4.3 Improvement of Transfer Efficiency 59
4.3.1 Introduction 59
4.3.2 Droplet Entrainment 59
4.3.2.1 Theoretical Determination of Entrained Droplet Size 59
4.3.2.2 Experimental Estimation of Entrained Droplet Size 60
4.3.3 Overspray 61
4.4 Spray Label Analysis 63
4.4.1 Methodology 63
4.4.2 Results 64
4.4.3 Discussion 66

4.4.4 Recommendations 67
4.5 Boundary Layer Analysis 67
4.6 Spray Pulsation Phenomenon 69
4.7 Effect of Nozzle Orientation 69
4.8 Uncertainty Analysis 70
Chapter 5: Conclusions 73
Chapter 6: Recommendations 75
References 76
Appendix A: Design of Linear Traverse 83
A.1 Design Options Considered 83
A.2 Angular Rotation Device 83
A.3 Theoretical Design of Linear Traverse 86
A.4 Sound Pressure Level Analysis of Linear Traverse 89
A.4.1 Purpose: 89
A.4.2 Equipment: 90
A.4.3 Test Procedure: 90
A.4.4 Sound Enclosure: 90
A.4.5 Data: 90
A.4.6 Analysis: 91
A.4.7 Conclusions: 92
A.4.8 Recommendations: 93
Appendix B: Experimental Testing Procedures 94
B.1 Preparing and Loading the Projectile Surface with Tail Plug 94
B.2 Preparing the Energy Dissipation Device 94
B.3 Computer Equipment and Imaging Setup 95
B.4 Photodiode Assembly and Oscilloscope Readings 96
B.5 Liquid Preparation 97
B.6 Filling the Linear Traverse Tank 98
B.7 Using the Atomizing Air 98
B.8 Firing the Linear Traverse 99
B.9 Linear Traverse Testing Brief Summary 99
B.10 Care and Maintenance 100
B.10.1 Projectile Surface 100

B.10.2 Tail Plug 101
B.10.3 Photodiode Assembly 102
B.10.4 PALLITE® VIII 102
B.10.5 Liquid Pump 103
B.10.6 Linear Traverse Tube 103
B.10.7 Nozzle 103
B.10.8 Energy Dissipation Device 103
Appendix C: Test Liquid Ink Addition Justification 104
Appendix D: Determination of Droplet Diameter and Velocity 107
D.1 Droplet Diameter 107
D.2 Droplet Velocity 112
D.3 Droplet Sizing MATLAB® Code 115
Appendix E: Spray Label Analysis MATLAB® Code 117

List of Tables

Table 2.1: Summary of the effect of various parameters on the six possible droplet impact outcomes [Reproduced from Rioboo *et al.* 2001] 15
Table 3.1: Compositions of test liquids at 25°C [Li *et al.* 2005] 26
Table 3.2: Shear-thinning liquid properties 28
Table 4.1: Impinging droplet parameter ranges 35
Table 4.2: Spray label test matrix 63
Table 4.3: Spray label analysis results 64
Table 4.4: Estimated ± uncertainties of measured variables 71
Table A.1: Linear traverse design summary 83
Table A.2: SPL measurements - no enclosure 91
Table A.3: SPL measurements - with enclosure 91

List of Figures

Figure 2.1: Six possible outcomes of droplet impact [Reproduced from Rioboo *et al.* 2001] 11
Figure 3.1: Linear traverse schematic 22
Figure 3.2: Projectile surface with tail plug 23
Figure 3.3: Plain-jet co-axial air-blast atomizer (w/o regular duckbill) 24
Figure 3.4: KELTRACK® shear viscosity [Li *et al.* 2005] 24
Figure 3.5: Carbopol® shear viscosity (baseline) 27
Figure 3.6: Xanthan gum shear viscosity 28
Figure 3.7: Horizontal imaging setup 30
Figure 3.8: Overhead imaging setup 31
Figure 4.1: Xanthan gum droplet impingement (for the droplet of interest: d = 144µm, U_{normal} = 16.6 m/s, We = 692) 34
Figure 4.2: Definition of the impact angle 36
Figure 4.3: Splashing of 100K PEO droplet with secondary droplet attached to parent drop via ligament 42
Figure 4.4: Frequency of droplet splash and corresponding threshold values 43
Figure 4.5: Effect of ink on Carbopol® shear curve 46
Figure 4.6: Breakup of xanthan gum 7.5 mm downstream of the nozzle 47
Figure 4.7: Breakup of Carbopol® 7.5 mm downstream of the nozzle 47
Figure 4.8: Breakup of a) 100K PEO b) 300K PEO c) 1000K PEO d) KELTRACK 51
(Photographs courtesy of Li *et al.* 2005) 51
Figure 4.9: KELTRACK ligament structures: a) beads-on-string b) bulbous tip 52
c) string d) membrane 52
Figure 4.10: KELTRACK bulbous tip ligament impaction 54
Figure 4.11: 300K PEO Ligament structures: a) bulbous tip b) beads-on-string 54
Figure 4.12: 300K PEO beads-on-string ligament impaction 55
Figure 4.13: 1000K PEO bulbous tip ligament impaction 56
Figure 4.14: Entrainment of 1000K PEO ligament tail upon impact 57
Figure 4.15: Breakup of 300K PEO beads-on-string ligament into discrete droplet 57
Figure 4.16: KELTRACK being applied to surface of rail 62
Figure 4.17: a) Sample image processed label b) far right c) right d) left e) far left 65
Figure A.1: Ratio of linear to centripetal acceleration as a function of droplet diameter 85

Figure A.2: Ratio of surface tension force to centripetal force as a function of droplet diameter 86
Figure A.3: Pressure in tanks A and B as a function of time 87
Figure A.4: Position and velocity as a function of time 87
Figure A.5: Exit velocity as a function of initial tank pressure for barrel lengths of 1m and 2m 88
Figure A.6: Velocity as a function of pressure for a barrel length of 2m 89
Figure A.7: Test locations 90
Figure C.1: Viscosity as a function of shear rate for water at 20°C 104
Figure C.2: Viscosity as a function of shear rate for 80 wt.% glycerin at 20°C 105
Figure C.3: Viscosity as a function of shear rate for 300K PEO at 20°C 105
Figure C.4: Viscosity as a function of shear rate for Carbopol® at 20°C 106
Figure D.1: Original image 107
Figure D.2: Inverted image 108
Figure D.3: Background estimation 108
Figure D.4: Background subtracted from image 109
Figure D.5: Cropping droplet of interest 109
Figure D.6: Inverted droplet 110
Figure D.7: Pixel intensities for droplets 111
Figure D.8: Image histogram 111
Figure D.9: Inverted droplet 112
Figure D.10: Setting the video scale 113
Figure D.11: Determination of impact angle 114

List of Symbols

μ	Liquid shear viscosity
μ_g	Viscosity of gas in which droplet travels
a	Vertical shift factor for elastic liquids
a_c	Centripetal acceleration
COF	Coefficient of friction
d	Droplet diameter
D	Characteristic dimension of obstacle for Stokes # calculation
e	Element of error
F_c	Centripetal force
F_{st}	Surface tension force
i	Index representing L different variables
j	Number of element of error
k	Consistency index
K_L	Splash threshold for Newtonian liquids
La	Laplace number
L_{ex}	Daily noise exposure level
m_{drop}	Mass of drop
M_v	Viscosity averaged molecular weight
n	Power-law index
Oh	Droplet impact Ohnesorge number
P_a	Pressure in tank A
P_b	Pressure in tank B
R	Dependent value comprised of measured variables
r	Radius of disk to be used in linear traverse design
R_d	Radius of droplet
Re	Droplet impact Reynolds number
Re_o	Droplet Reynolds number for Stokes # analysis
Re_x	Reynolds number for boundary layer analysis
R_{max}	Maximum spread radius
R_{nd}	Non-dimensional roughness
R_a	Mean roughness height
S	Stopping distance
Stk	Stokes number
U	Impact velocity
U_{normal}	Normal velocity component
U_o	Initial droplet velocity
u_R	Uncertainty of R
u_{x_i}	Uncertainty of measured variable
v	Linear velocity
We	Droplet impact Weber number

x	Length of flat plate in boundary layer analysis
x_i	Measured variable
α	Impact angle
δ	Boundary layer thickness
ζ	Spread factor
θ_i	Sensitivity index of R to x_i
π	Pi
ρ_g	Density of gas in which droplet travels
ρ_l	Density of liquid
σ	Surface tension
τ	Shear-stress
τ_o	Yield stress
τ_R	Relaxation time
ω	Angular rotation
$\dot{\gamma}$	Shear rate

Acknowledgements

I'll be the first to admit that this Master's degree, as I was warned when I began, was full of ups and downs. I'd also admit that at times, it felt like there were significantly more downs than ups, which was definitely a challenge in itself to learn to move past these downs. I did however manage to move forward and feel that I am a far better and more enlightened individual having been through these numerous ups and downs than if I had not experienced them.

I would have to say that I am hard pressed to find another experience in my life in a two-year time frame where I have experienced such profound growth and maturing, academically, personally, and socially. The strides that I have made in my engineering abilities and self-confidence is ten fold, in addition to significant enhancements in my interpersonal and communication skills. By far, the biggest asset that I have gained over the course of the past two years however was to learn how to truly independently think and "learn" for myself. For this, I give my academic supervisors, Dr. Martin Davy and Dr. Sheldon Green, the utmost gratitude for showing me the way to establishing such a valuable tool. I also owe significant gratitude to my supervisors for assisting and supporting me along the entire duration of the past twenty-four months.

I would like to thank a few people at Kelsan Technologies, particularly Dr. Don Eadie, Dave Elvidge, and John Cotter for their technical assistance throughout this project and for their insightful comments at our meetings.

A very special thanks goes out to Dr. Peter Cripton and his research group in the Department of Orthopedic Engineering Research, for allowing the use of their Phantom V9.0 camera when available for my purposes. Without the use of this camera, completion of this thesis would have been significantly more challenging, if not impossible. Similarly, I would also like to express my thanks to Dr. Steven Rogak and the combustion group for allowing the use of their PhantomV7.1 High Speed camera and associated equipment when available. I would like to thank Markus Fengler, Roland Genshorek, and Steve Carey in the departmental machine shop for all their patience, assistance, tool usage, engineering insight, and machining time in developing the linear traverse. A special thanks also goes out to Dr. Frigaard and the Complex Fluids Lab, particularly to Stefan Storey for his assistance in dealing with the rheometer and his non-Newtonian rheological insight, as well as for supplying me with multiple samples of both Carbopol® and xanthan gum solutions. A very special thanks goes out to John Kennah

for his time and effort in helping to develop the wooden projectile surface; it was very much appreciated. Special thanks also goes out to Larry Li and Seth Gilchrist, for their technical assistance and general support over the past two years, Murray Hodgson for use of his sound-pressure level meter, Tim Paterson for all his unabated help with the setup and commissioning of the linear traverse, M. Marengo, C. Tropea, and D. Sivakumar for their advice and technical assistance during my analysis, and finally to Erin Kennah, for her understanding and willingness to help out whenever possible throughout the last year.

I am also extremely grateful to my supervisors for allowing me the opportunity to travel to Japan to attend the ICLASS 2006 conference. The trip was an incredibly rewarding experience, both professionally and personally, and I feel very fortunate to having been able to attend. I would also like to thank ILASS-Americas for providing me with the Student Travel Stipend to assist in covering the financial expenses associated with attending this conference.

This project would not have been possible without financial assistance from our sponsors; thanks thus goes out to Kelsan Technologies Corporation, the National Sciences and Engineering Research Council of Canada, and Advanced Systems Institute.

Finally, I would like to say that I've realized a Master's degree is far more than just academic; it is a complete maturing and growing experience. The lifestyle that I now live here is one that I choose to stay with and the friendships and relationships I have established will be ones that will continue for many years. I have to say that the last two years have been the most exciting, busy, educational, and all-around best two years of my life. For that, I thank Martin and Sheldon for allowing me the opportunity to "learn" in this beautiful city.

Chapter 1

The Use and Application of Friction Modifiers in the Railway Industry

This chapter will give a brief background into the motivation for this thesis. The need for friction control in the railway industry will first be addressed, followed by background pertaining to past friction control methods. Friction modifiers (FM's) will then be introduced including benefits associated with using FM's, as well as methods of application. An industrial liquid FM, known as KELTRACK® HI-RAIL, the FM of focus for the present research, is also introduced. Finally, a discussion of the current research objectives will ensue, thus setting the stage for the next chapter outlining relevant literature pertaining to the questions at hand.

1.1 Introduction

The Canadian rail network, comprised of more than 72,000 kilometers of track and operating through five time zones [Cotter *et al.* 2005], annually transports more than 270 million tonnes of freight [Transport Canada]. Rail transport provides the most efficient and cost-effective form of freight transportation in North America [Transport Canada]. Freight transport constitutes only a small part of the railway industry in continents such as Asia and Europe, where a greater emphasis is placed on transit applications. This rapidly growing transit industry transports millions of commuters every day, establishing the commuter train as the primary form of transport in densely populated countries such as Japan. With rising fuel costs making truck and air transport increasingly less efficient and with a continuing increase in population density, railways will continue to increase their influence in the 21st century.

Due to this continuing strong economic and societal influence, ongoing research is being conducted by the railway industry into further improving the efficiency of rail transport and advancing railway technology. In the past decade alone, railways have reduced total fuel consumption by 5% and have increased their revenue tonne-kilometers per litre by 28% [Cotter *et al.* 2005]. As a result of this research, railroads have recognized that by using an integrated approach to effectively managing the wheel-rail interface, significant benefits such as controlling wheel and rail wear and reducing operating costs, can be obtained. As noted by Eadie *et al.* [2002], the three main focal points for effective management at the wheel-rail interface, most effective when

implemented together, are 1) proper selection and maintenance of wheel and rail profiles, 2) proper selection of grade and quality of wheel and rail metallurgy, and 3) effective control of friction. The effective control of friction has been in the past the least advanced of the three; however, in recent years, friction control technology has been emerging rapidly [Eadie *et al.* 2002].

1.2 Friction Control

Friction control in the past has primarily focused on the gauge face/flange, where grease or oil-based lubricants (grease is primarily used for freight applications whereas oil is typically used for transit applications) have been applied to reduce the coefficient of friction (COF) to a minimal value (COF < 0.2) [Eadie *et al.* 2002]. These hydrocarbon products are applied either through trackside (to the gauge face/corner) or on-board dispensing systems (to the wheel flange). However, these lubricants tend to migrate to or are flung to the top-of-rail (TOR), thus causing a low COF where an intermediate COF (0.2 < COF < 0.4) is required, an undesirable side effect [Chiddick and Eadie 1999]. In addition, the use of oil and grease can cause both cleanliness and environmental issues as these lubricants are flung from the rail face as the locomotive passes over.

Gauge face/flange lubrication was then taken to the next step with the development of solid stick lubricants, applied to the wheel flange by a constant force spring. This system solved the problem of lubricant migrating to the TOR surface due to the dry film nature of the lubricant [Eadie *et al.* 2002]. Although lubrication of the gauge face/flange is a mature technology, there are still areas left for improvement, particularly in the application area [Kalousek *et al.* 1997].

Recently, however, researchers have begun to refocus their efforts on TOR friction control. This is as expected as comprehensive friction management would encompass both gauge face/flange and TOR friction control. Although first employed more than fifteen years ago when it was discovered that TOR friction control significantly reduced fuel consumption [Eadie and Kalousek 2001], this is still a relatively new and emerging field as most of the world's railroads still operate today without TOR friction control [Eadie *et al.* 2002]. TOR friction management also provides a significant opportunity to reduce wheel and track wear [Kalousek *et al.* 1997].

Similarly as for gauge face/flange lubrication, grease-based lubricants were traditionally used. However, grease-based lubricants can reduce frictional levels but

cannot control them [Eadie and Kalousek 2001]. As Kalousek *et al.* [1997] noted, significant costs and adverse affects are associated with having too low or too high of COF [see also Chiddick and Eadie 1999]. Thus, it is desirable that an intermediate COF, $\mu \approx 0.35$, be maintained at the TOR surface; this intermediate value is crucial to the role of enhancing performance without compromising traction and braking [Eadie *et al.* 2001, 2002]. As a result of this requirement for an intermediate frictional level, friction modifiers (FM) have emerged.

1.3 Friction Modifiers

Friction modifiers exist either as solid sticks or as water-based solutions, with the latter denoted as liquid friction modifiers (LFM's), which contain suspended polymeric and solid composites [Eadie and Kalousek 2001]. By introducing these suspended solids with engineered frictional properties in appropriate quantities into the wheel/rail interface, the frictional characteristics of the layer between the wheel/rail interface, containing wear debris and contaminants, can be modified accordingly [Chiddick and Eadie 1999]. FM's are able to reduce, control, and maintain frictional levels at a specified optimal level over a given number of wheel/train passes, a significant advantage over hydrocarbon based lubricants [Eadie and Kalousek 2001].

Combined with the additional, above-mentioned components of an integrated wheel/rail management approach, the use of FM's has been proven to lead to substantial benefits. Of environmental importance, Cotter *et al.* [2005] found that with the use of a LFM on tracks with a curve density ranging from 25 to 51%, fuel consumption was reduced by 155 Liters/Million Ton-miles to 744 Liters/Millions Ton-miles. The associated reduction in greenhouse gas emissions (CO_2) ranged from 0.3 metric tonnes per million ton-miles to 2 metric tonnes per million ton-miles. With an industry which consumes over 2 billion litres of diesel fuel per year and with the Canadian Federal Government currently pressing the railroad industry for further GHG reductions [Cotter *et al.* 2005], this is of significant interest. In addition, noise generated when trains travel around corners, known as wheel-squeal, has been shown to be reduced with use of a LFM, typically by 10-15 dB, and up to as much as 20 dB. This is of great interest to railroads operating close to residential areas [Eadie *et al.* 2001, Chiddick and Eadie 1999], as well as to the residents themselves. Furthermore, the application of FM's can

lead to reductions in vibrations, lateral forces when curving, and both wheel and rail wear [Eadie *et al.* 2002, Eadie and Kalousek 2001].

Kelsan Technologies Corporation, located in North Vancouver, BC, is a leader in developing friction modifiers for the railway industry. They have developed a number of FM's for use in various applications where differing friction characteristics are required. Of particular interest, is a high positive friction LFM known as KELTRACK HI-RAIL. Due to the compositional nature of this friction modifier, it inherently exhibits non-Newtonian behavior. KELTRACK HI-RAIL will be discussed further in Chapter 3.

1.4 Application Methods of LFM's

As mentioned above, FM's exist either as solid-sticks or water-based liquids. Solid-stick FM's are typically applied to the wheel tread using a constant force spring. This type of FM, however, is not the focus of this investigation and therefore, will not be discussed further. Application techniques of LFM's, on the other hand, are still currently being investigated and developed. Significant effort into reliable and effective application of the liquid material on the TOR has been put forth; effective application is essential to realizing the full benefits of TOR friction control and to ensure cross contamination between gauge face and TOR, where low desired friction is in opposition with required intermediate friction, does not occur [Eadie *et al.* 2001, Kalousek *et al.* 1997].

LFM's can be dispensed onto the railhead through use of a wayside/trackside applicator, not to be discussed further, or through use of on-board spray systems mounted underneath locomotives, track maintenance vehicles known as Hi-Rail trucks [Eadie and Kalousek 2001], or more recently, freight wagons [Cotter *et al.* 2005]. Spray nozzles, typically airblast atomizers, are located 2-3" from the TOR surface and apply the liquid material to the surface by means of a fine, atomized spray so as to promote water evaporation and leave behind a thin, uniform film, similar to a coat of paint [Cotter *et al.* 2005]. This film can be effective for up to 1200 axle passes, equivalent to three one-hundred car trains [Eadie and Kalousek 2001].

1.5 Research Objectives

Little is known, however, as to the effectiveness of application of these spray nozzles. As in most spray coating applications, including this one, the primary objective is to achieve the best possible transfer efficiency (i.e. percentage of total liquid sprayed that

remains on the target surface) [Settles *et al.* 1998] while providing an adequately uniform deposition on the target surface, in this case, the surface of the rail. Thus, it is desirable to understand spray droplet behavior both before and after potential impact occurs on the TOR surface to optimize liquid-target placement. Any liquid not reaching the surface initially or not remaining on the rail surface after impact will contribute to environmentally undesirable and costly product wastage.

The main research objective of this project thus is to examine the interaction of a spray of a LFM with a rail surface, in the presence of a relative velocity, with the intent of optimizing spray deposition. Although the physics associated with field application (i.e. moving spray nozzle over stationary rail) are not able to be exactly replicated in the lab (see Chapter 3), an accurate indication of spray-rail interaction can be obtained using the experimental setup developed for this purpose. This includes a linear traverse, which propels a rail surface at high speed underneath a stationary mounted spray nozzle. High-speed photography is used to capture images of spray impaction behavior on the surface of the rail. In achieving the above objective, the author hopes that a more solid understanding of the physics behind spray coating applications can be obtained.

In addition, due to the lack of literature pertaining to non-Newtonian atomization, as well as inconsistent sprayer performance having been previously noted in the field due to the effect of cross winds and fouling, a concurrent project looking to characterize the behavior of sprayers of non-Newtonian liquids in a cross wind is also currently underway. In combining knowledge gained from both of these investigations, it is hoped that an optimal application method, with the highest transfer efficiency possible, can be achieved.

1.6 Summary

Railroads are the primary form of freight transportation in North America. Significant research has been conducted to improve the effectiveness and efficiency of railway transport. Friction reducing agents, such as grease-based lubricants, have been used in the past to reduce friction on the gauge face and the top of rail. However, these lubricants only lower the frictional levels and cannot control them at an intermediate level, which is desired at the top of rail surface. As a result, friction modifiers were developed which can, unlike lubricants, reduce, control, and maintain frictional levels at an optimum level. However, the effectiveness of the friction modifier is dependent on the application

method. One particular type of friction modifier is of a liquid nature and is typically applied to the top of rail using a spray nozzle located on locomotives or Hi-Rail trucks. The effectiveness of this form of application, in terms of spray deposition and transfer efficiency, is unknown. Thus, this has resulted in the present investigation, with the primary objective being to examine and improve this spray application process in an effort to obtain optimal transfer efficiency.

Chapter 2

Spray Impact on a Surface

This chapter will examine previous work pertaining to spray interactions with a surface. A brief introduction into atomization will be followed by a review of the existing research on spray impaction. This will lead into examinations of firstly Newtonian droplet impingement, followed by non-Newtonian droplet impingement. Further work will be reviewed pertaining to the effect of a moving surface on droplet impact behavior, with a summary ending the chapter highlighting the scope of the present work, as well as areas for future work.

2.1 Introduction

Atomization is defined as the disintegration of bulk liquid into small drops [Lefebvre 1989]. Liquid in the form of a jet or a sheet emerges from a spraying device, known as a nozzle or atomizer, and is disintegrated firstly into ligaments, and then into discrete droplets [Glass 1997], through the action of capillary forces. For the most common method of producing a spray, this disintegration occurs through the action of a relative velocity between the bulk liquid and a gaseous medium. This may occur by discharging a liquid with high kinetic energy into relatively slow-moving or stationary gaseous surroundings (i.e. pressure atomizer). In the case of a plain-jet airblast atomizer, an opposite approach is taken whereby a slow-moving central liquid stream is disintegrated by a high kinetic energy annular air jet [Lefebvre 1989]. In this case, aerodynamic forces greatly exceeding the magnitude of liquid surface tension forces (high aerodynamic Weber numbers) cause instabilities on the surface of the jet and thus, cause break-up. Other methods of producing sprays include the external addition of mechanical energy to the bulk liquid through vibration, rotation, or sound waves [Lefebvre 1989].

The science and knowledge behind atomization has grown substantially in the last decade. This is primarily due to advancements in technology, such as laser diagnostics, allowing for certain aspects of the spray to be analyzed which were previously not feasible, as well as a growing interest in potential spray applications. Sprays now play a very important role in many industrial processes including combustion in internal combustion and jet engines, spray drying and cooling, industrial washing, the delivery of agrochemicals, medicinal applications such as nebulizers, inkjet printing, and spray

coating applications such as fire suppression, paper processing, and spray painting [Lefebvre 1989].

The majority of the above applications involve the interaction of a spray with a surface. Being that sprays are comprised entirely of droplets, of varying size distribution, the impact of droplets on a surface, whether the surface is of solid or liquid form, is of fundamental interest as it is desirable to know whether impacting droplets stick to a surface or simply splash and/or rebound off. As a result, the majority of effort in the past has been put forth into understanding the physics behind droplet impact and only recently, with the onset of advanced technology, has the spray impaction process begun to be experimentally investigated.

2.2 Spray Interaction with a Surface

Spray impingement with a surface occurs in many industrial processes. This includes various types of internal combustion engines where the fuel, injected into the cylinder, can strike cylinder walls, combustion chamber walls, or the walls of the port or intake valve [Bai and Gosman 2002]. In these cases, fuel deposition on the wall can cause adverse effects by developing a liquid film on the wall, eventually leading to unburned hydrocarbon emissions. In this application, both primary splash and secondary atomization are encouraged to reduce the formation of this liquid film. In other cases, such as spray coating applications, a regular and homogeneous coating is desired, whereby splashing is directly avoided [Sivakumar and Tropea 2002, Roisman *et al.* 2002]. Thus, it is desirable to gain an understanding of the spray impact process for both design and modeling so the characteristics of spray impact can be determined [Ghielmetti 2001].

A spray interacting with a surface initially results in droplets impinging upon a dry, solid surface. However, almost instantaneously, the system transforms into one in which hundreds of droplets are impinging on a liquid film, deposited by prior impacting droplets [Vander Wal *et al.* 2006]. Upon impact on the liquid film, secondary atomization can occur, with secondary droplets being expelled in various directions away from the impaction point. Although the interaction of a spray, or individual droplets, with a liquid film is of fundamental importance in all spray-surface applications, including spray coating processes, it is not the focus of the present work and will not be considered

in this investigation. Therefore, only spray impaction on a dry, solid surface will be considered.

Experimental analysis of spray impingement is a relatively new and emerging field. This is due to the large difficulty in extracting detailed spray impingement data through experiment [Bai and Gosman 1995]. Only recently has the advent of advanced technology allowed experimental analysis of spray interaction with a surface to be performed. Many researchers have used phase-Doppler anemometry (PDA) [Bai *et al.* 2002, Panao and Moreira 2004, Mundo *et al.* 1997, 1998, Roisman and Tropea 2005] or laser-Doppler velocimetry (LDV) [Brunello *et al.* 1991] to characterize the incoming spray, as well as the impacting spray (i.e. secondary droplets). Even with the above experimental methods, a complete set of experimental spray impingement data has yet to be obtained.

Although high-speed photography has been used extensively to examine individual droplet impaction behavior, only a few studies have been conducted where high-speed photography is used to analyze spray impaction on a surface. As Dhiman and Chandra [2005] note, this is due to the small physical scale of the liquid features and high velocities at which they travel, making imaging for use of extracting quantifiable data, very difficult. Roisman and Tropea [2002, 2005] show images of spray impact taken with high-speed cameras yet they are used strictly for observing spray behavior. Sivakumar and Tropea [2002] however used two high-speed CCD cameras, along with the phase-Doppler technique to investigate the effect of interactions of impacting neighboring drops on an individual droplet impact outcome. Velocities and diameters were extracted using the images taken by the cameras and although a measure of uncertainty was associated with these measurements due to the resolution of the imaging system, the analysis still provided an accurate indication of near-wall droplet impaction details.

Numerical modeling, however, has been the primary means of investigating spray impaction on a surface to date. In most cases, these models are compared to and validated against experimental measurements taken using the above-mentioned techniques. All but a few of the current models treat the poly-disperse spray as a superposition of individual, non-interacting droplets [Sivakumar and Tropea 2002]. These include work by Naber and Reitz [1988], Bai and Gosman [1995], Stanton and Rutland [1996], and Mundo *et al.* [1998]. However, as shown by Tropea and Roisman [2000], these single droplet impaction models are inadequate due to unaccounted for

interactions between drops which arise during spray impact. These unaccounted for droplet interactions also cause single droplet impact models to be insufficient in predicting the amount of liquid deposited on the surface, as confirmed by experimental determination of the liquid deposited mass using PDA [Tropea and Roisman 2000, Weiss 2005]. To advance the area of spray impact modeling, Tropea and Roisman attempted to develop their own model, taking into account the interaction of neighboring droplets by introducing a statistical parameter to account for droplet interactions. Roisman *et al.* [2002] then went further and experimentally investigated the interaction of two droplets impinging on a surface, considered to be the first step in advancing single-droplet models to accurate poly-disperse models. Although very relevant to predicting spray impact outcome, spray impaction modeling is out of the scope of the present work and therefore, will not be investigated further.

2.3 Newtonian Droplet Impact

As mentioned above, the interaction of droplets with a dry, solid surface is of significance to many industrial processes. This has sparked substantial interest in this phenomenon and as a result, Newtonian droplet impact on a dry, solid surface is now a mature subject field, having been studied for over a century. Despite the significant effort however put into droplet impaction research on a dry, solid surface, this phenomenon is still not entirely understood [Yarin 2006].

Droplet impact behavior on a dry, solid surface is very complex and depends on many variables including impact velocity, impingement angle, droplet size, liquid properties such as viscosity, density, and surface tension, and surface properties including wettability and roughness [Yarin 2006]. It has been shown [Mundo *et al.* 1995, Yarin 2006] that the primary dimensionless groups governing Newtonian droplet impact are the Reynolds, Weber, and Ohnesorge numbers, defined respectively as:

$$\mathrm{Re} = \frac{\rho U d}{\mu},\ We = \frac{\rho U^2 d}{\sigma},\ \text{and}\ Oh = \frac{\mu}{(\rho\sigma d)^{1/2}} = \frac{We^{1/2}}{\mathrm{Re}},$$

where ρ, μ, and σ are the liquid density, viscosity, and surface tension, respectively, with d and U denoting the droplet diameter and impact velocity, respectively [Yarin 2006]. Additionally, sometimes a dimensionless surface roughness group is used, defined as $R_{ND} = R_a / d$ where R_a is the mean roughness height of the wall surface [Mundo *et al.*

1995]. Wettability, however, has yet to be accounted for in a non-dimensional representation [Sikalo *et al.* 2002].

In the past, it has been understood that three outcomes of post-impact droplet behavior are possible; bounce, splash, or spread [Rein 1993]. However, work by Rioboo *et al.* [2001] has expanded on this and has reclassified post-impact droplet behavior into six possible outcomes: deposition, prompt splash, corona splash, receding break-up, partial rebound, and complete rebound. These outcomes are shown below in Figure 2.1.

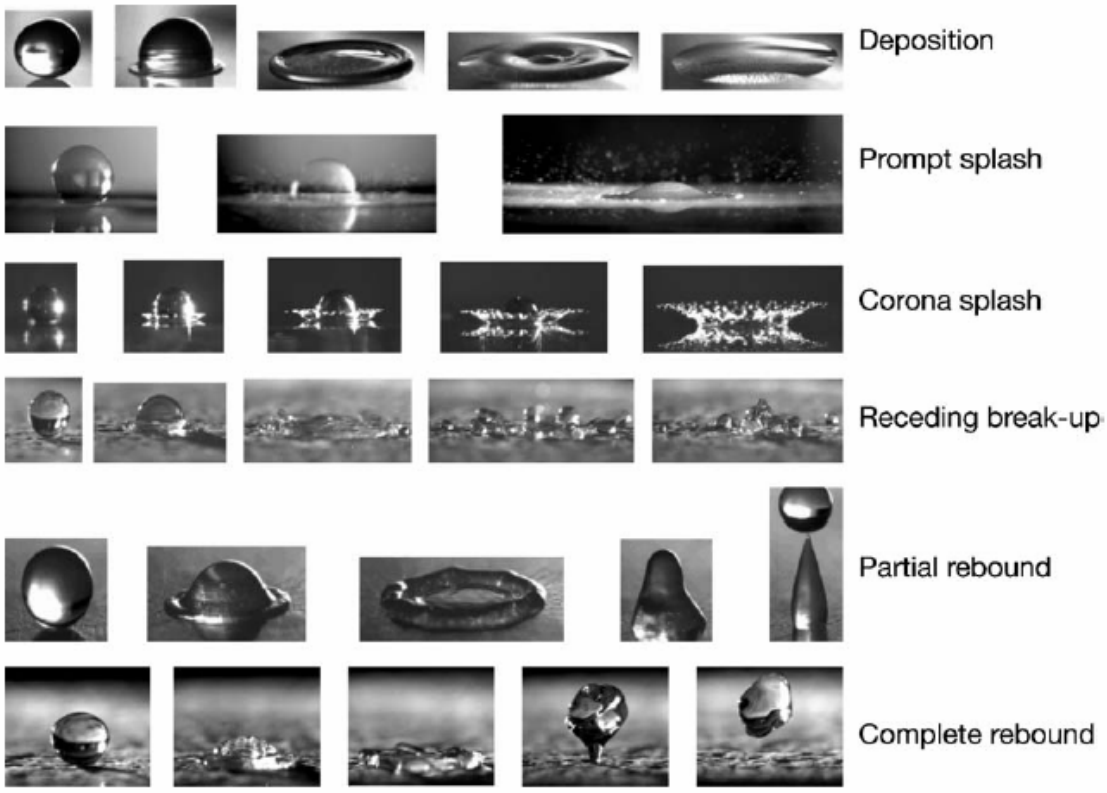

Figure 2.1: Six possible outcomes of droplet impact [Reproduced from Rioboo *et al.* 2001]

In order to promote maximum transfer efficiency, optimal droplet impact would involve deposition and adhesion of the liquid on the surface; both splash and rebound, regardless of type, can be detrimental to spray coverage.

The deposition process occurs in two stages; in the first, the kinematic stage, the radius of the drop expands at a rate independent of liquid and surface properties and is dependent solely on inertia. In the second stage, actual deposition, the impacting droplet spreads, relaxes, and then reaches an equilibrium state where it wets the surface. The drop remains attached to the surface the entire time with no breakup occurring [Rioboo *et*

al. 2001, 2002]. The kinematic stage, and partly the second stage, constitute an initial stage for the other outcomes [Yarin 2006]. A spread factor, $\xi = 2R_{max}/d$, where R_{max} is the maximum radius achieved during spreading and d is the non-deformed impacting droplet diameter, is often used to describe the maximum spread of a droplet when comparing to different drop impacts [Rioboo *et al.* 2002, Sikalo *et al.* 2002].

Receding breakup, although not to be considered further, is primarily a wettability phenomenon. This occurs if the dynamic contact angle reaches its limiting value of 0° during lamella retraction from its maximum diameter, thus leaving behind droplets on the surface [Rioboo *et al.* 2001].

Splash is defined as the formation of secondary droplets upon impact [Cossali *et al.* 1997]. The phenomenon of splash has been studied extensively; the physics involved and the mechanisms contributing to splash are well-known. Examples include, but are not limited to, work by Worthington [1876], Levin and Hobbs [1971], Stow and Hadfield [1981], Chandra *et al.* [1991], Mundo *et al.* [1995], Rioboo *et al.* [2001, 2002], and Sikalo *et al.* [2002, 2005b]. Increases in droplet inertia and surface roughness, amongst other variables, can lead to prompt splash, whereby droplets are formed at the contact line of the rapidly spreading lamella (the sheet of fluid that jets radially outwards underneath an impacting droplet) at the beginning of the spreading phase [Rioboo *et al.* 2001]. Furthermore, corona splash, first encountered by Levin and Hobbs [1971], promoted through a reduction in surface tension, can also occur. In this case, the liquid lamella detaches from the wall [Yarin 2006, Sikalo *et al.* 2002] and droplets are formed at the rim of a corona or crown.

A critical Weber number is often reported where splashing begins; however, the Weber number does not fully encompass all of the variables defining droplet splash, including other droplet properties and surface properties. This has led to widely differing critical Weber numbers having been reported in the literature [Rein 1993]. Range and Feuillebois [1998] however believe that their experimental data pertaining to splash can be described solely through use of a critical Weber number, stated as a function of surface roughness. This is of similar nature to work done by Stow and Hadfield [1981] who defined a splashing threshold on dry surfaces in terms of Reynolds and Weber numbers. Rewritten, Stow and Hadfield's splash threshold is of the form $WeOh^{-0.4} = K_L$ and is also a function of surface roughness [Cossali *et al.* 1997]. It was unclear however whether prompt or corona splash was referred to in their investigation

[Yarin 2006]. Bai and Gosman [1995] used experimental data taken by Stow and Hadfield [1981], combined with their own underlying assumptions, to derive a transition based on the critical Weber number for diesel spray impinging on a dry wall. This transition is given as $We_c = A \cdot La^{-0.18}$, where La is the Laplace number, defined as $La = \frac{\rho\sigma D}{\mu^2}$, and A is an experimentally determined constant based on surface roughness.

Mundo *et al.* [1995] used the parameter $K_L = Oh\,\mathrm{Re}^{1.25}$ to define the limit of deposition and corona splashing for both smooth and rough surfaces. The splashing threshold, K_L, found was 57.7, whereby any values of K_L above this value lead to splashing and any values below lead to complete deposition of the liquid. This correlation, when rearranged, is of the same form as that proposed by Stow and Hadfield, however slightly scaled (K_L = 6.58 x 10^2). This was confirmed after further inspection by Cossali *et al.* [1997] who showed that these two thresholds were consistent. As a result, Cossali *et al.* [1997] was able to establish his own correlation based on this data as $K_L = 649 + 3.76 / R_{ND}^{\ 0.63}$, where R_{ND} is the non-dimensional roughness, defined as the surface roughness normalized with droplet diameter. Finally, Yarin and Weiss [1995] were also able to experimentally determine a splash threshold of the same form as $WeOh^{-0.4}$, once again with a slightly scaled K_L value.

One author whose work contradicts this commonly determined splash threshold is that of Walzel [1980], who yielded a splash threshold of the form $Oh^{-0.7}We = 7.9x10^{10}$. This relation was shown to predict a critical We number that is one order of magnitude too large when compared to the data of Stow and Hadfield [1981]. It is suspected that reasons for this discrepancy may be due to surface roughness effects, as well as the relative size of the disk which was impinged upon [Cossali *et al.* 1997].

It is well known in the literature [Levin and Hobbs 1971, Stow and Hadfield 1981, Mundo *et al.* 1995, Cossali *et al.* 1997, Rioboo *et al.* 2001, 2002, Sikalo *et al.* 2002] that prompt splash is promoted with an increase in surface roughness (i.e. splashing threshold limit K_L is decreased as the non-dimensional roughness is increased). This is due to surface asperities causing instabilities on the lamella, thus leading to breakup. At small values of R_a, the splash threshold has a strong dependence on the surface roughness but as R_a gets large, this dependence becomes increasingly smaller [Parker 1970]. Corona splash, however, usually is seen on smooth surfaces. Mundo *et al.* [1995] showed that

when a droplet impinged on a very rough surface (with surface roughness height of the same order as droplet diameter), no corona was formed and instead, rigorous breakup into very small secondary droplets occurred. This is also noted by Lindgren and Denbratt [2000].

Rebound, on the other hand, results in a droplet, after impact, receding and either partially or fully leaving the surface which it impinged upon. Work done into the phenomenon of rebound includes, but once again not limited to, Pasandideh-Fard *et al.* [1996], Schiaffino and Sonin [1997], Kim and Chun [2001], Rioboo *et al.* [2001, 2002], Manzello and Yang [2004], Sikalo *et al.* [2002, 2005], and Lee and Kim [2004]. An understanding of the science behind rebound is yet to be complete [Kim and Chun 2001].

If significant kinetic energy exists at the end of the spreading stage and is still not dissipated during lamella receding, this may be enough to cause rebound to occur. If a partial rebound occurs, a liquid column is formed on the surface, which may produce one or more drops at its top due to the action of capillary forces. In complete rebound, the energy still existing in the receding stage may be enough to cause the droplet to leave the surface entirely [Yarin 2006]. Whether partial or full rebound occurs depends on the dynamic receding contact angle, where low values promote partial rebound and high values promote complete rebound. Liquid properties, such as surface tension and viscosity, as well as the difference between the maximum and final spread of the lamella, also have a significant role. Higher inertial impact (high We number) leads to larger maximum lamella spread [Rioboo *et al.* 2001, Sikalo *et al.* 2002], thus promoting rebound.

Direct empirical correlations put forth to describe the rebound threshold have not been described like they have for splashing. However, Schiaffino and Sonin [1997] were able to define a distinct Weber number range for liquid mercury droplets impinging on a glass surface, outlining the significance of the Weber number for droplet rebound. Kim and Chun [2001] confirmed this in their work. They found that recoil velocity is directly dependent on Ohnesorge and Weber numbers, with more dependence on the Ohnesorge number. They also concluded that a decrease in the Ohnesorge number or an increase in the Weber number leads to rapid recoil when impinging on a non-wettable surface. Sikalo *et al.* [2002] were also able to relate Weber number to rebound in realizing that a higher impact Weber number led to increased lamella spread and thus, increased the probability of rebound.

Sikalo *et al.* [2001] states that all not droplet impaction influencing parameters have been correctly stated in the past and thus, that droplet impaction thresholds cannot solely be quantified in terms of the Weber, Ohnesorge, and Reynolds numbers. Rein [1993] also notes that differences in impingement thresholds often lie in the fact that the exact conditions of the impact are often not well known. Simple things such as the contamination of a surface by foreign substances or surfactants may have a significant impact on drop impact outcome. More complex groupings, including the effects of surface roughness and wettability, as well as interdependency amongst the liquid and surface properties, must be considered, leaving this area open for future work [Sikalo *et al.* 2001]. Table 2.1 is a summary outlining the various parameters affecting droplet outcome where V_0 is the impact velocity, σ and μ are the liquid surface tension and viscosity, respectively, R_a and R_w are the roughness amplitude and roughness wavelength of the surface, respectively, and θ_{rec} is the dynamic receding contact angle.

Table 2.1: Summary of the effect of various parameters on the six possible droplet impact outcomes [Reproduced from Rioboo *et al.* 2001]

Increase of	Deposition	Prompt splash	Corona splash	Receding breakup	Partial rebound	Complete rebound
V_0	↓	↑	↑	↑	↑	
D	↓	↑				
σ		↓	↓	↑	↑	↑
μ	↑	↓	↓	↓		
R_a	↓	↑	↓			
R_w		↓				
θ_{rec}				↑	↑	↑

*Arrows indicate the sense of the respective parameter change to exceed the threshold for that outcome.

2.4 Non-Newtonian Effects

Many industrial coatings, including paints and agrochemicals, exhibit non-Newtonian rheological behavior owing to the presence of polymers and/or solid particles in their formulations. These non-Newtonian liquids exhibit both time and rate dependent shear viscosities, and can also possess Trouton ratios [ratio of extensional to shear viscosities] greater than the Newtonian value of 3 [Tirtaatmadja *et al.* 1993].

Work by Mansour and Chigier [1995] revealed that liquid viscoelasticity induced ligament stretching prior to the formation of discrete droplets. Ligament stretching

consequently led to an increase in droplet sizes when compared with the atomization of Newtonian liquids under the same atomization conditions [Li *et al.* 2005]. This result was confirmed by Mun [1999] in his work with agricultural sprayers, where he found that, as the molecular weight of the polymer additive rose, the resultant mean droplet size increased while the percentage of small droplets formed decreased.

As a result of the wide-spread use of non-Newtonian solutions in numerous industrial applications, researchers in the last decade have shifted their focus slightly to begin examining non-Newtonian droplet impaction. In comparison to Newtonian droplet impaction however, this topic is a relatively new and emerging field.

Preliminary work has shown that droplet deposition can be controlled by introducing polymers and other non-Newtonian agents to otherwise Newtonian solutions with aims of suppressing splash and rebound, a phenomenon greatly desired in coating applications [Yarin 2006]. Cooper-White *et al.* [2002] notes that both splash and rebound for Newtonian droplets can be retarded by increasing the liquid shear viscosity. Actually, as noted by Rioboo *et al.* [2001], increasing the shear viscosity decreases the probability of all droplet break-up mechanisms. However, in doing this, a significant increase in the energy required to atomize is introduced; thus making use of non-Newtonian agents to control droplet deposition looks far more favorable.

Bergeron *et al.* [2000] discovered that with the addition of polymer additives, such as polyethyleneoxide (PEO), droplet recoil from smooth non-wetting surfaces was suppressed. Bergeron attributed the suppression of rebound to the high extensional viscosity inherent in high-molecular weight polymeric solutions. Crooks and Boger [2000] went further and discovered that the splash threshold, the transition where spreading to splashing takes place, on hydrophilic surfaces was significantly higher for elastic droplets than inelastic (Newtonian) droplets. They found that the splash threshold for Newtonian solutions $K_L = WeOh^{-0.4}$ does not apply to elastic non-Newtonian solutions, thus highlighting that the surface roughness, and the Ohnesorge and Weber numbers, are not sufficient to describe the splashing threshold of elastic solutions. Crooks and Boger [2000] were then able to establish a vertical shift factor, based on data for a Newtonian liquid, which allowed them to predict the splash threshold for elastic liquids. Furthermore, they were able to show that the splash threshold increased with increasing molecular weight of the polymer. In another study by Crooks *et al.* [2001], the droplet recoil height and velocity were related to the apparent Trouton ratio for a set

of elastic test liquids. They found that with an increase in molecular weight of the polymer additive, a significant reduction in the recoil velocity and maximum recoil height was observed, supporting the previously mentioned findings of Bergeron *et al.*

Rafai and Bonn [2005] further investigated the effects of non-Newtonian rheology on droplet impaction behavior by employing shear-thinning and elastic test liquids. They found that both these non-Newtonian characteristics led to a reduction in the rate of spreading, which is in agreement with the findings from Bergeron *et al.* and Crooks *et al.*

Finally, work by Rozhkov *et al.* [2003] revealed that the addition of high-molecular polymer additives did not have an effect on the droplet recoil velocity and that the spreading lamella retracted in the same manner as that of a Newtonian water droplet. This is in disagreement with the results obtained by Bergeron *et al.* and Crooks *et al.* The discrepancy is believed to be due to the influence of the substrate on which the droplets impacted. Rozhkov *et al.* removed the influence of the substrate by employing a small target [of diameter similar to the impacting droplet]; the authors formerly mentioned used a hydrophobic plate, much larger than the diameter of the impacting droplet. Thus, Rozhkov *et al.'s* findings suggested that polymeric additives do not have a direct effect on the elongational deformations of a droplet, but instead directly affect the interaction of the lamella during the recoil stage.

As noted by Li *et al.* [2005], atomization of elastic liquids can lead to the formation of large-scale ligaments. In his examination of the air-blast atomization of three model elastic test liquids of varying PEO concentrations and molecular weights, Li *et al.* [2005] found that filamentary breakup structures were produced, with their scales increasing with elasticity. It was believed that the elasticity exhibited by these polymeric solutions was the cause for the formation of ligaments. The author however is currently unaware of existing literature pertaining to ligament impaction.

2.5 Droplet Impaction on a Moving Surface

As mentioned above, a stationary mounted spray nozzle will apply the LFM to a moving surface. The moving surface will be provided through means of a linear traverse, further described in Chapter 3. The moving surface is desired for three reasons: 1) to replicate the spray coating process of a LFM onto the surface of the rail in the presence of a relative velocity, 2) to visualize spray impaction on a dry solid surface without build-

up of previously deposited liquid, and 3) to examine the effect, if any, of surface speed on droplet impact and deposition.

When droplets impinge normally upon a moving surface as opposed to a stationary surface, splashing may be enhanced. This is due to a sudden tangential force that the droplet experiences upon impact, causing a destabilizing effect on the droplet [Rein 1993]. This is also experienced when a droplet impinges obliquely on a surface. Furthermore, upon entering the boundary layer at the wall, additional deforming forces are introduced to the droplet [Rein 1993] which could decelerate and deform the drop slightly before impact. This was shown by Yao and Cai [1988] whose experimental setup involved droplets impinging normally onto a moving disk. They noticed that as the rotating speed was increased, a substantial reduction in the critical Weber number for splashing occurred.

Additionally, Parker [1970] noted that in his work with droplets impinging on a spinning disk, the presence of a boundary layer caused a proportion of the mass of the impacting droplet to lift-off from the surface. This was due to the air layer penetrating underneath the impacting droplet. This was also found by Povarov *et al.* [1976a,b] who observed that surface speed indeed has a definitive effect on droplet impact outcome. Povarov observed three cases of boundary layer interaction with an impinging droplet to be spreading, partial reflection, and total reflection, with spreading occurring for laminar boundary layers (lower surface speed) and eventually leading to total reflection for turbulent boundary layers (high surface speed). It is unknown at this time as to what effect the moving surface provided through use of the linear traverse will have on the spray impaction behavior in the present investigation.

2.6 Summary

Experimental investigations of spray impingement have previously been rather limited primarily due to the small physical scale of the liquid features and high velocities at which the droplets travel, making visualization very difficult. Only with the recent onset of advanced technology has a detailed examination of sprays become more attainable. Spray impingement modeling is more abundant; however to accurately model the spray impingement process, a detailed understanding of droplet impact dynamics is needed for both Newtonian and non-Newtonian liquids. Significant literature exists in the area of Newtonian droplet impact, however is still lacking for non-Newtonian droplet

impact. Finally, a moving surface will be used in the present investigation and it is expected that boundary layer effects will play a role in analyzing droplet impaction. A detailed understanding of the spray impingement process is crucial in optimizing many spray coating applications, particularly in the present industrial case.

This thesis will experimentally investigate the interaction of a spray with a moving surface using high-speed photography. As a result of the industrial collaboration behind this project, KELTRACK LFM will be the primary fluid of choice for spray testing. Various other model rheological test liquids will be investigated; firstly, Newtonian fluids of varying shear viscosity will be tested to isolate the effect of shear viscosity in order to validate the work done in this project to the work of previous authors, and secondly, liquids of varying non-Newtonian rheological behavior, including elastic and shear thinning, will be used to isolate the effect of non-Newtonian properties on spray impingement and deposition, as well as to examine the impaction of ligaments. The author hopes that this work will assist in optimizing the industrial spray coating process described above, as well as further advance the knowledge in the area of spray coating, particularly relating to improving transfer efficiency and isolating the effect of various non-Newtonian properties.

It would be of significant interest to Kelsan to obtain knowledge of the effects of additional various properties on the droplet impact dynamics of KELTRACK. Although not in the scope of this project, this would include the examination of surface temperature, spray impingement angle, surface roughness, and rail surface speed. This thus leaves the door open for future work.

Chapter 3

Experimental Setup and Methodology

This chapter describes the experimental test rig and setup used in the present investigation. The linear traverse, used primarily as a means to provide a moving surface, will first be addressed. The design and application of the moving surface, hereinafter denoted as the projectile surface, will then be discussed. An overview of the experimental spray setup will be given, including nozzle specifics. The nine experimental test liquids used in the present investigation will be introduced, with their rheological properties given. Finally, a detailed description of the imaging setup used, specifically the high-speed camera, will be put forth.

3.1 Linear Traverse

A linear traverse was designed and built specifically for providing a moving surface onto which a spray can impinge. As mentioned in Chapter 1, in field applications, the LFM is applied to the surface of the rail through nozzles mounted underneath locomotives or Hi-Rail trucks. In these applications, the moving nozzle applies the LFM onto a stationary rail. There is no presence of a boundary layer on the surface of the rail however there are the presence of external aerodynamic effects including turbulence, large-scale vortices, and crosswinds, initiated by the passing-by of the locomotive. These effects would be very difficult, if not impossible, to replicate in the lab and are therefore neglected in the current investigation. Li [2006] however has attempted to examine these external aerodynamic effects by examining the effect of a spray in a cross-flow.

In any case, the linear traverse set-up, whereby a stationary nozzle applies the LFM to a moving rail is a very good approximation to field application and is the best that can be done given existing resources. It would be expected that if it was attempted to accelerate the nozzle up to high velocities in the lab environment, unsteady fluctuations in both liquid and air flow rates would occur, thus introducing a large element of uncertainty in the spray behavior. However, on the other hand, accelerating the rail to high velocities leads to the formation of a boundary layer on the surface of the rail, which in turn may affect droplet trajectories. This will be taken into consideration when examining droplet impingement.

A number of design options were initially considered for the linear traverse however will not be discussed further here; a brief description of these additional options can be found in sections A.1 and A.2 in Appendix A. A pneumatic energy storage system however eventually presented itself to be the most desirable design and was thus pursued.

With the pneumatic energy storage design in mind, a thermodynamic model [Mish and Hubbard 2001] was firstly developed in MATLAB™, using thermodynamic relations and Newton's second law to estimate traverse performance based on design selection criteria (i.e. air tank volume, barrel length, etc.). Further detail pertaining to this model, as well as estimated traverse performance curves, are given in section A.3. Using this model as a tool for component selection, components were purchased from local manufacturers and the linear traverse, essentially a large air cannon, was constructed. The linear traverse setup works as follows: pressurized air in a tank is rapidly released into a long, narrow barrel wherein a projectile surface (wooden carrier base with the desired impaction surface mounted on top) resides such that it expels out at a velocity dependent on the initial air pressure set in the tank. After exiting the barrel, the projectile surface travels beneath the atomizer and the resultant spray before striking an energy dissipation device and coming safely to a stop. The linear traverse can propel our 2.5 kg projectile up to speeds of 30 m/s using an air pressure of 7.2 bar (90 psig). Figure 3.1 depicts the linear traverse consisting of a 30 gallon air tank connected to a central air compressor (not shown) capable of delivering a maximum of 7.9 bar (100psig), a solenoid actuated poppet valve connected to the tank by means of a 1.5" NPT rubber hose, a 3 meter long 10 cm x 15 cm x 0.6 cm section of rectangular steel tubing, with the last meter of the tube being cut in half crosswise, and the energy dissipation device. A number of strategically positioned sandbags, wrapped in Kevlar®, were used to dissipate the kinetic energy of the moving projectile. A detailed set of procedures for operating the linear traverse are given in Appendix B.

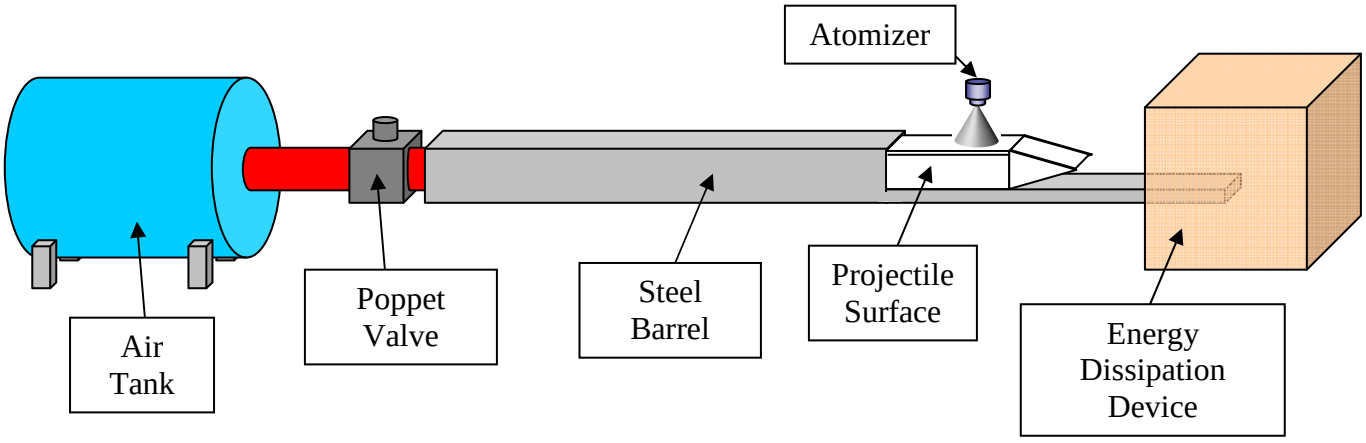

Figure 3.1: Linear traverse schematic

Finally, upon completion of the linear traverse, it was noticed that the expansion of the air in the tube, particularly upon exit out the tube, caused a relatively loud burst of noise to occur. This, of course, raised concerns that this excessive noise may be harmful to the occupants of Lab 308 in the PPC. In order to ensure compliance with the Worker's Compensation Board of British Columbia, sound pressure level testing was carried out. Upon completion of the analysis, a sound proofing enclosure was constructed around the air tank and all patrons of the lab near the vicinity of the traverse while in operation were required to wear ear protection. A complete description of the sound pressure level analysis can be found in section A.4.

3.2 Projectile Surface

A 13mm thick mirror-polished, work-hardened steel surface, formerly the top layer of a 136# designation rail, was secured to a wooden base. This wooden base acted as a light-weight carrier for the impaction surface and approximated the side faces of a typical rail section to ensure that the aerodynamics of the spray around the rail were emulated correctly. The dimensions of the wooden base were chosen to match closely to that of the steel barrel internals to minimize air leakage. The leading 25 cm of the wooden carrier was shaped into an aerodynamic nose to reduce the onset of boundary layer separation, as well as to minimize aerodynamic drag. The projectile surface is shown in Figure 3.2.

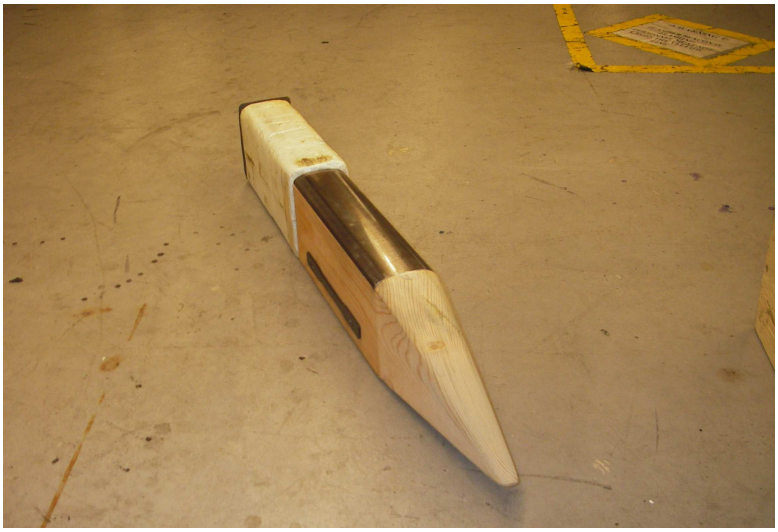

Figure 3.2: Projectile surface with tail plug

Finally, a projectile tail plug was constructed to push the aforementioned projectile surface down the barrel. The purpose of the tail plug was to provide a tight seal around the inside of the barrel, thereby further keeping air leakage to a minimum. The tail plug also ensured that the projectile surface had opportunity to travel beneath and beyond the spray before the rapidly expanding air from inside the barrel was allowed to exit and disrupt the trajectories of airborne droplets. The tail plug was constructed from polystyrene foam, with dimensions closely matching that of the barrel internals. Mounted at its trailing end was a 10cm x 15cm piece of gasket material that acted like a "wiper" surface, further minimizing the potential for air leakage.

3.3 Spray Setup

The nozzle used for all spray tests was an external-mix, plain-jet co-axial air-blast atomizer, shown in Figure 3.3, which had a liquid orifice inner diameter of 1.47 mm and an annular air orifice gap of 0.69 mm. The atomizer was mounted on a swivel mechanism, which allowed for varying spray impingement angles. The distance between the atomizer and the top of the projectile surface was approximately 67mm. The liquid was delivered to the nozzle by a gear pump and a common liquid flow-rate of 60ml/min was used for all spray tests, measured using a stopwatch and a graduated cylinder. Before the liquid exited from the nozzle, it passed through a small rubber nipple known as a duckbill, designed to prevent liquid leakage when the pumps were turned off. The atomizing air pressure was monitored using a dial gauge and was set at 1.4 bar gauge

pressure (20psig). All spray tests were conducted at an ambient temperature of 25ºC and atmospheric pressure.

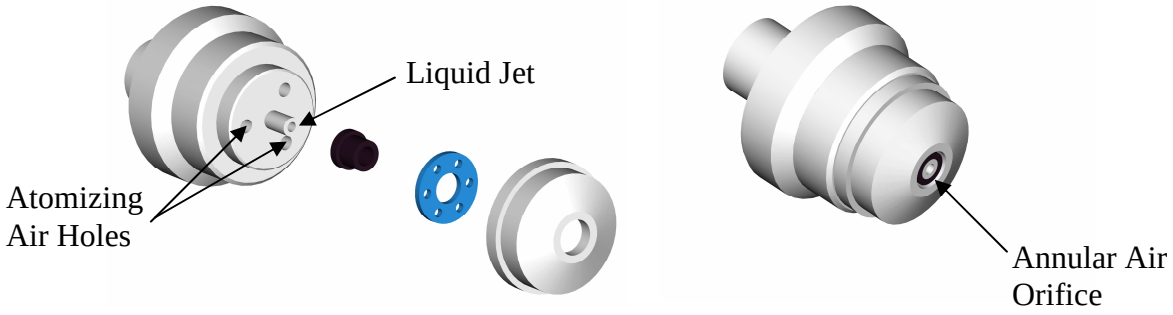

Figure 3.3: Plain-jet co-axial air-blast atomizer (w/o regular duckbill)

3.4 Test Liquids

The industrial water-based LFM, known as KELTRACK HIRAIL, was the fundamental test liquid used in this investigation. Using a HAAKE HS1 viscometer, Li [2005] measured KELTRACK's shear viscosity, up to a shear rate of 32000 s^{-1}, and observed strong shear-thinning behavior, with the absence of a limiting shear viscosity at high shear rates. KELTRACK's behavior can be conformed to the power-law model ($\mu = k\dot{\gamma}^{n-1}$), where *k* and *n* are the consistency and power-law indices, respectively. Li determined these indices to be 3610.9 mPa.s^n and 0.5214, respectively. This behavior can be seen in KELTRACK's shear curve at 25°C, shown in Figure 3.4 below.

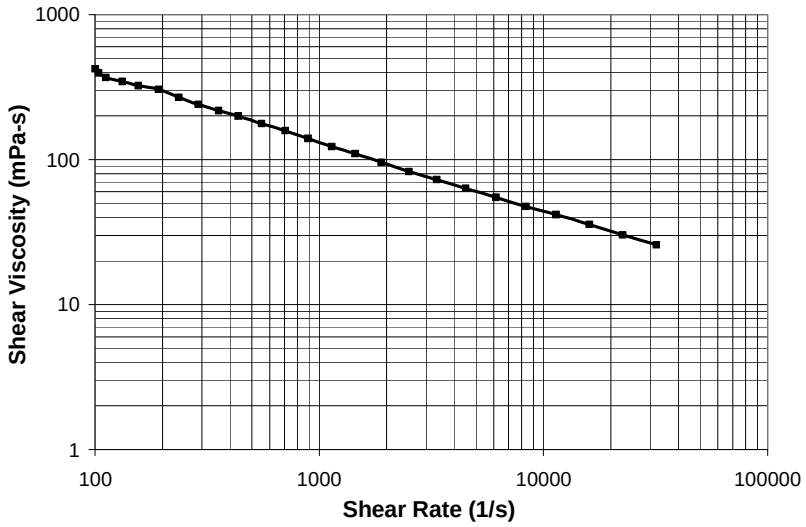

Figure 3.4: KELTRACK® shear viscosity [Li *et al.* 2005]

Li also measured the density of KELTRACK HIRAIL and found it to be similar to that of water at 25°C.

Finally, KELTRACK HIRAIL is believed to be elastic owing to its similarities in breakup upon atomization, particularly in the presence of ligaments and filamentary structures, to elastic test liquids, as shown by Li [2005].

As a means of investigating the rheological properties behind KELTRACK's spray impaction behavior, additional test liquids with defined rheological properties were formulated in order to compare their spray impaction behavior to that of KELTRACK. In total, three elastic, three inelastic, and two shear-thinning test liquids were formulated and tested alongside KELTRACK. These additional test liquids used, with exception to the shear-thinning liquids, were the same as the ones used by Li in his investigation, allowing for a detailed set of experimental test data, when combined with Li's work, both immediately upon breakup and upon surface impaction.

Firstly, as a measure of isolating liquid elasticity, constant low-viscosity Boger fluids [Boger 1977, Crooks *et al.* 2000] were developed. Three varying molecular weights (M_v), 100K, 300K, and 1000K g/mol, of polyethylene oxide (PEO), purchased from Sigma-Aldrich, were dissolved in a solution of glycerin and distilled water. As noted by Mun *et al.* [1999], PEO is a flexible, water soluble, and non-surface active polymer, making it desirable for this application. The relative concentrations of glycerin and water to maintain approximately similar shear viscosities of 5 mPa·s were of those suggested by Mun *et al.* [1999]. Mun [1996] also showed that the elasticity of these liquids was directly dependent on PEO molecular weight, with elasticity increasing with molecular weight.

Secondly, as a measure of isolating shear viscosity, two inelastic test liquids were formulated, consisting of a 50 weight % and an 80 weight % glycerin-water solution, in addition to pure distilled water. Shear viscosities of the solutions were directly dependent on the relative glycerin concentration. All elastic and inelastic glycerin solutions were constructed with USP Grade 99.5% glycerin. Table 3.1 summarizes the compositions of both the elastic and inelastic test liquids.

Table 3.1: Compositions of test liquids at 25°C [Li *et al.* 2005]

PEO M_v [g/mol]	PEO wt.%	Glycerin wt.%	Water wt.%	μ_s [mPa·s]	σ [mN/m]	ρ_l [g/cm^3]
-	0	0	100	0.9	69.2	1
-	0	50	50	5.1	66.6	1.13
-	0	80	20	46.7	65.2	1.21
100000 (100K)	0.6	32.4	67	4.8	60.4	1.08
300000 (300K)	0.05	44.35	55.6	5.1	59.7	1.11
1000000 (1000K)	0.075	38.0	61.925	4.9	57.3	1.10

The majority of shear viscosities, surface tensions, and densities of both the elastic and inelastic solutions shown above in Table 3.1 were measured by Li [2006]. Li used a HAAKE VT550 viscometer with a MV-1 concentric-cylinder sensor to measure the shear viscosities of both the elastic and inelastic test liquids at a temperature of 25°C. Shear rates in the range of 100 to 1000 s^{-1} were used for both the elastic and inelastic test liquids and the viscosities were found to remain relatively constant. Similarly, Li [2006] used a Du Noűy ring apparatus to measure the equilibrium surface tensions of these additional test liquids, which were found to vary from 57.3 to 60.4 mN/m and 65.2 to 69.2 mN/m for the elastic and inelastic liquids, respectively. Errors associated with the above measurements can be found in section 4.8.

Finally, as a means of examining shear-thinning behavior on droplet impaction, both a 0.067 wt.% Carbopol® 940 solution and a 0.3 wt.% xanthan gum solution were prepared. The Carbopol® 940 and xanthan gum were purchased from Noveon and R.T. Vanderbilt Company Inc., respectively. Carbopol® polymers are cross-linked polyacrylic acid polymers which swell in water when exposed to a pH environment above 4-6 [de Vicente *et al.* 2006]. They are widely used as thickening agents in cosmetic products. Xanthan gum, on the other hand, is a rod-like polysaccharide of high molecular weight and is also used as a thickening agent, including in many foods [de Vicente *et al.* 2006]. Both Carbopol® and xanthan solutions were prepared by slowly dissolving the appropriate amount of polymer (and sugar, in the case of xanthan) into an agitated container of distilled water, being sure the polymer was added gradually to avoid polymer clumping. In addition to the 0.3 wt.% xanthan gum powder, 33 wt.% sucrose (Rogers white sugar) was added to the polymer solution, leaving 66.7 wt.% of water.

Furthermore, in regards to the Carbopol® solution, once the Carbopol®-water solution had been left for 24 hours, sodium hydroxide was added to the agitated bath until the pH was approximately 7. This neutralized the solution and activated the polymer, an essential step in obtaining shear-thinning behavior [de Vicente *et al.* 2006].

Shear viscosity measurements were taken of both liquids using a Bohlin C-VOR rheometer, with a concentric vane and cup geometry, at a temperature of approximately 20°C. Figure 3.5 displays the shear curve for Carbopol®.

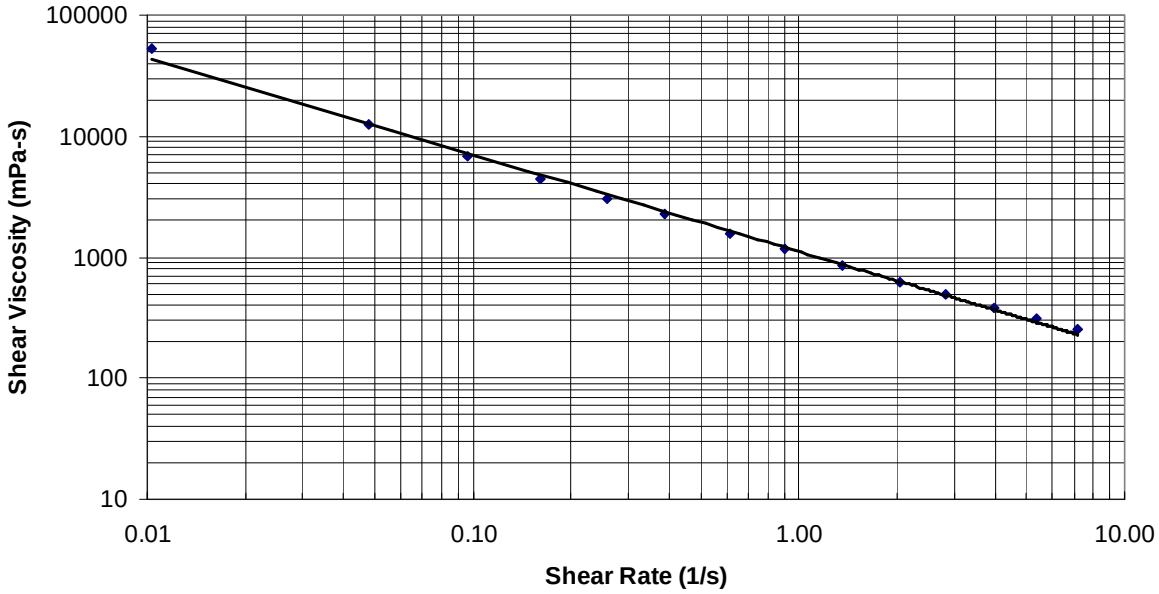

Figure 3.5: Carbopol® shear viscosity (baseline)

Carbopol® exhibits viscoplastic behavior, in that it behaves like a solid below a certain yield stress value and then flows like a liquid once this stress has been overcome [Noveon, Inc.]. It can be seen from Figure 3.5 that once the yield stress has been overcome, Carbopol® exhibits power-law behavior. Carbopol's behavior can thus be described by the Herschel-Bulkley model, given as:

$$\tau = \tau_o + k\dot{\gamma}^n \qquad (3.1).$$

The apparent yield stress for this particular batch of Carbopol® was determined to be approximately 0.55 Pa, determined by examining the viscosity-shear stress relationship.

Similarly, Figure 3.6 displays the shear curve for xanthan gum.

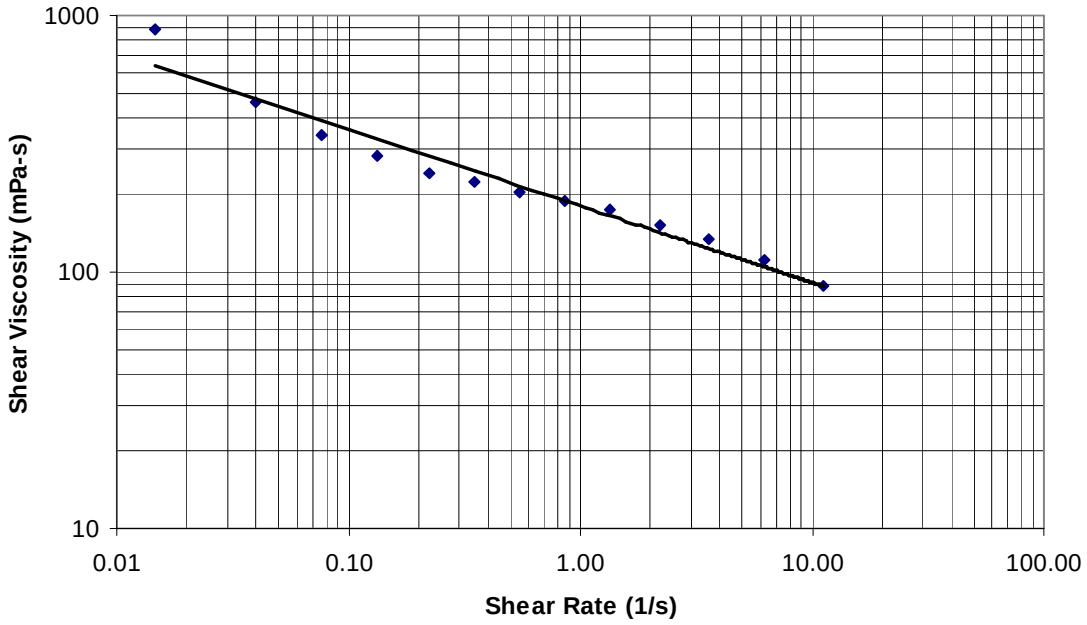

Figure 3.6: Xanthan gum shear viscosity

Similar to Carbopol® and KELTRACK, xanthan gum also exhibits power-law shear-thinning behavior; it does not however exhibit viscoplastic behavior. Power-law and consistency indices are given for both Carbopol® and xanthan gum in Table 3.2.

Surface tensions of the shear-thinning test liquids were also measured and found to be 61.7 and 62.5 mN/m for the Carbopol® and xanthan gum solutions, respectively. The surface tension of KELTRACK, also measured by Li, was found to be 39.7 mN/m, significantly lower than all of the above values.

Table 3.2 summarizes the consistency and power-law indices, surface tension, and density values of KELTRACK and the two shear-thinning liquids.

Table 3.2: Shear-thinning liquid properties

	Consistency k [mPa-s^n]	Power-Law Index n	σ [mN/m]	ρ_l [g/cm^3]
KELTRACK	3610.9	0.5214	39.7	1.09
Carbopol®	1113.1	0.198	61.7	1.00
Xanthan Gum	180.63	0.702	62.5	1.09

To aid visualization of the finely atomized liquid features, red food dye was added to both the elastic and inelastic test liquids. Measurements of the shear viscosities of the test

liquids before and after addition of the food dye showed very little, if no effect, of the food dye, thus justifying the use of this coloring agent to ensure sufficient liquid contrast while imaging. For the same purpose, ink was used to dye the xanthan gum solution; any effect of the ink on the xanthan gum polymer structure was deemed negligible due to such a minute concentration (≈ 0.25%). This ink was also used to dye the Carbopol® solution. Upon further testing, however, it was realized that the addition of the ink had an effect on the polymer structure in that it lowered the yield stress up to as much as an order of magnitude in some cases. This is believed to be due to the acidic nature of the ink. Once this was realized, all further testing with Carbopol® was done using phenol red, a liquid pH indicator with a pH ranging from 6.8 – 8.0. The addition of phenol red to the Carbopol® solution was shown to have negligible effect on the Carbopol® shear curve and yield stress.

The justification of using food dye and phenol red to color the transparent liquids to increase imaging contrast is given in Appendix C.

3.5 Imaging Setup

Vision Research's Phantom v7.1 and v9.0 high-speed cine cameras were employed to visualize spray impaction on the projectile surface. These cameras use a SR-CMOS (self-resetting complementary metal oxide semi-conductor) sensor to allow image capture at extremely high frame rates without significantly compromising resolution. A high-intensity continuous light source, the PALLITE® VIII, was used to illuminate the surface.

The camera was positioned in two orientations. In the first one, the camera was oriented downwards at an angle of 6.5 degrees from the horizontal to better view impaction events, and was located approximately 14.2 mm to the right of the spray. By placing the camera in this position, near the periphery of the spray, the droplet number density was considerably lower than at the spray centerline, which allowed for better visualization and identification of individual droplets and their impactions (i.e. what exactly they impinged on: previously deposited liquid or dry surface). Also, by placing the camera to the right of the spray and viewing the projectile surface before it had gone through the entire spray, a far greater number of droplet impacts on a dry surface were observed than if the camera had been placed on the left. The optical setup was based on the typical backlit technique. Figure 3.7 below shows the horizontal camera setup in relation to the projectile surface and the nozzle.

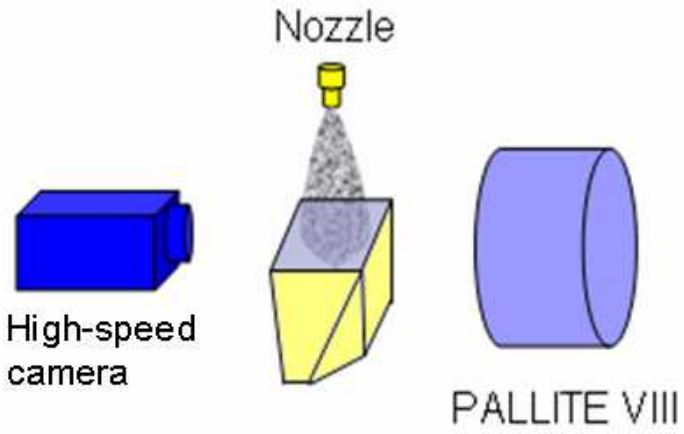

Figure 3.7: Horizontal imaging setup

A preliminary set of experimental tests in the horizontal orientation were performed with the Phantom v7.1 and the Nikon AF Micro-Nikkor 60mm f/2.8D lens. A resolution of 256 x 256 pixels, a frame rate of 26,900 pictures per second, an f# of 5.6, and an exposure time of 1 microsecond were standard. The depth of field (DOF) was approximately 3mm and all videos had a field of view (FOV) of approximately 9mm x 9mm, equating to a pixel resolution of 35µm.

After performing preliminary data analysis on this first set of videos however, it was realized that a higher pixel resolution was needed to minimize the error in determining droplet diameter. Therefore, a second set of tests were performed with the goal of improving pixel resolution (i.e. decreasing the FOV while keeping camera resolution the same). Originally, a Navitar 12x zoom lens was first tried and although it was able to provide a more than sufficient pixel resolution, it was found to allow sufficiently less light to the sensor due to a smaller aperture and therefore, significantly compromised the quality of the videos. At the same time though, it was realized that there was a limit on the minuteness of the field of view; although microphotographs of droplet impaction were desired to accurately discern post impact behavior (very small FOV), information regarding droplet velocities were also needed, making it necessary to be able to track droplets for multiple frames hence requiring a larger FOV.

For this second set of tests however, the Phantom v9.0 was employed due to the unavailability of the Phantom v7.1 at the time of testing. Due to the v9.0's slightly different camera capabilities, a resolution of 288 x 256 pixels, a frame rate of 15,625 pictures per second, an f# = 5.6, and an exposure time of 2 microseconds was considered

optimal for all tests. In assuming a droplet velocity of 30 m/s (near the top-end of the velocity spectrum) and given the above frame rate, a droplet would travel approximately 1.9 mm between frames. Based on this, a FOV of approximately 4.1 x 3.9 mm was deemed a desirable compromise. Thus, the original decision of the Nikon AF Micro-Nikkor 60mm f/2.8D being the lens of choice was renewed as this lens allowed for a minimum FOV of approximately 3mm, considered to be more than sufficient for our purposes, while still providing sufficient light. This new imaging setup allowed for a pixel resolution of 15µm, a significant improvement over the previous pixel resolution. The depth of field measurement stayed the same at approximately 3mm.

In the second orientation, the camera was positioned so as to view the spray impaction on the surface of the rail from an overhead angle. The camera was placed directly above the traverse barrel at an angle of 52° from the horizontal, with the camera being focused on the surface of the rail, as shown in Figure 3.8. In this case though, the backlit imaging technique no longer applied and so light from the PALLITE® was reflected off of the rail surface. A resolution of 288 x 256 pixels, a frame rate of 15,625 pictures per second, an f# = 5.6, and an exposure time of 2 microseconds was also used for these tests. A FOV of approximately 57 x 51mm was standard for all overhead tests, set to encompass the entire width of the rail in the viewing window.

In both orientations, the camera was triggered electronically by a photodiode assembly.

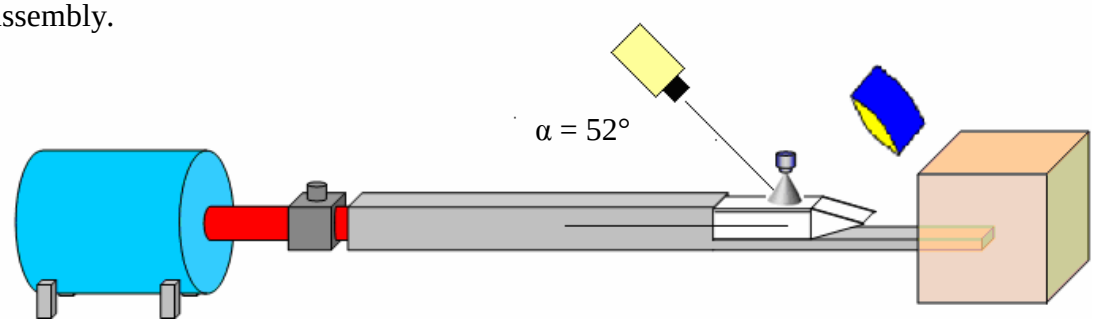

Figure 3.8: Overhead imaging setup

3.6 Summary

A novel linear traverse, essentially a large air cannon, has been designed for use in spray impaction studies of which its sole purpose is to provide a moving surface on which spray impingement can be examined. The linear traverse is designed to approximately replicate field application of LFM although there are still definitive differences existing between field and lab application which cannot be replicated. A

projectile surface, consisting of a mirror-polished 30cm section of work-hardened steel mounted on a wooden carrier with an aerodynamic nose, is expelled out the end of the linear traverse barrel. It is then impinged upon by a spray generated by an external mix co-axial air-blast atomizer located approximately 67mm above the projectile surface. A total of nine test liquids, including KELTRACK LFM, were sprayed in the investigation, with the purpose of isolating and examining the effect of shear viscosity, elasticity, and shear thinning behavior on droplet impact dynamics. The spray impingement phenomenon is examined from both horizontal and overhead views using high-speed photography. Finally, the projectile surface enters the energy dissipation device, where it impacts a number of strategically placed sandbags and is brought to a stop.

Chapter 4

Experimental Results and Discussion

This chapter outlines and discusses the key findings of this experimental investigation. Firstly, spray impact analysis of the nine test liquids will be put forth, whereby impacting Weber, Reynolds, and Ohnesorge numbers will be stated for a given sample distribution. These numbers will then be used to calculate and compare to a critical splash-deposition limit for Newtonian liquids, previously developed in literature. Secondly, a discussion will ensue pertaining to the impingement of elastic liquids, particularly in regards to ligaments and filamentary structures, which are developed as a consequence of a liquid's viscoelastic properties. Thirdly, additional means for the improvement of transfer efficiency will be addressed, including discussions of overspray and droplet entrainment. Fourthly, an analysis of the spray deposition on the surface of the rail using spray labels will be given and discussed, with the goal of highlighting possible deposition asymmetries. Fifthly, a discussion of the effects associated with increased surface speed will be mentioned, pertaining solely to the effect of the boundary layer on the surface of the rail. Sixthly, a brief mention will be given regarding noticeable spray pulsations that were observed in the videos under examination. Next, the effect of orienting the spray nozzle at angles of 45° both away and against the incoming rail to both decrease and increase the effective relative velocity between the droplets and the surface, will be mentioned. Finally, uncertainty analysis for the droplet impaction results will be outlined in section 4.8.

4.1 Spray Impact Analysis

4.1.1 Impinging Droplet Parameters

The objective of this analysis was to examine the effects of specifically isolated rheological properties on droplet impact and then compare these effects to the spray impaction behavior of KELTRACK. This would provide insight as to whether or not KELTRACK's current rheological formulation is effective in ensuring optimal transfer efficiency.

Horizontally imaged high-speed cine videos were taken of the spray impaction process for all nine rheological test liquids at a projectile surface speed of approximately 10m/s (± 1m/s). Individual droplets were tracked and observed, both before and after impact on the surface of the rail, as shown in Figure 4.1. Approximately 40 droplets, on

either end of the size spectrum, were chosen for analysis. Only droplets considered in focus (i.e. in the depth of field) were used in droplet examination so as to minimize error in droplet sizing. Keep in mind that the goal in analyzing these videos was not to perform droplet sizing or droplet velocity analysis, but instead to use droplet size and velocity info to make observations and conclusions regarding the impaction behavior of these droplets (furthermore, droplets would be selected from near the spray centerline as opposed to the right of the spray if a droplet size and velocity distribution was sought after). Measurements of droplet diameter, impact velocity, and impact angle were taken (the details behind how these measurements are taken are discussed in Appendix D) and using this information, impacting Weber number, Reynolds number, and Ohnesorge numbers, were determined.

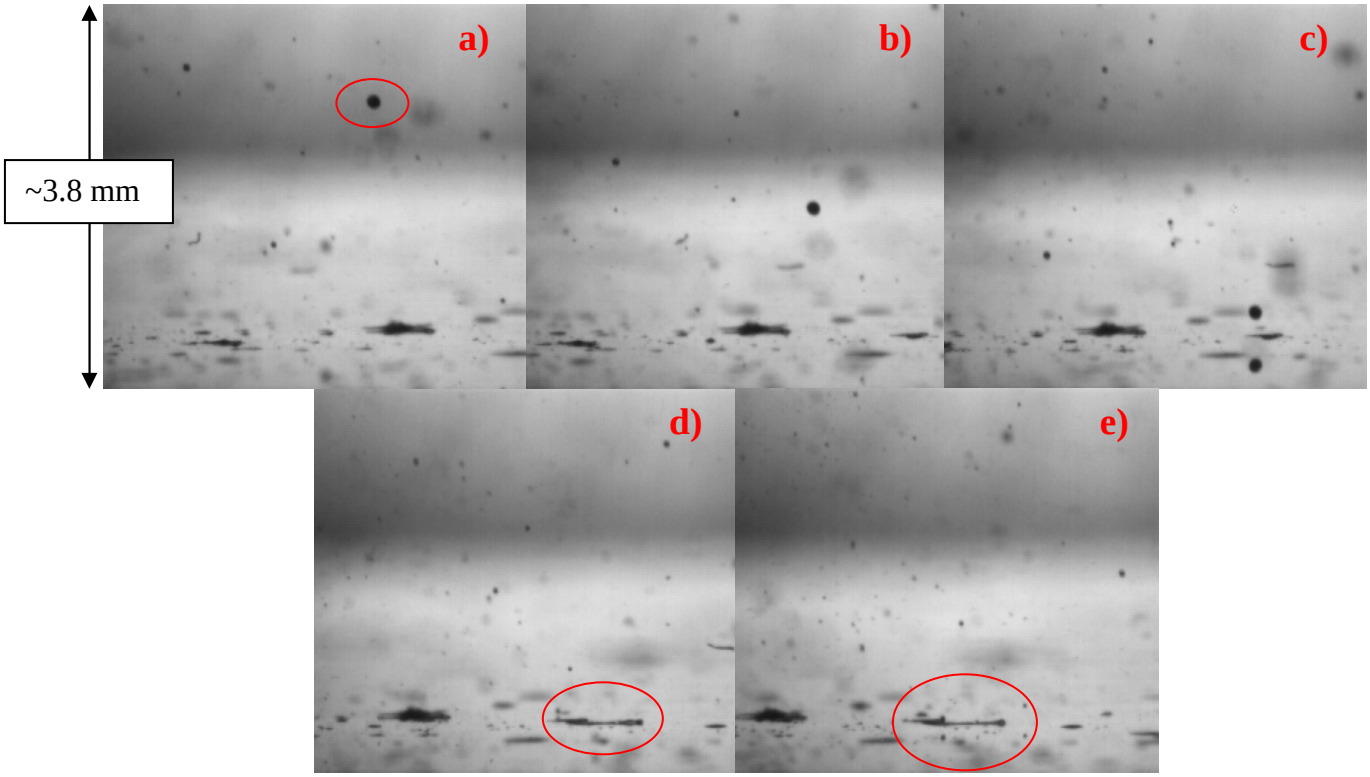

Figure 4.1: Xanthan gum droplet impingement (for the droplet of interest: d = 144µm, U_{normal} = 16.6 m/s, We = 692)

Comparisons were then made of the differing impaction behaviors amongst the rheological test liquids, with conclusions being inferred regarding the effect of certain

rheological properties on impaction behavior, particularly pertaining to splash (no occurrences of droplet rebound were noted for any of the test liquids).

Shown in Table 4.1 below is a compilation of impacting droplet diameter, the normal component of impact velocity, Weber number, Reynolds number, and Ohnesorge number for the nine test liquids used in this investigation based on a sample set of 40 droplets.

Table 4.1: Impinging droplet parameter ranges

	d (μm)	U_{normal} (m/s)	We	Re	Oh
Distilled Water	45 - 155	6.3 - 27.8	45 - 946	418 - 3099	0.009 - 0.016
50 wt.% Glycerin	47 - 121	5.1 - 27.0	23 - 1384	58 - 670	0.050 - 0.090
80 wt.% Glycerin	43 - 200	2.0 - 33.1	3 - 3152	2 - 151	0.370 - 0.800
100K PEO	45 - 211	0.8 - 29.3	1 - 1652	10 - 764	0.041 - 0.088
300K PEO	54 - 152	7.6 - 28.0	67 - 1433	103 - 611	0.051 - 0.085
1000K PEO	54 - 156	9.5 - 47.5	109 - 4517	131 - 1131	0.049 - 0.084
KELTRACK	44 - 191	3.3 - 27.9	16 - 2577	N/A	N/A
Xanthan Gum	42 - 220	5.9 - 26.5	29 - 2199	N/A	N/A
Carbopol®	45 - 255	7.3 - 30.9	48 - 1231	N/A	N/A

As noted from Table 4.1, the smallest droplet diameter able to be tracked and analyzed for impaction analysis was 42 microns. Droplets of diameter smaller than this were not accurately resolvable by the imaging system given the field of view dimensions (approximately 3.5 x 3.9mm). Even if droplets were able to be resolved, it was virtually impossible to track these extremely small droplets through multiple frames, particularly for the lower viscosity, inelastic liquids. The maximum velocities measured also had an upper limit on them which was also defined by the field of view window.

Also noted in Table 4.1, is the lack of Reynolds number and Ohnesorge number ranges for the KELTRACK, Carbopol®, and xanthan gum test liquids. Being that these three liquids exhibited shear-thinning behavior, it was very difficult to estimate a characteristic viscosity with which to use in droplet impact analysis (i.e. determination of Reynolds number and Ohnesorge number). Initially, an estimation of the shear rate experienced by a droplet upon impact was obtained and then using this shear rate, an appropriate shear viscosity was extrapolated from the shear curve of the liquid. However, due to uncertainties associated with timescale effects for the shear-thinning behavior (i.e. would the shear viscosity instantaneously react to the shear rates experienced upon impact or is there a relaxation time associated with it) and inconsistencies between the three shear thinning liquids as to the shear rates that were applied in the determination of

the shear curve, this approximation method was not used. Thus, for these three liquids, in order to eliminate uncertainty in trying to estimate an appropriate characteristic viscosity, droplet impaction behavior was characterized strictly with Weber number.

The large majority of droplets examined in this investigation impacted the surface at an oblique angle, with the angle α, shown in Figure 4.2, being defined as the impact angle. For the above-mentioned dimensionless numbers, only the normal velocity component of the impinging droplets was used. This is in agreement with Mundo *et al.* [1995].

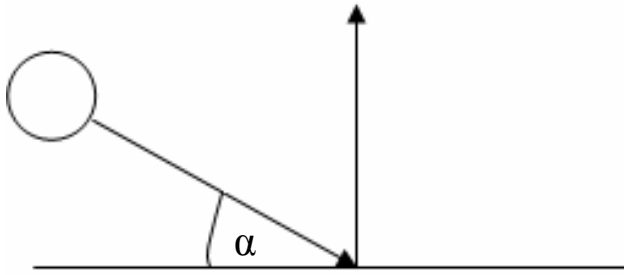

Figure 4.2: Definition of the impact angle

4.1.2 Splashing Considerations

If droplets were observed to splash within the initial sample set of forty, an additional sample set of strictly splashing droplets (approximately twenty were desired) was sought after in order to quantify splashing behavior and hopefully gain insight into the critical splash-deposition limit for each test liquid. This, however, proved to be problematic because in most cases (all but one test liquid), twenty additional droplets could not be found to splash, even after analysis of all the available data (i.e. high-speed videos comprised of hundreds of droplets) had been completed.

As can be expected, the larger FOV (relative to droplet diameter), coupled with the low imaging resolution, also made discerning droplet splash extremely difficult, if not impossible. Droplet splash was only able to be visualized with larger droplets, with diameters on the order of 100 microns and greater. This was due strictly to the fact that the secondary droplets and filamentary structures that were expelled away from these larger impacting droplets were large enough to be resolved by the imaging system. However, many smaller droplets traveling at high speeds, thus yielding Weber numbers on the similar order or even larger than large droplets traveling at lower speeds (Weber number is proportional to the square of velocity), were deemed not to splash, strictly

because the secondary droplets were unable to be observed; however, splash could very possibly be occurring.

Furthermore, due to the large field of view and low resolution, in many cases of droplet impact, it was very hard to distinguish whether or not droplets were impacting on dry surface or previously deposited liquid film, particularly for the water and the 50 wt.% glycerin solutions. Even a minute volume of liquid contained on the surface of the rail underneath an impacting droplet can significantly lower the splash threshold.

Although the current imaging setup provided an excellent macro view of droplet impaction behavior, which proved to be sufficient for gaining fundamental insight into spray-surface interaction, high-speed photographic analysis, with a relatively large FOV, made it extremely difficult, if not impossible, to establish statistically quantifiable droplet impaction conclusions. Therefore, as a result of numerous uncertainties for all test liquids, no firm conclusions could be drawn and an accurate critical splash-deposition limit for the test liquids was unable to be obtained in this analysis.

Even with the above-mentioned splashing uncertainties, an attempt was made to compare droplet impaction results for the Newtonian liquids to the widely accepted splash-deposition limit, defined as $K_L = WeOh^{-0.4}$. Typically, this relation is plotted as a function of non-dimensional surface roughness to obtain a splash-deposition curve. Mundo [1995], however, found this relation to be independent of surface roughness and although originally presented in a slightly different form, found this critical-splash deposition limit to have a value of 6.58×10^2 (Mundo's actual critical value was found to be 57.7). Therefore, being that the surface roughness of the rail used in this investigation was not measured, the value of $K_L = 6.58 \times 10^2$ was used for comparison purposes.

However, this splash-deposition limit only applies to three of the nine test liquids used in this investigation. As mentioned in Chapter 2, Crooks and Boger [2000] stated that this relation cannot be applied to elastic liquids and that the non-dimensional Weber, Reynolds, and Ohnesorge numbers, and non-dimensional surface roughness are not able to describe the splashing behavior of elastic liquids. They instead established a vertical shift factor which allowed for the prediction of the splash-deposition limit for an elastic liquid, based on the splash threshold for a reference Newtonian liquid, at a given value of non-dimensional roughness. They defined their shift factor as '*a*' and developed the relation:

$$K_L(E_R) = (1-a)K_L(E), \tag{4.1}$$

where $K_L(E_R)$ and $K_L(E)$ are the splash-deposition limits of a reference Newtonian liquid and an elastic liquid, respectively. They determined shift factors for four constant-viscosity Boger solutions, with shift factors of 0.57 and 0.87 for both a 300K and 1000K PEO solution, respectively. By plotting the four shift factors Crooks and Boger obtained as a function of molecular weight, a power-law relationship emerged. Using this power-law relationship, the shift factor for 100K PEO was interpolated and estimated to be approximately 0.36. By applying these shift factors to equation 4.1, splash-deposition limits for 100K, 300K, and 1000K PEO solutions were estimated to be 1028, 1530, and 5061, respectively. These limits will be discussed further in section 4.1.4 to see how they compare with the elastic results obtained in this investigation.

The author is unaware of any critical splash-deposition limits existing for shear-thinning liquids.

In all cases, only splashing to the right of the droplet was noticed (or spreading to the right if splash did not occur), opposite the direction of motion of the moving surface. This is believed to be primarily due to the impaction angle of the droplets but also could be related to moving surface and/or atomizing air jet effects.

4.1.3 Splashing Behavior of Inelastic Liquids

To examine the effect of shear viscosity on droplet impaction behavior, three glycerin-water solutions were sprayed and their droplet impaction was examined. These included both a 50 and 80 wt.% glycerin solution, as well as distilled water.

Firstly, as noted previously by Li *et al.* [2001], an increase in shear viscosity leads to an increase in mean droplet size. It was visually evident from observing the videos (however not reflected in the results shown in Table 4.1) for the three different Newtonian test liquids of varying shear viscosity that droplet size did indeed vary, with water having the smallest mean droplet size and 80 wt.% glycerin having the largest. However, statistically this cannot be determined from the videos because of the difficultly in identifying a sufficient number of droplets. A proper droplet sizing technique, such as shadowgraphy or phase Doppler particle analyzer, should be employed to obtain a more accurate measurement of droplet sizes.

It was noticed that the image quality of the cine videos degraded substantially during testing of water and 50 wt.% glycerin. This was believed to be due to the carrier air jet entraining a high percentage of the relatively small, low inertia droplets, thus reducing

the degree of contrast between the spray and background illumination. This fact alone made it extremely difficult to track very small droplets in these two test liquids and virtually impossible to see the expelling of secondary droplets upon droplet splash. In addition, the atomizing air stream deposited a substantial number of smaller droplets on the surface of the rail, thus leaving a scattered liquid film. On the other hand, for the other test liquids (80 wt.% glycerin and the elastic solutions), the surface remained relatively clean and dry.

4.1.3.1 Distilled Water

In the original sample set examined, only one droplet was noted to splash with a second droplet noted to be near the onset of splash. Additional instances of droplet splash were sought after; however, after going through numerous videos of water spray impaction, each containing hundreds of impacting droplets, only two additional instances of droplet splash were noted. For these cases unfortunately, though, velocity and impact angle information could not be obtained due to the impacting droplet appearing in only one frame before it impacted on the surface of the rail (thus indicating a relatively high velocity).

When comparing against the splash-deposition threshold, it was found that greater than 80% of the droplets reported critical K_L values greater than the limit found by Mundo *et al.* [1995] of 658, even though only two droplets were noted to splash. As expected, this result seems problematic; however, it does give validity to the assumption that droplet splash may actually be occurring for many cases where it was deemed to have not.

4.1.3.2 50 wt. % Glycerin

No splash was observed on the surface of the rail in the initial sample set taken. In all the impingement instances observed, the droplets impacted the surface and spread to the right. However, it is inconclusive to suggest whether or not these droplets splashed because most of them were too small to visualize. Upon examining hundreds of other droplets contained in numerous additional videos, still only a few cases of droplet splash were observed (the droplet however appeared in only one frame). One could possibly attribute this observation to not having reached the critical We #, due to an increase in shear viscosity; in comparing the 50 and 80 wt.% glycerin solutions, it is plausible that the critical Weber number for 50 wt.% glycerin lies between the maximum value of

Weber number determined in the 50 wt.% analysis of 1354 and the max value of the Weber number of the 80 wt.% glycerin of 3152 (where splashing occurred for the 80 wt.%), thus inferring that droplets with Weber numbers higher than their critical value were never actually observed for 50 wt.% glycerin. However, it is more likely again that droplet splash could not be discerned for the smaller impacting droplets. Similarly, when comparing to the splash-threshold limit, approximately 38% of the droplets reported critical K_L values greater than the limit of 658.

4.1.3.3 80 wt. % Glycerin

In the initial sample set taken, only one droplet was observed to splash. In all other cases, droplets spread slightly upon impact and remained deposited, with no signs of even the onset of splash. The one droplet that was observed to splash had a significantly higher Weber number (We = 3152) than other droplets in the analysis, possibly inferring that indeed the critical-splash deposition limit had not been reached in all other cases of droplet impact examined. Furthermore, after expanding the initial sample set size to contain hundreds of more droplets, no others signs of droplet splash were noted. In comparison to the splash-threshold limit, approximately 28% of the droplets reported critical K_L values greater than the limit of 658.

4.1.3.4 Inelastic Splashing Conclusions

Although the decreasing percentage of droplets that have critical K_L values greater than the splash-threshold limit can be perceived as possibly due to the increase in shear viscosity associated with going from distilled water to 80 wt. % glycerin, this trend is not strong enough to prove that droplet splash is suppressed with increasing shear viscosity. Thus, the effect of increasing shear viscosity and its known ability to increase the splash threshold cannot be accurately inferred from this investigation.

The splash-deposition limit given above ($K_L = WeOh^{-0.4}$) is strictly for Newtonian liquids. In all of the above inelastic test liquids, most significantly for water, a large percentage of droplets were deemed to have not splashed even though their calculated K_L values were much higher than the stated value of 658. This, as mentioned above, may be due to an incorrect observation being made as to whether droplet splash actually occurred or not. In addition, the author has recently learned that this stated value has been perceived to be low by other researchers in the field. The reasoning for this speculation is that the surface with which Mundo used as his impaction substrate was thought to be not

entirely removed of liquid (i.e. not a completely dry surface) before the next drop impinged upon it, which would have the effect of lowering the splash-threshold. No conclusions can be made as to whether or not this splash-threshold value appears to be low or not.

4.1.4 Splashing Behavior of Elastic Liquids

For all liquids, inelastic, elastic, and shear-thinning alike, prompt splash was the primary type of splash observed in this analysis. However, in comparing elastic liquid splash behavior to that of inelastic liquid splash behavior, it became immediately obvious that splashing of elastic liquids was considerably different. Splash, defined as the production of secondary droplets, resulted in a number of secondary droplets being expelled from the periphery of the expanding lamella for inelastic liquids. However, for splashing of elastic liquids, although secondary droplets were observed to form, they tended to remain attached to the parent drop via thin filamentary ligaments. An example is shown below in Figure 4.3. This was also noticed by Crooks and Boger [2000]. With enough impact energy, these secondary drops attached via ligaments would eventually break away and more often than not, be entrained in the atomizing air jet traveling along the surface of the rail. Thus, when analyzing the elastic liquids, splash was further classified into two distinct outcomes: 1) Secondary droplets are produced and expelled from parent droplet but still remain attached via ligaments, and 2) Secondary droplets and filamentary ligaments are expelled from parent droplet, having been completely detached from the parent drop. The second case leads to overspray and a reduction in transfer efficiency.

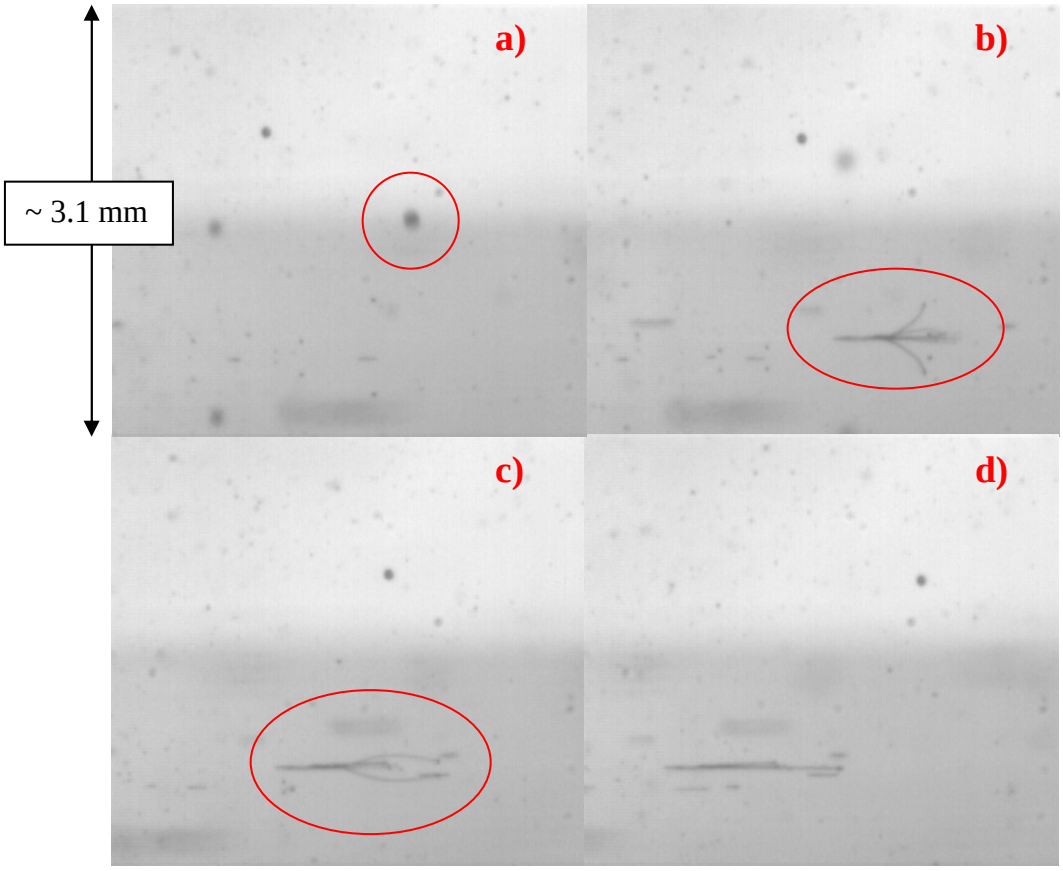

Figure 4.3: Splashing of 100K PEO droplet with secondary droplet attached to parent drop via ligament

Finally, similarly for the elastic liquids as with the inelastic liquids, it was very hard to distinguish droplet splash for smaller droplets impacting the surface of the rail, thus introducing an element of uncertainty into the analysis.

4.1.4.1 100K PEO

Approximately 25% of the droplets in the initial sample set were observed to splash (actually, more droplets were observed to splash however they appeared only in one frame and thus, impaction info could not be extracted). As a means of further examining droplet splash behavior, a secondary sample set, consisting of approximately twenty splashing droplets (this was all that could be obtained after examining numerous spray impaction videos), was established. In combining both sample sets, non-splashing droplets were found to have a splash threshold range of $172 \leq K_L \leq 5183$, with approximately 85% of these droplets having splash threshold values less than 2100, with splashing droplets having a splash threshold range of $1790 \leq K_L \leq 12508$, with 90% of

the droplets having splash threshold values greater than 2100. This relationship can be seen in Figure 4.4, shown below.

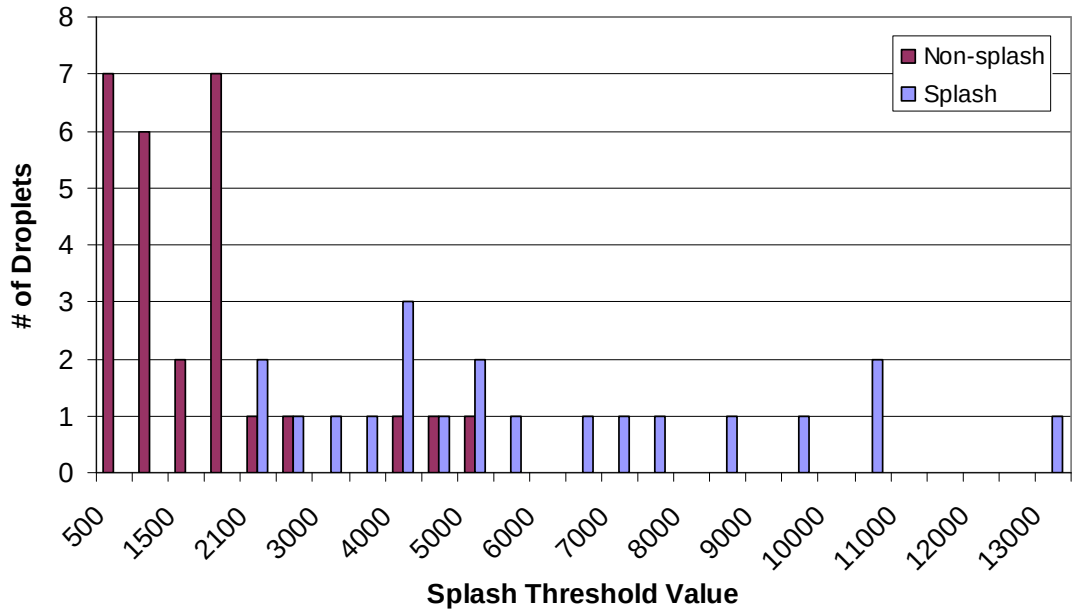

Figure 4.4: Frequency of droplet splash and corresponding threshold values

Based on Figure 4.4, an approximate critical splash-threshold can be estimated to be near 2100 or slightly above. Based on the number of uncertainties associated with this method of analysis, this estimation is problematic but one that provides some insight into droplet impaction behavior for an elastic liquid. A significantly larger sample set should be obtained to properly quantify an appropriate splash threshold.

However, in comparing this value of 2100 to the critical value interpolated using the method proposed by Crooks and Boger [2000] (approximately 1028), it can be seen that our value is significantly higher. The author is unaware as to what could contribute to this discrepancy, other than the large inaccuracy in using such a small sample set and again, the poor ability of the imaging system to discern droplet splash.

An additional point of interest is that a significantly larger number of droplets were observed to splash upon impact than when compared with the other test liquids, particularly when comparing against water and 50 wt.% glycerin (as displayed by the occurrence of splashing droplets in the initial sample set). This seems contradictory because as previously mentioned in Chapter 2, it is well known in literature that, when compared to inelastic liquids, the addition of polymers acts to inhibit splashing.

However, as already discussed in section 4.1.3, it was assumed that many inelastic droplets actually were splashing even though they appeared to not. Due to the larger droplets produced upon atomization of elastic liquids and the absence of the dark atomizing air jet, splash was more easily discerned. Therefore, the author attributes this "illusion" to, once again, inadequate imaging on the micro level.

Upon splash of 100K PEO droplets, secondary droplets connected via filamentary structures were released from the periphery of the expanding droplet. If these filamentary structures detached from the parent droplet, they either deposited on the surface of the rail or if they were small enough, were carried away by the atomizing air jet. This contributed to overspray and a reduction in transfer efficiency. Although shown for a 300K PEO beads-on-string ligament, an example of secondary droplets and filamentary structures being carried away by the surface air jet can be seen in Figure 4.12, with the direction of the surface air jet illustrated by the red arrow.

4.1.4.2 300K PEO

In addition to the impaction of ligaments (which will be discussed later in section 4.2), a large number of droplets were also observed impacting the rail. However, only one instance of droplet splash was noted within the initial sample set. Furthermore, after further examination of the complete data set, only one other instance of droplet splash was noted where impaction information could be gathered. There were other occurrences of droplet splash that were observed however, they could not be analyzed, again due to high droplet velocity causing the droplet to only be in one frame. The one occurrence of droplet splash had the highest value of Weber number reported in Table 4.1, with the second occurrence having a Weber number that fell within the top 80% of the distribution.

The approximated critical splash threshold value found using the method proposed by Crooks and Boger [2000] was approximately 1530. Both instances of splash had critical values greater than this (4359 and 2468), however, so did 14 other droplets deemed to have not splashed. Based on only two instances, no inferences can be made regarding a critical splash threshold value seen for this liquid in our investigation but it is expected to be higher than the value calculated using Crooks and Boger's method.

In comparison with 100K PEO, the significantly fewer droplets observed to splash with the 300K PEO can be attributed to an increase in elasticity associated with the higher molecular weight of polymer.

Splashing however was noted due to droplet impact on a previously existing liquid film. This in turn caused large-scale filamentary structures to rise up and thus, be entrained and carried away by the surface air jet.

4.1.4.3 1000K PEO

No signs of droplet splash occurred during the entire examination of spay impaction of 1000K PEO. Due to a slightly different imaging setup employed when examining 1000K PEO, allowing for a larger FOV, slightly higher droplet velocities were able to be examined. As a result, Weber numbers were correspondingly higher as well. Twenty percent of the droplets examined within the initial sample size had Weber numbers greater than the highest Weber number examined in the 300K PEO analysis. Even with these larger Weber numbers, the critical splash threshold was never reached. This complete lack of splashing, for similar Weber number ranges as experienced with the other two PEO solutions, can be attributed to an increase in liquid elasticity with the 1000K PEO.

Similarly for 1000K PEO, when comparing to the splash threshold value of 5061 stated by Crooks and Boger [2000], 80% of the non-splashing droplets fell under this limit. However, being that no droplets were observed to splash, no real comparisons or conclusions can be made regarding this limit.

4.1.4.4 Elastic Splashing Conclusions

Although unable to be justified with droplet impaction results, an increase in liquid elasticity had the effect of reducing the number of droplets observed to splash, with 100K PEO having the greatest number to 1000K PEO, where no droplet splash was observed at all.

Furthermore, due to the uncertainties associated with the drop impact analysis for the inelastic liquids, no conclusions can be made regarding elastic liquids having higher splash thresholds than Newtonian inelastic liquids.

A significantly larger sample set must be used in order to firstly compare splash threshold limits for the elastic liquids to those estimated by Crooks and Boger [2000] and secondly, to possibly estimate our own shift factors based on this investigation. Keep in mind though, as was mentioned for the inelastic case, the splash threshold of 658 for inelastic liquids (which was used to determine the splash threshold for the elastic liquids), has been considered to be low, which gives validity to the inference that our

splash threshold values for the elastic liquids are larger than those estimated using the method proposed by Crooks and Boger.

4.1.5 Splashing Behavior of Shear-Thinning Liquids

As mentioned in section 4.1, both Reynolds and Ohnesorge numbers were not calculated for the three shear-thinning liquids used in this analysis. Thus, only Weber number was used as the sole parameter to characterize droplet splash for these liquids.

The Carbopol® solution used in this analysis had been dyed with ink in order to allow for significant contrast when imaging. It was later learned however that the addition of the ink affected the properties of the Carbopol® solution in that it lowered the yield stress from approximately 0.55 Pa to 0.08 Pa, as well as lowered the shear curve, as shown below in Figure 4.5. The new consistency and power-law indices for the inked Carbopol® solution are 435.66 mPa-s^n and 0.318, respectively.

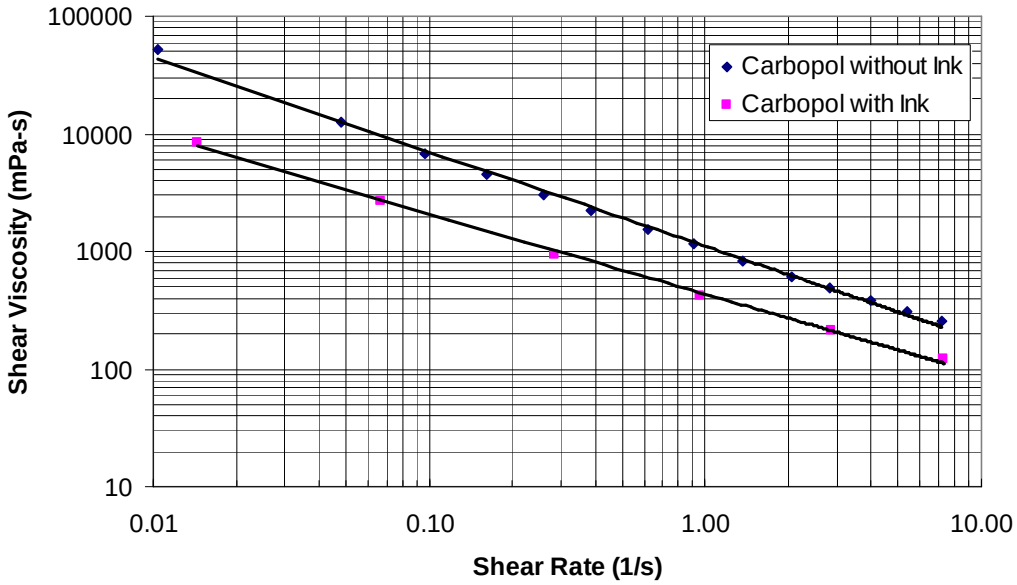

Figure 4.5: Effect of ink on Carbopol® shear curve

The true effect that the addition of the ink had on the Carbopol® polymer structure is unknown. Ideally, extensional viscosity and surface tension measurements both before and after the addition of the ink would have been taken but were unable to be performed.

Carbopol® and xanthan gum both exhibit shear-thinning behavior; however, Carbopol® also exhibits viscoplastic behavior and xanthan gum is believed to be elastic. Xanthan's elasticity is highlighted by the visualization of large discrete ligaments and

filamentary structures upon atomization immediately downstream of the nozzle, shown in Figure 4.6 below.

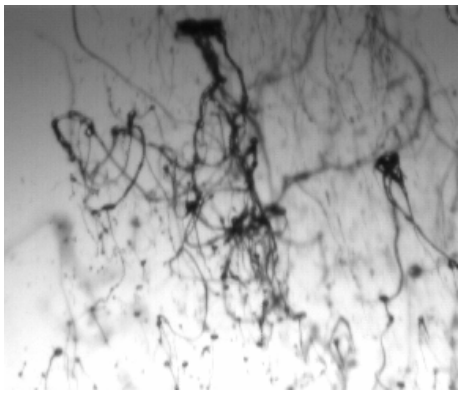

Figure 4.6: Breakup of xanthan gum 7.5 mm downstream of the nozzle

Unfortunately, extensional viscosity measurements of both the Carbopol® and xanthan gum solutions were not taken. The elastic nature of Carbopol® is unknown however it is believed to be very mildly elastic at this concentration. The breakup of Carbopol® 7.5mm downstream of the nozzle is illustrated in Figure 4.7.

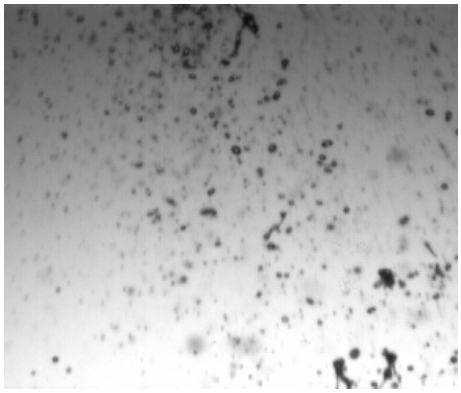

Figure 4.7: Breakup of Carbopol® 7.5 mm downstream of the nozzle

4.1.5.1 Carbopol®

Within the initial sample set taken, only one droplet was observed to splash. After further examination of the entire data set, 14 additional droplets were found to splash. The non-splashing droplets had a Weber number range of $48 \leq We \leq 1231$, with the splashing droplets having a range of $282 \leq We \leq 2579$. A strong correlation could not be found between splashing and non-splashing droplets in terms of the Weber number. This

was not entirely surprising based on the fact that Weber number alone cannot be used to describe the droplet impaction process, particularly for non-Newtonian liquids.

4.1.5.2 Xanthan Gum

Similarly, for xanthan gum, within the initial sample set taken, only two occurrences of droplet splash were noted. Upon the collection of the second sample set, an additional 13 droplets were found to splash. The non-splashing droplets had a Weber number range of $29 \leq We \leq 1850$, with the splashing droplets having a range of $824 \leq We \leq 2949$. In this case however, 85% of non-splashing droplets had Weber numbers less than 1300 whereas 80% of splashing droplets had Weber numbers greater than 1300. This may possibly infer that there exists a splash threshold corresponding to a Weber number of approximately 1300.

4.1.5.3 Shear-Thinning Splashing Conclusions

Based on the impaction behavior of Carbopol® and xanthan gum, no conclusions can be drawn pertaining to the critical splash thresholds of these two liquids. In addition, the effect of shear thinning behavior on droplet impaction in relation to the effect of elasticity and shear viscosity cannot be quantified from this analysis. As mentioned above, Carbopol® exhibits viscoplastic behavior and xanthan is believed to be mildly elastic. In order to properly quantify the effect of shear-thinning, this property must solely be isolated from any elastic or viscoplastic behavior as with these test liquids, we cannot accurately quantify exactly which rheological property is influencing droplet impact.

4.1.6 KELTRACK

No signs of droplet splash occurred during the entire examination of spay impaction of KELTRACK. All droplets spread slightly and remained on the surface of the rail. Droplet splash was only noticed if droplets impinged upon a previously existing liquid film and even then, the splash was relatively contained, with virtually no secondary droplets or filamentary structures being entrained by the atomizing air jet. KELTRACK's droplet impaction behavior exhibited strong resemblance to that of 1000K PEO, where no droplet splash was observed as well.

4.1.7 Spray Impact Conclusions

The droplet impact analysis described above was not designed to be a splashing impact analysis as a means of determining a critical splash-deposition limit. The analysis was meant to provide insight into transfer efficiency improvement methods by examining droplet impaction behavior for a number of rheologically defined test liquids. As mentioned in Chapter 2, Dhiman and Chandra [2005] note that spray analysis using high-speed imaging with the intent of extracting quantifiable data is extremely difficult, owing to the small physical scale of the liquid features and high velocities at which they travel. As a means of significantly improving this droplet impaction analysis, two cameras, with higher acquisition frame rates, should be employed; one should be positioned so as to track droplets through multiple frames with the other being positioned so as to strictly examine impaction behavior (i.e. very small FOV). This would allow for significantly improved imaging and thus, distinguishing of droplet splash, as well as allow a greater number of high-velocity droplets to be included in the statistical sample set. Furthermore, an additional method of accurately quantifying the effect of these rheological properties on droplet impaction behavior would be to examine the droplet impaction process on a more macro scale (i.e. droplets with much larger diameters) with a consistently repeatable experimental setup.

In addition to the numerous above mentions of variables affecting the ambiguity of this droplet splash analysis, a few other additional considerations can be noted. The aerodynamic flow fields present in the immediate vicinity of the spray could very possibly impose significant droplet spin. This, in turn, could have a significant effect on droplet impact outcomes. It was also extremely difficult to ensure that the droplets were impacting on a dry surface in all cases; even the slightest presence of a liquid film would lower the splash threshold. Finally, the uniformity of the surface roughness on the rail was never measured. It is well known that surface roughness significantly influences droplet impact outcome; slight differences in surface roughness over the length of the rail (i.e. surface polish non-uniformities, scratches, etc.) could substantially influence the splashing behavior from one droplet to the next.

Accurate and clear comparisons regarding the influence on droplet impact outcome between shear thinning behavior, viscoelastic behavior, and inelastic behavior cannot be inferred from this analysis.

Finally, as Rioboo *et al.* [2001] notes, the droplet impact outcomes shown in Figure 2.1, cannot solely be defined using K_L, Weber number, Reynolds number, and Ohnesorge number, even for Newtonian liquids as these dimensionless groups do not make allowance for surface wettability and roughness effects. This therefore instills a sense of caution when attempting to compare against the critical splash threshold, as was done in the above analysis.

4.2 Viscoelastic Effects

4.2.1 Ligaments and Filamentary Structures

As mentioned above, Li *et al.* [2005] noticed the formation of filamentary structures and ligaments upon atomization of three varying molecular weight PEO elastic test solutions (100K, 300K, and 1000K) and the industrial LFM (KELTRACK). These filamentary structures and ligaments are shown in Figure 4.8 as breakup photographs for 100K PEO, 300K PEO, 1000K PEO, and KELTRACK, respectively. For 300K PEO, 1000K PEO, and KELTRACK, these ligaments and filamentary structures remained intact until they reached the surface of the rail, located 67mm beneath the nozzle. As a result, these three test liquids were observed to have ligaments impacting the surface of the rail. Although Li *et al.* observed the formation of filamentary structures for the 100K PEO elastic solution near the atomizer, due to this sample's reduced elasticity, the ligaments formed eventually collapsed into discrete droplets under the action of capillary forces before reaching the rail surface. This was also noted to be the case for xanthan gum as although ligaments and filamentary structures are shown to be present immediately downstream of the nozzle in Figure 4.6, no ligaments were observed impacting the rail surface.

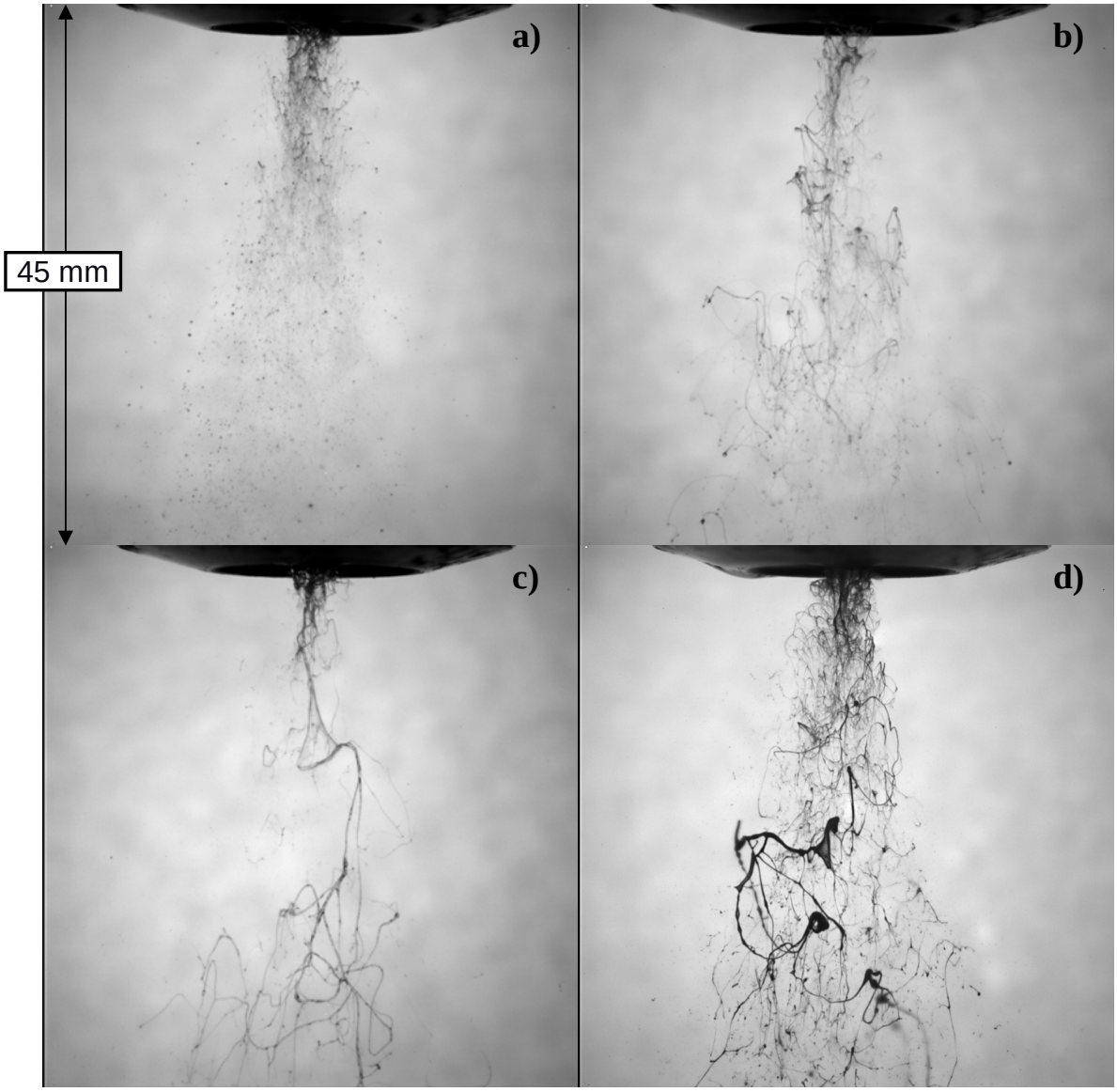

Figure 4.8: Breakup of a) 100K PEO b) 300K PEO c) 1000K PEO d) KELTRACK (Photographs courtesy of Li *et al.* 2005)

4.2.2 Ligament Classification

The ligaments observed impacting the surface of the rail can be broadly classified into four main structures: beads-on-string, bulbous tip, string, and membrane. Examples of each are shown in Figure 4.9. Note that only KELTRACK ligaments are shown to define the classifications.

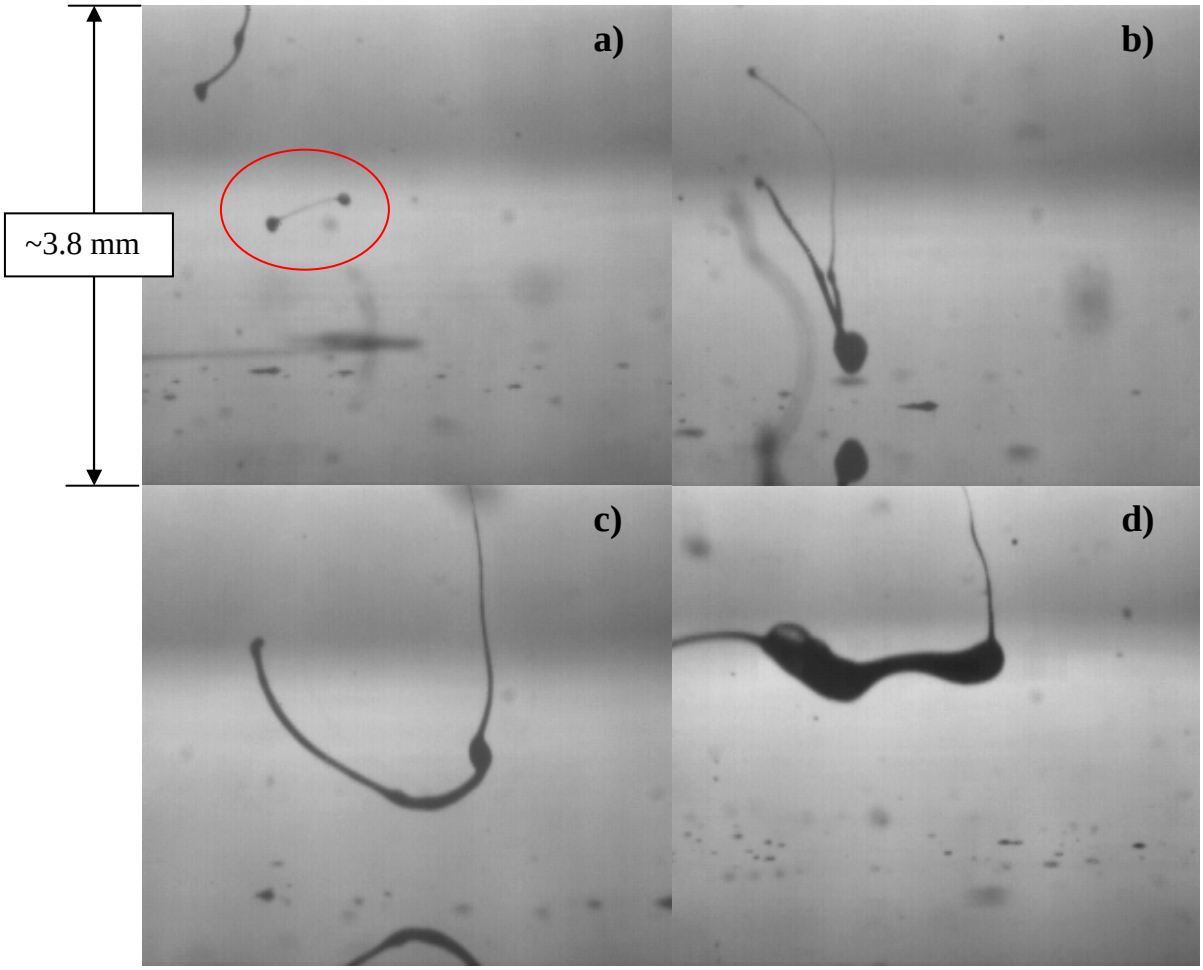

Figure 4.9: KELTRACK ligament structures: a) beads-on-string b) bulbous tip c) string d) membrane

Beads-on-string [Goldin *et al.* 1969] structure ligaments are defined by a minimum of two droplets connected by a filamentary ligament, with the diameter of the ligament being considerably smaller than the diameter of the droplet. These structures had as many as five or six droplets per filament. Structures looking as if they were “dog bone” shaped continued to break up, were elongated, and eventually became beads-on-string. Many of these beads-on-string structures fell to the influence of capillary forces and broke up into definite bulbous tip structures. This structure was defined by a droplet at the end of one or more filamentary ligaments, usually with its diameter being relatively large compared to the width of the ligament. The third structure, noted as the string, was clearly that; a long thin cylindrical filamentary structure with relatively constant diameter (droplets on end of filament were on same order of diameter). Finally, the fourth structure noted was the membrane. This was defined as any non-spherical compilation of ligaments that

contained at least three or more appendages and may be joined together. It was clearly seen however that the majority of ligaments impacting the rail were the beads-on-string and bulbous tip structures.

4.2.3 Ligament Impaction

4.2.3.1 KELTRACK

The majority of liquid delivered to the surface of the rail was in the form of large-scale ligaments and not the typical spherical droplets. The total percentage of liquid volume residing in droplets can be considered small relative to the percentage residing in ligaments.

In every case of KELTRACK ligament impaction, there were never any visible signs of splash on a dry surface. The ligaments impacted the surface, underwent minimal spreading, and remained deposited. Splash was observed only when a ligament impacted onto a previously deposited liquid film. This situation occurs when the leading surface of an incoming ligament impacts and deposits on a dry surface, but the remainder of its structure impinges onto itself, thereby initiating splash. In addition, ligament or droplet rebound was not observed in any of the videos. Thus, based on these observations, KELTRACK's current rheological formulation, which cannot be revealed due to propriety considerations, proved to be very effective in keeping sprayed liquid on the surface of the rail. A KELTRACK bulbous tip ligament impacting the surface is shown in Figure 4.10. Please note that for this figure, and all others in this section which contain a series of sequential images, the time separation between images is 64µs. The one exception to this is Figure 4.12 which had a time separation of 37µs.

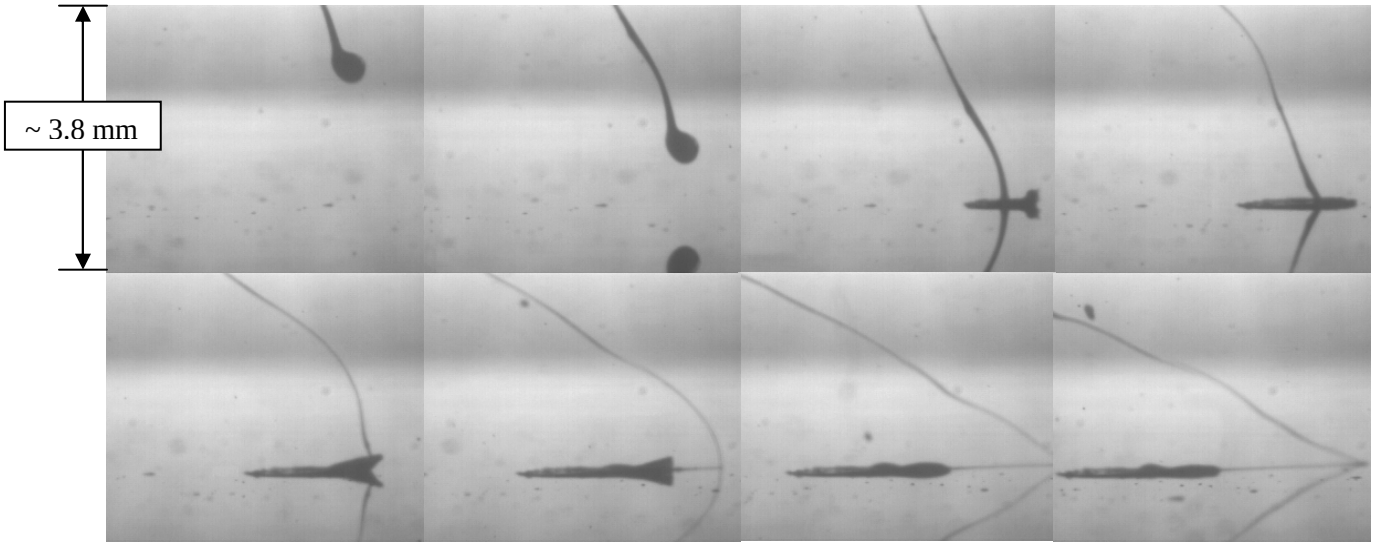

Figure 4.10: KELTRACK bulbous tip ligament impaction

4.2.3.2 300K PEO

As noted with KELTRACK, primary liquid deposition on the surface of the rail was through the impaction of ligaments and not with droplets. The ligaments inherent in the atomization of the 300K PEO elastic solution were classified into both the bulbous tip and beads-on-string structures, shown in Figure 4.11.

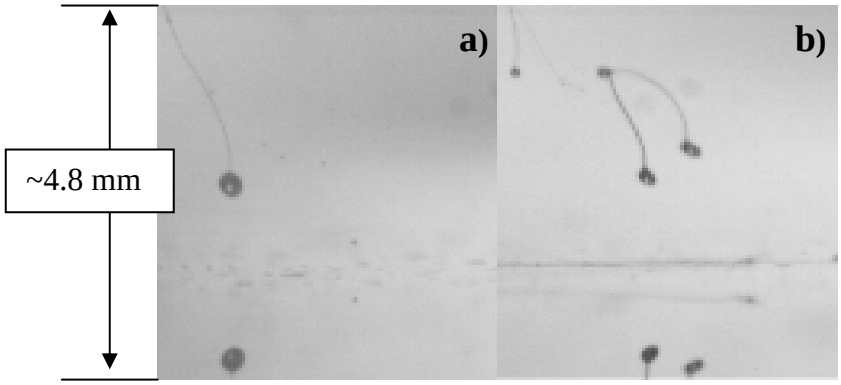

Figure 4.11: 300K PEO Ligament structures: a) bulbous tip b) beads-on-string

Upon impacting the rail surface, the majority of ligaments were observed to splash, with firstly ligaments, and then secondary droplets jetting outwards from the periphery of the lamella on the right side of the droplet. Again, only splashing to the right of the droplet was noticed (opposite to the direction of motion of the moving surface) due to reasons previously discussed.

It was noticed that there was significant overspray generated due to the splashing of these ligaments. Upon impact and then splash, filamentary structures broke away from the impacting ligament and were carried away by the atomizing air jet along the surface of the rail. This, of course, is detrimental to spray coverage and will significantly reduce the transfer efficiency. Surprisingly, such phenomenon was not noticed for the industrial LFM in any case; this was apparent in examining droplet and ligament impact, as well as noticing the lack of filamentary structures moving horizontally through the field of view. A 300K PEO ligament impacting on the surface with its subsequent splash is shown in Figure 4.12.

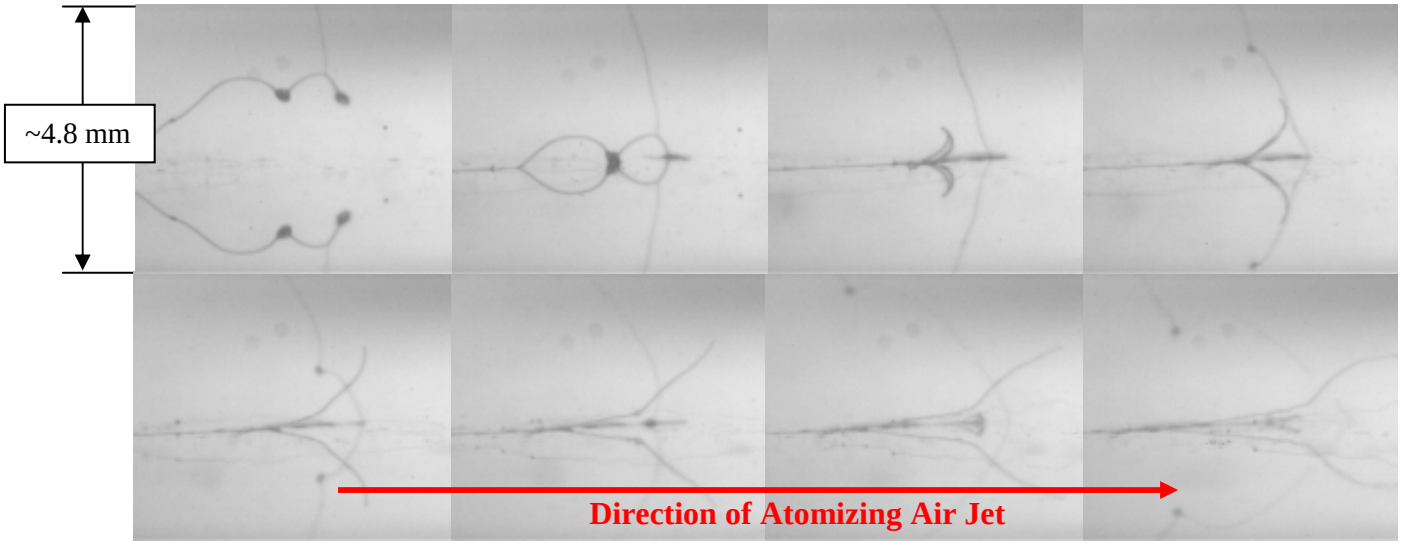

Figure 4.12: 300K PEO beads-on-string ligament impaction

4.2.3.3 1000K PEO

Even more-so than with 300K PEO and KELTRACK, the majority of liquid delivered to the surface of the rail was in the form of ligaments. The total percentage of liquid volume residing in droplets was extremely small relative to the percentage residing in ligaments. Ligaments were primarily of the bulbous tip and beads-on-string structures but there were also large numbers of string type ligaments (pictures will not be shown due to similarity with 300K PEO ligaments, shown above).

Upon impaction on the surface, in contrast to 300K PEO, a very large percentage of these ligaments were observed not to splash, with only a few splashing cases observed for very large ligaments or when impinging upon a previously deposited liquid film. The ligaments instead spread and remained on the surface of the rail. Even with ligaments experiencing the onset of splash, splash was still suppressed and did not occur. This very

much resembled the ligament impaction behavior of KELTRACK. Shown in Figure 4.13 are two separate cases of 1000K PEO bulbous tip ligaments impacting the rail surface. In both these occurrences, the onset of splash is evident however there is no expelling of secondary droplets or filamentary structures from the edge of the expanding lamella.

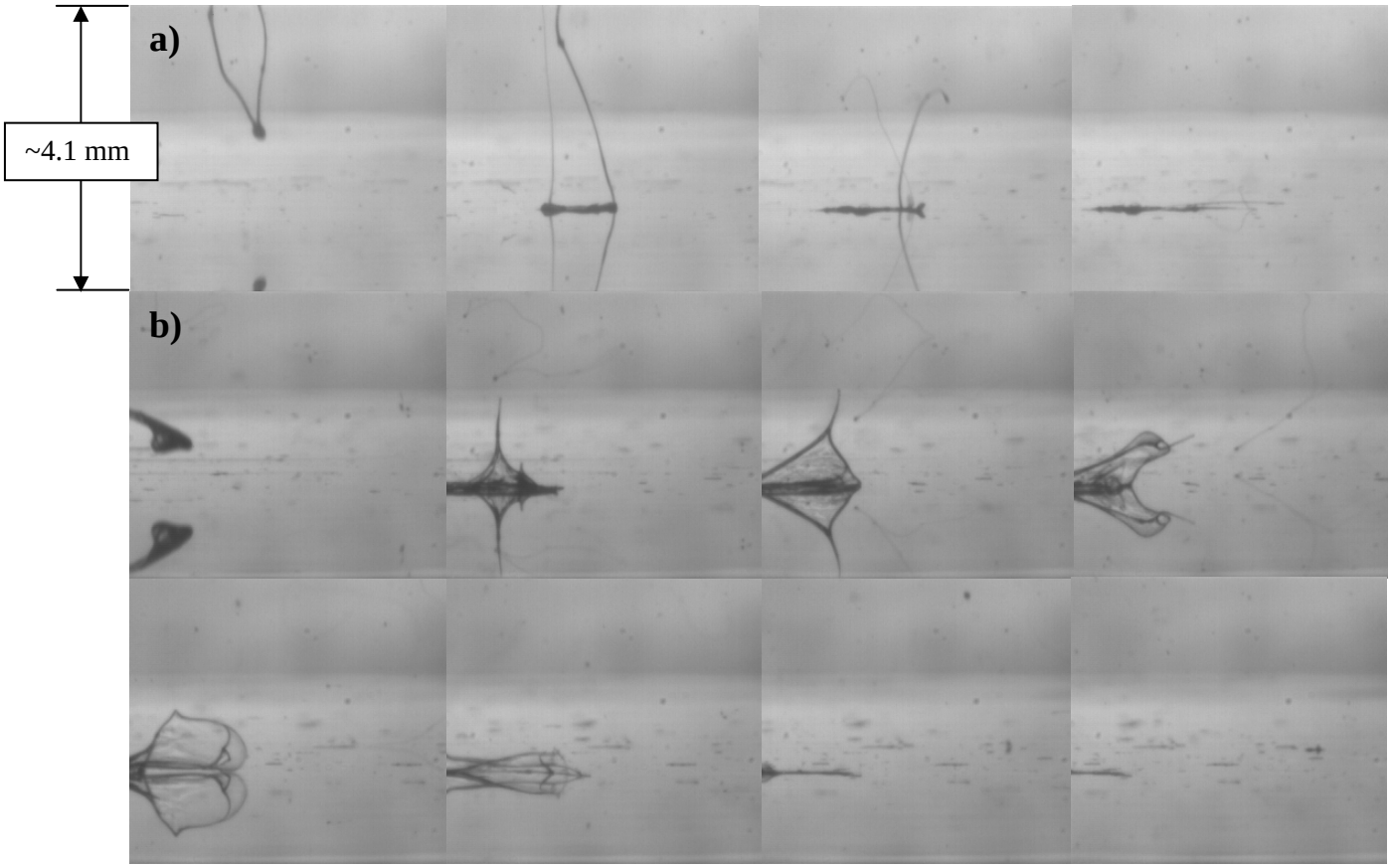

Figure 4.13: 1000K PEO bulbous tip ligament impaction

For the few cases that splash does occur with these large ligaments, secondary droplets and filamentary structures are expelled into the atomizing air stream, just the same as with 300K PEO. Although the occurrences are significantly less frequent, there are still signs of overspray and thus, still a slight reduction in transfer efficiency.

Actually, it is surmised that a significant percentage of the overspray (although total overspray is still relatively little) seen in examining the videos for 1000K PEO is attributed to the entrainment of low inertia lightweight ligaments, as well as the detachment of the filamentary tail from the impacting ligament immediately upon impact. When these ligaments impact, the impact forces causes these filamentary structures to break away from the impacting droplet and due to their low inertia and light

weight, they are carried away by the atomizing air jet. This can be seen in Figure 4.14 shown below. The long lightweight trailing filamentary structures are detached from the impacting droplet, immediately entrained by the atomizing air jet, and carried along the surface of the rail. This however was not noticed with KELTRACK.

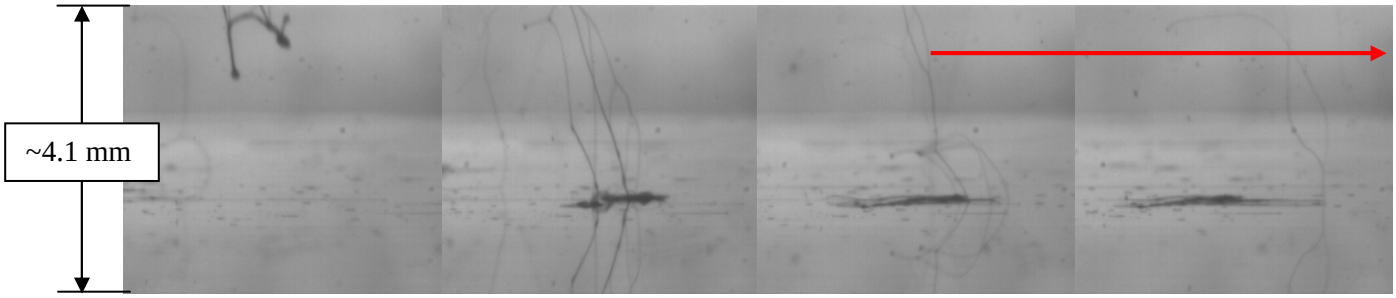

Figure 4.14: Entrainment of 1000K PEO ligament tail upon impact

It was also noticed that there were significantly more ligaments and fewer large discrete droplets impacting the surface with 1000K PEO than when compared to the other elastic test liquids. This can be attributed to 1000K PEO's increased elasticity. Beads-on-string and bulbous tip ligaments were carried downstream of the nozzle and eventually broke up under the action of capillary forces, with the tail ligament being detached from the bulbous tip, as shown below in Figure 4.15 for 300K PEO (in this figure however, the break up most likely occurs due to interaction with the atomizing air jet). However, due to the increased elasticity associated with a higher molecular weight polymer, 1000K PEO filamentary structures did not break up into discrete droplets but instead remained relatively intact immediately near the surface of the rail; thus, a greater number of ligaments and fewer droplets were observed impacting the surface.

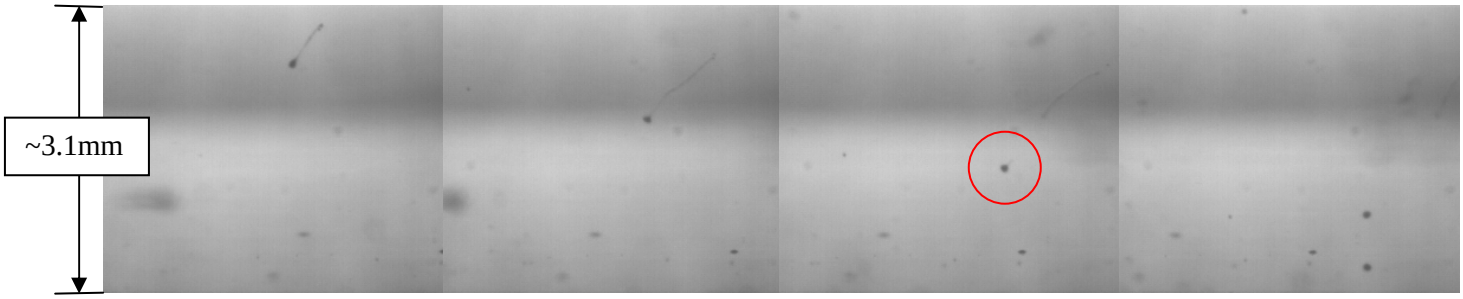

Figure 4.15: Breakup of 300K PEO beads-on-string ligament into discrete droplet

4.2.4 Elastic Liquid Impingement Conclusions

In examining the effect increasing elasticity has on droplet impact behavior, two observations can be noted: 1) the splash threshold is increased, and 2) for a given downstream distance from the nozzle, an increasing number of ligaments and a fewer number of droplets are observed to impact the rail. The second observation is a result of reduced atomization which allows for ligaments to remain intact at a further downstream distance from the nozzle. This has the effect of reducing overspray losses as these larger ligaments are not as easily entrained by the atomizing air jet due to larger inertia.

On a similar note, an obvious difference noted between the impaction of KELTRACK and the impaction of the elastic liquids was a significantly far fewer number of very small lightweight tails and filamentary structures with KELTRACK. As mentioned above, these lightweight filamentary structures and string type ligaments were detached and then entrained in the atomizing air jet upon impact of bulbous tip and beads-on-string ligaments and thus, contributed to overspray. This was not noticed with KELTRACK. This may be an effect of KELTRACK's lower surface tension; essentially, the lower value of surface tension would provide a reduced tendency (reduced capillary forces) to break up and form discrete droplets. As a result, KELTRACK's ligaments would be less spherical in shape (which was noticed) and have larger diameter cylindrical "tails" or filamentary structures connected to them. This increased volume provided these filamentary structures with enough inertia to resist the entrainment tendency of the atomizing air jet and thus, settle on the surface of the rail. Therefore, it is surmised that KELTRACK's low value of surface tension assists in its excellent spray coverage abilities in, not only allowing increased spread upon impact, but also resists the breakup of ligaments so as to minimize overspray.

Therefore, there seems to be a trade-off when dealing with viscoelastic atomization; due to the relatively larger droplets inherent upon atomization of elastic liquids, it can be inferred that a larger percentage of these higher inertia droplets will reach the impaction surface, as opposed to getting entrained by the atomizing air jet on the surface of the rail. However, these elastic liquids also produce light weight filamentary structures which break up and pull away from the droplets due to the action of capillary forces. These ligaments and filamentary strings are entrained by the atomizing air jet and lead to a reduction in transfer efficiency. Therefore, elastic liquids with low surface tension may prove to be beneficial in ensuring high transfer efficiency.

4.3 Improvement of Transfer Efficiency

4.3.1 Introduction

In order to assess the transfer efficiency of a given spray deposition process, knowledge of two areas must be obtained:

1) The amount of sprayed liquid which actually reaches the intended target after it leaves the nozzle, and
2) Spray-surface interaction behavior (i.e. does the sprayed liquid remain on the surface upon impact or is it expelled away?).

Sections 4.1 and 4.2 provide a detailed look into the latter of these two areas. In addressing the first area with regards to air-blast atomization, two questions need to be asked: 1) What percentage of the spray is actually reaching the target surface and not being entrained by the atomizing air-jet which travels along the surface?, and 2) Is the spray relatively well confined to the dimensions of the intended target surface (i.e. is there overspray)? These two questions will be addressed here.

4.3.2 Droplet Entrainment

4.3.2.1 Theoretical Determination of Entrained Droplet Size

As noted by Weiss [2005], when the atomizing air, co-flow with the spray, impinges on a wall, a stagnation zone is developed and the flow is bent from its original free stream direction and directed radially outwards as a wall-jet (known as the atomizing air jet in this thesis) along the surface of the wall (i.e. rail). Suspended small droplets with negligible inertia may follow these streamlines and escape impact on the wall by entrainment whereas larger droplets, with larger inertia, may tend to continue in a straight line, disregarding streamline path. Droplets that follow the curved streamlines can be described as having curvilinear motion. The dimensionless Stokes number (*Stk*) is used to characterize curvilinear motion and is defined as the ratio of the stopping distance of a droplet to a characteristic dimension of the obstacle [Hinds 1999]. The stopping distance is defined as the distance the particle continues to travel in its original direction before coming to rest. Stokes number in the Stokes regime ($Re_d < 1$) is defined as:

$$Stk = \frac{S}{D} = \frac{\tau_R U_o}{D}, \tag{4.2}$$

where U_o is the relative velocity between the droplet and the medium (approximated to be around 45m/s), and τ is the particle's relaxation time, defined as the time needed for

the particle to adjust its velocity to new flow conditions and is restricted to Stokes regime conditions. The Reynolds number for a droplet is defined as:

$$\mathrm{Re}_o = \frac{\rho_g U_o d}{\mu_g}, \tag{4.3}$$

where ρ_g and μ_g are the density and viscosity of the medium (i.e. air), and d is the diameter of the droplet.

However, in this analysis, we are dealing with droplet Reynolds numbers significantly higher than unity and as a result, an empirical correlation [Mercer 1973] must be used to define the stopping distance (for Re < 1500), given as:

$$S = \frac{\rho_l d}{\rho_g}\left[\mathrm{Re}_0^{1/3} - \sqrt{6}\arctan\left(\frac{\mathrm{Re}_0^{1/3}}{\sqrt{6}}\right)\right], \tag{4.4}$$

where ρ_l is the liquid density of the droplet. In using the distance between the nozzle and the rail surface (67 mm) as the characteristic dimension, Stokes numbers were calculated. When Stk >>1, particles continue moving in their initial direction when the streamlines are bent and if Stk << 1, particles follow the curvilinear streamlines [Hinds 1999]. Droplets within this Stokes number range will have motion lying between these two limits. Based on these limits and for all the test liquids (water and 80 wt.% glycerin having the lower and upper limits on liquid density, respectively), it was found that particles with diameters less than 6-7 µm would follow the streamlines where as diameters greater than 93-106 µm would be able to completely maintain their initial path. Thus, theoretically, droplets with diameter greater than 6-7 µm should be observed to impact the rail, however with a large majority of them having a potentially influenced trajectory.

When compared to an estimation done by Weiss [2005], who showed that the upper limit of potentially entrainment-affected droplet sizes for a spray impinging onto a vertical wall lied in the range of 50–100 micrometers, the above estimation seems quite reasonable.

4.3.2.2 Experimental Estimation of Entrained Droplet Size

As previously mentioned, due to the formation of larger discrete droplets when atomizing elastic liquids (discussed in Chapter 2), it can be inferred that a greater percentage of the liquid volume will impact the surface due to higher droplet inertia, with

fewer being entrained by the atomizing air jet. This was observed for the elastic liquids, including KELTRACK, from the absence of a dark atomizing air jet.

This observation however was not experimentally investigated at this time. Given the current experimental setup, it was questioned whether or not valid conclusions could be obtained. Thus, this area of experimentally determining droplet entrainment effects on transfer efficiency losses is left as an area of future work. A combination of laser induced fluorescence (LIF) and particle image velocimetry (PIV) should be employed in order to analyze air flow patterns around the rail. By seeding the flow with a fluorescing particle dye, using light emitted from the PIV laser, and by employing both micro and macro imaging setups, insight into the flow field around the rail could be obtained and relevant insight into this field could be gained. Although reported for impinging fuel sprays using pressure injection, experimental work into wall-jets was done by Mohammadi *et al.* [2000].

Knowledge of the height and spreading velocity of the wall jet could also be applied to the analysis of boundary layer effects, described in the next section.

4.3.3 Overspray

For the given spray deposition process, it is essential that the spray be confined to the width of the rail as closely as possible. As a means of examining this, amongst other variables, a number of videos were taken of the spray deposition process on the surface of the rail for all test liquids, using the overhead imaging setup. This provided a qualitative insight into the spray deposition process and highlighted significant differences in spray-surface interaction amongst the various test liquids. Unfortunately, however, the true insight that these videos provide cannot be seen through observing images extracted from the videos. However, shown in Figure 4.16 below are two overhead images of the spray deposition process for KELTRACK.

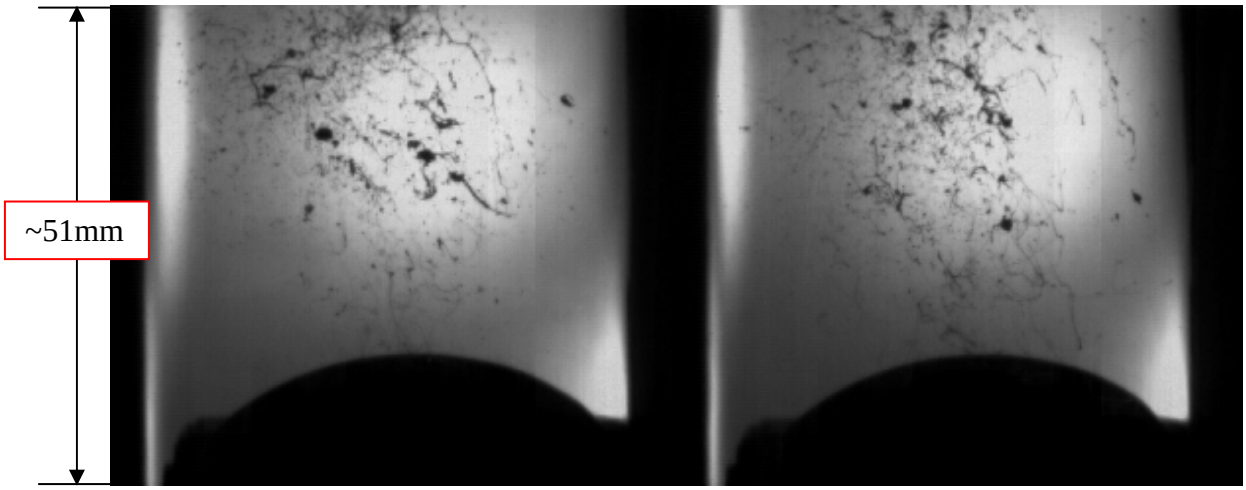

Figure 4.16: KELTRACK being applied to surface of rail

Although not able to be discerned in the above images, examination of the videos illustrated that the spray deposition of KELTRACK proved to be very well confined to the width of the rail. This however was not the case for all test liquids; particularly for water and the 50 wt.% glycerin, there seemed to be significant overspray. This was highlighted by noticeable spray pulsations, mentioned further in section 4.6. 1000K PEO on the other hand, had a spray deposition process very similar to that of KELTRACK and was confined even more-so to the centre of the rail, a consequence of 1000K PEO's inability to effectively atomize.

Videos near the outermost edges of the gauge face of the rail were also taken. Although there were obvious signs of liquid material impacting at the outermost reaches of the rail width, significant losses were not noticed.

Additional experimental means may be employed to measure the amount of overspray associated with the spray deposition of KELTRACK however the author does not feel this is necessary. The volumetric fraction thought to be expelled out of the rail width confines is considered to be negligibly small.

As a more quantitative means of examining the spray deposition, a spray label analysis was performed, now discussed in section 4.4.

4.4 Spray Label Analysis

4.4.1 Methodology

As an additional means of examining the spray deposition on the surface of the rail, a spray label analysis was performed. The purpose of this analysis was to examine the effect of atomizing pressure (AP) and rail surface speed (RSS) on spray deposition. As a result, the following test matrix was used:

Table 4.2: Spray label test matrix

Test 1		Test 2	
AP (psig)	**RSS (m/s)**	**RSS (m/s)**	**AP (psig)**
20	10	10	12
	20		20
	25		28

This analysis consisted of precisely positioning and fastening aluminum-backed tape to the centre of the rail surface (covering the entire top of rail surface, with the edges of the tape aligned at the edges of the gauge face), actuating the linear traverse as usual, and spraying KELTRACK on the aluminum surface of the tape. Aluminum-backed tape was used in order to ensure that no absorption of the liquid friction modifier occurred. The use of this tape however added a level of difficulty to the analysis in that the tape contained surface texture lines that were quite noticeable upon performing image processing. Once KELTRACK, however, had been applied to the aluminum-backed tape, the label was removed and scanned at a resolution of 600 dots per inch.

A short program was written in MATLAB® (code is given in Appendix E) using the built-in Image Processing Toolbox and was designed to determine:

1) The percentage area of rail surface covered for a given fixed label window, approximately 48mm x 28mm.

2) If widthwise asymmetries were present in the spray distribution.

The program worked as follows: the scanned label was read into MATLAB® and the area of interest where the image analysis was to take place was selected using a cropping feature. Using a zoom function, the furthest most left pixel of the label was then selected. Being that all labels had a fixed pixel width, the label was cropped to a defined width and height to ensure consistency of results. A threshold was then set to try to isolate KELTRACK's spray deposition from the surface texture lines apparent on the aluminum

tape (KELTRACK maintained a relatively constant intensity regardless of drop size) and the image was converted to black and white. Unfortunately however, after numerous attempts of trying to remove the surface texture lines from the label, one consistent method could not be applied and as a result, there still existed obvious signs of the surface texture lines in the image processed labels. An estimate as to the effect these lines had on the total percentage of area covered yielded a max value of 3.4%. Although not ideal, the presence of these lines was deemed to not significantly affect the results from this analysis. The total number of pixels of KELTRACK FM present within the set label window was then determined and knowing the total number of pixels in the image, a percentage spray area covered was determined. Finally, the label width was divided equally into four interrogation areas. The spray coverage area was then calculated for each of the defined interrogation windows and relative values were compared to highlight possible asymmetries in spray deposition.

4.4.2 Results

The following chart outlines the spray deposition results:

Table 4.3: Spray label analysis results

	AP = 20 psig			**Rail Speed = 10 m/s**			
	Rail Speed (m/s)			**Atomizing Pressure (psig)**			
	10	**20**	**25**	**12**	**20**	**28**	
Total % Area Covered	27.5	20.2	12.4	17.9	27.5	25.1	Total % Area Covered
Far Right	8.3	12.5	11.7	8.8	8.3	11.6	Far Right
Right	32.1	33.6	32.3	30.8	32.1	40.0	Right
Left	46.4	41.5	38.9	45.0	46.4	38.9	Left
Far Left	13.2	12.5	16.9	15.4	13.2	9.6	Far Left

The total % area covered refers to the % of area covered on the rail with FM for a given length and width of label. The other four columns refer to the four interrogation areas used in the investigation. The values stated in Table 4.3 are the calculated means based on ten samples.

Another point to note is that the reason 25 m/s was used instead of the logical 30 m/s in the effect of surface speed testing was due strictly to the linear traverse not being able to reach a speed of 30 m/s anymore. This was surprising but was something that had been

noticed over the last duration of testing. Even with a newly refined tail plug, speeds of 30m/s could not be obtained and thus, speeds of 25m/s were used.

Shown in Figure 4.17 below is a sample image of the spray deposition at a rail speed of 10 m/s, with an atomizing pressure of 20psig. The four interrogation areas given in Table 4.3, defined as if one was looking at the back of the rail profile as it was being fired, are shown here as well.

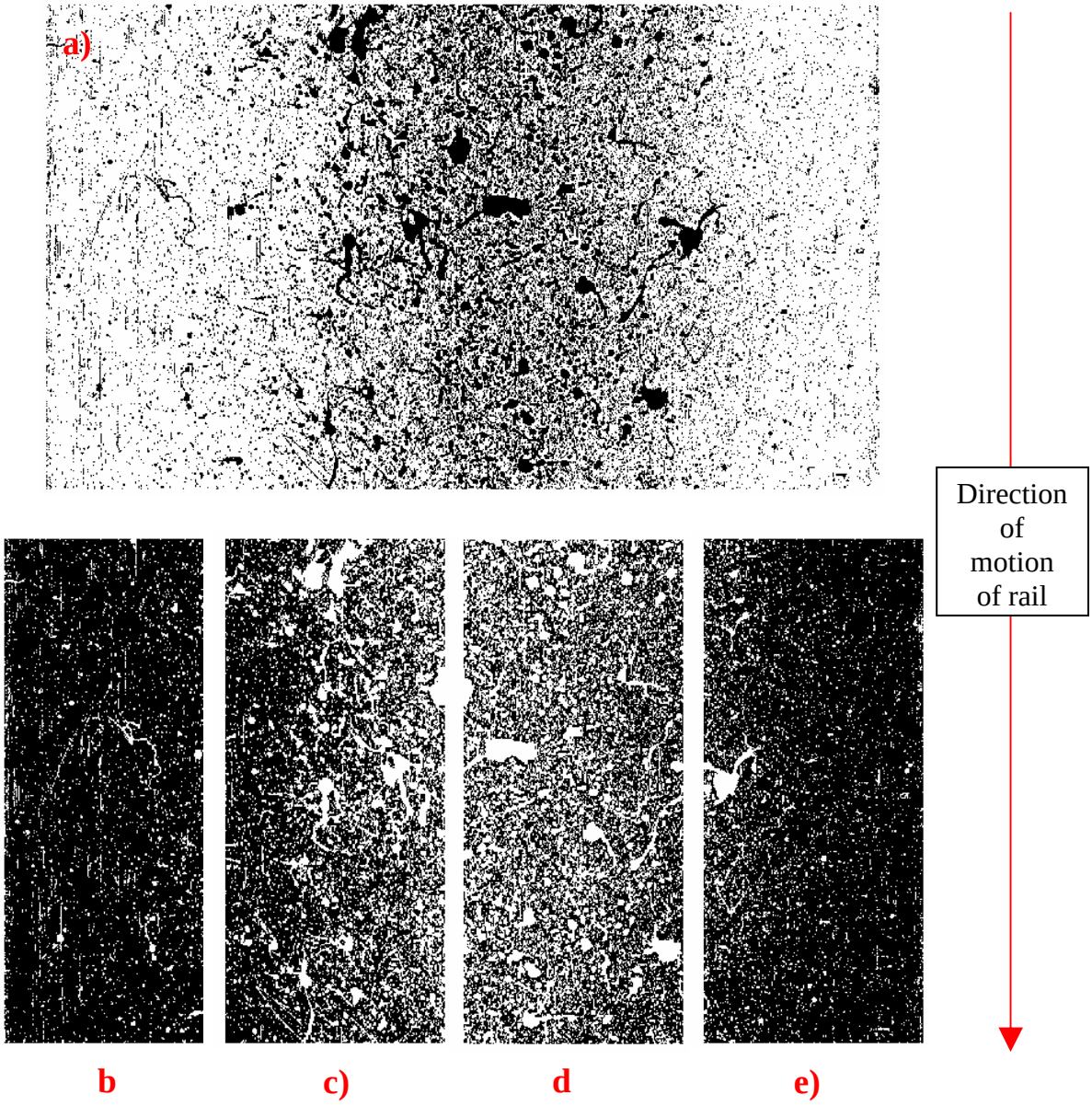

Figure 4.17: a) Sample image processed label b) far right c) right d) left e) far left

4.4.3 Discussion

Firstly, as can be seen from Table 4.3, the percentage area covered decreased as rail speed was increased, with a spray coverage of approximately 27.5% being reported for 10m/s. This is as expected due to the decreased time the rail will spend underneath the spray with higher velocities. The other thing to note is, as mentioned in section 4.5, the presence of the boundary layer may play a role at higher speeds, possibly preventing the impaction of a larger percentage of the lower inertia droplets, thus contributing to the reduction in spray coverage, which would not be experienced in field application.

Secondly, as atomizing pressure was increased from 12psig to 20psig, an increase in spray coverage area was noted. However, by further increasing the pressure to 28psig, the spray coverage slightly decreased. By increasing atomization pressure, atomization will be enhanced, expected to lead to a finer mean droplet size, thus, increasing the probability for a greater percentage area covered. However, there exists a limit to this relationship at some stage; as atomizing pressure is increased, the percentage area covered would no longer continue to increase. Whether that limit is observed here between 20 and 28psig is uncertain. This is left as an area for future work, with testing incorporating a wider range of pressures and in using a larger statistical sample set to base conclusions.

Thirdly, the spray deposition seemed to be skewed to the left of the centerline. This was noted in all cases examined. The nozzle had been completely cleaned immediately prior to the start of testing; therefore, nozzle fouling can be ruled out. One explanation for these asymmetries in spray deposition could be due to a possible asymmetric liquid flow due to slight asymmetries in the duckbill. Although in examining the plain liquid jet, it did not appear to be skewed in any way. A second explanation could be due to asymmetries in the atomizing air flow paths in the nozzle itself. It was noted that the annular holes situated in the small washer inside the atomizer with which the atomizing air passes through before it exits out through the annular air gap were not of consistent diameter. In the case of the varying surface speed, this effect seemed to be the strongest at the lower surface speed of 10m/s, with the effect decreasing with increasing surface speed. At a higher surface speed with less spray coverage, the decreased volume of liquid material in the fixed window may make the skewing effect seem less pronounced. For the second case, this effect seemed to be strongest at the lower atomizing pressures and significantly less pronounced at the higher atomizing pressure of 28psig, almost to the

point where the spray was symmetric about the centreline. Reasons for this are unknown at this time.

Finally, variations in total spray coverage measurements could be attributed to the spray pulsation phenomenon, previously described in section 4.6. These spray pulsations, as seen in the videos, are characterized by temporal and spatial fluctuations in droplet number density and as a result, are believed to affect spray deposition in the lengthwise direction. The measurement window in which analysis was performed may not have been large enough to encompass the periodic frequency of the pulsation and thus, depending on where the measurements were taken, could yield substantially different spray coverage areas. Standard deviations for the total spray coverage measurements ranged from 0.9 to 3.6 and from 1.5 to as high as 7.1 for the individual spray coverage measurements, thus resulting in futile confidence levels, based on the student-t distribution, for most measurements.

4.4.4 Recommendations

A much larger portion of the label (i.e. the full length) should be examined and analyzed in hopes of identifying and quantifying lengthwise variation in spray deposition. This would highlight the effect of the spray pulsation phenomenon, as mentioned in section 4.6, on spray deposition and a frequency at which these occur could be estimated.

A larger sample set should also be implemented as a means of providing a confidence level with which spray coverage can be accurately stated for the above testing conditions.

It was recently suggested by an expert in the field that a spray not be used for this coating application. Instead, he suggested that more research be conducted into using a plain liquid jet. The use of this analysis program, combined with the linear traverse, could be used to test the effectiveness of such a concept and is left as an area for future work.

4.5 Boundary Layer Analysis

Originally, spray impaction tests were to be conducted at 10, 20, and 30 m/s; however, it became immediately obvious at 20m/s that there was the strong presence of a boundary layer on the surface of the rail. This was evident by observing the horizontal movement of droplets and other debris traveling in the same direction and at approximately the same speed as the rail.

The height of this boundary layer on the surface of the rail was approximated using a flat plate flow analysis. Using the length of the rail surface (approximately 0.3m), Reynolds numbers (Re_x) at 10, 20, and 30 m/s were calculated to be 203200, 406400, and 609600. In all likelihood, the boundary layer is turbulent and thus, Blasius' solution for turbulent flow was used, which is given as:

$$\frac{\delta}{x} = \frac{0.16}{\mathrm{Re}_x^{1/7}}, \tag{4.5}$$

where δ is the boundary layer thickness (u = 0.99U) [White 1999]. This yields boundary layer heights of 8.51mm, 7.71mm, and 7.27mm at 10, 20, and 30m/s, respectively.

As mentioned in the previous section, when the atomizing air jet impinges on the surface of the rail, its streamlines are bent and a wall-jet is formed, which moves away from its impingement location. Being that for all testing, the camera was situated between the nozzle and the exit of the linear traverse, in the videos that were taken, the wall-jet tended to act against the boundary layer (if the camera was located downstream of the nozzle, the atomizing air jet and boundary layer would act together). In many cases, this effect could be seen as the rail first entered underneath the nozzle. Droplets, traveling in the direction of the rail in the boundary layer, suddenly changed course and immediately were driven back in the reverse direction. It was obvious that the strength of the atomizing air jet was significantly stronger than that of the boundary layer at 10 m/s. However, as the velocity increased to 20 m/s, significantly fewer droplets were seen impacting the rail and significantly more were seen traveling in the direction of the rail. This effect was significantly more pronounced at 30 m/s, to the point where droplet impact was very rarely observed in the given imaging field of view, and the presence of the boundary layer seemed to be much stronger than that of the atomizing air jet. It is unclear however as to the exact role the strength of the boundary layer plays on this observed reduction of the number of droplet impacts; it is surmised that there may be additional factors which need to be considered, such as skewing of the spray, which may be contributing to the observed lack of droplet impacts. In any case, all testing then became confined to a surface speed of 10 m/s, where minimal boundary layer interaction was noticed; the effect of surface speed on droplet deposition was therefore not quantified in this analysis.

4.6 Spray Pulsation Phenomenon

First noticed in videos taken of the atomization of KELTRACK, the breakup process seemed to be subject to pulsations, operating at a given frequency. These pulsations, resemblant of the super-pulsating sub-mode previously noted in literature [Farago and Chigier 1992], are defined as having both spatial and temporal fluctuations in droplet-number density [Li *et al.* 2005]. These pulsations were noticed not only in viewing the breakup immediately downstream of the nozzle, but also were observed in the examination of both the horizontal and overhead videos, with the pulsations being most easily discernable with the lower viscosity, inelastic liquids. Discussion of these pulsations will not be taken further but it is recommended as an area for future work that the effect of these pulsations on spray deposition and uniformity be quantified.

4.7 Effect of Nozzle Orientation

As a means of examining the effect of nozzle orientation on droplet impaction behavior, KELTRACK was sprayed at a nozzle orientation of both 45° towards the oncoming rail surface and 45° away from the oncoming rail surface. The former of these had the effect of increasing the relative velocity between the spray and the rail, where the latter had the opposite effect. This second orientation can be considered analogous to field application of LFM. It has been noted in preliminary work by Li [2006] that the effect of a crosswind on spray behavior is to skew the spray in the direction of the flow velocity. As a result, the spray no longer impinges the surface in a direction normal to the surface, but instead impinges at an inclined angle, which is a function of flow velocity. This skewing then acts to reduce the relative velocity between the moving spray nozzle and the stationary surface.

Rein [1993] points out that the splash threshold may be lowered when a droplet impacts the surface at oblique angles. This is due to a sudden tangential force experienced upon impact, causing a destabilizing effect on the lamella. This effect is also seen when a droplet impinges upon a moving surface, as mentioned in section 2.5. Thus, in reducing the effective relative velocity at which droplets impinge, the onset of splash can be reduced.

In examining the videos taken with the nozzle oriented away from the incoming rail, it was clearly obvious that the reduction in relative velocity led to a much more relaxed spray impaction, with no occurrences of splashing. However, in examining the opposing

case, where the spray-rail relative velocity was increased, spreading of impacting droplets and ligaments was significantly more energetic and although instances were few, droplet splash was observed. These qualitative observations thus agree with Rein [1993].

Although only a brief synopsis is given here, field application of LFM with an associated inherent cross flow may prove to be beneficial in promoting effective spray coverage.

4.8 Uncertainty Analysis

The error analysis in this investigation consisted of both the error associated with droplet velocity, impact angle, and droplet diameter measurements, as well as the error associated with the calculation of the dimensionless numbers, Weber number, Reynolds number, and Ohnesorge number. Being that the dimensionless numbers are functions of multiple variables, x_i, their uncertainties are dependent on the combined error present in the measured variables of interest (u_{x_i}), given as equation 4.6 [Figliola and Beasley 1995],

$$u_{x_i} = \pm\sqrt{e_1^{\,2} + e_2^{\,2} + \cdots + e_j^{\,2}} \tag{4.6}$$

where *e* is defined as an element of error of the measured variable and *j* is the number of measured variables. The uncertainties of these measured values however were not easily defined, as discussed below. The uncertainty associated with the dimensionless variables are thus dependent on these measured variables and are given as equation 4.7,

$$u_R = \pm\sqrt{\sum_i^L \left(\theta_i u_{x_i}\right)^2} \tag{4.7}$$

where R is the dependent variable of interest (in our case, it is the dimensionless numbers), u_R is the uncertainty of this dependent variable, *i* is the index representing *L* measured variables, and θ_i, defined as the sensitivity index of R with respect to x_i. This sensitivity index is given as:

$$\theta_i = \left.\frac{\partial R}{\partial x_i}\right|_{x=\bar{x}} \tag{4.8}.$$

where R is the dependent variable (in our case, it is the dimensionless number of interest).

For droplet normal velocity, Weber number, Reynolds number, and Ohnesorge number, equation 4.7 can be written as equations 4.9, 4.10, 4.11, and 4.12, respectively.

$$u_{u_{normal}} = \sqrt{(\sin\alpha \cdot u_U)^2 + (U\cos\alpha \cdot u_\alpha)^2} \tag{4.9}$$

$$u_{We} = \sqrt{\left(\frac{U_{normal}{}^2 d}{\sigma}\cdot u_\rho\right)^2 + \left(\frac{2U_{normal}\rho d}{\sigma}\cdot u_{U\,normal}\right)^2 + \left(\frac{\rho U_{normal}{}^2}{\sigma}\cdot u_d\right)^2 + \left(\frac{-\rho U_{normal}{}^2 d}{\sigma^2}\cdot u_\sigma\right)^2} \tag{4.10}$$

$$u_{\mathrm{Re}} = \sqrt{\left(\frac{U_{normal} d}{\mu}\cdot u_\rho\right)^2 + \left(\frac{\rho d}{\mu}\cdot u_{U_{normal}}\right)^2 + \left(\frac{\rho U_{normal}}{\mu}\cdot u_d\right)^2 + \left(\frac{-\rho U_{normal} d}{\mu^2}\cdot u_\mu\right)^2} \tag{4.11}$$

$$u_{Oh} = \sqrt{\left(\frac{1}{(\rho\sigma d)^{1/2}}\cdot u_\mu\right)^2 + \left(\frac{-\mu}{2\rho^{3/2}(\sigma d)^{1/2}}\cdot u_\rho\right)^2 + \left(\frac{-\mu}{2\sigma^{3/2}(\rho d)^{1/2}}\cdot u_\sigma\right)^2 + \left(\frac{-\mu}{2d^{3/2}(\rho\sigma)^{1/2}}\cdot u_d\right)^2} \tag{4.12}$$

The resulting estimated uncertainties associated with the measured values are summarized in Table 4.4.

Table 4.4: Estimated ± uncertainties of measured variables

Surface tension	0.1 mN/m
Density	0.001 g/cm^3
Viscosity	2%
Velocity	0.23 m/s
Diameter	20%
Impact Angle	1.6°

Being that the diameter of the droplet was determined using a MATLAB image processing program, the error associated with droplet diameter is an approximation. Firstly, due to the resolution of the imaging system, error in droplet size increased for very small droplets. Secondly, the above mentioned stated error of 20% was estimated based on additional upper and lower thresholds set in the droplet sizing program which were used to estimate the percentage of pixels falling between the set threshold and the upper threshold and again between the lower threshold and the threshold used. This uncertainty measurement is deemed to be quite conservative.

The stated error in velocity measurement was based on ± one pixel in each direction and being that velocity was normalized with a fixed time frame for a defined pixel resolution, this value remained constant. The stated error in the impact angle measurement was determined also to be ± a pixel in each direction. However, due to the fact that this value is not normalized with a fixed time but instead with distance, this value increased with decreasing distance (decreasing velocity). As a result, the standard deviation was calculated for a given number of impact angle measurements and based on the student-t distribution for a 95% confidence level, was found to be ± 1.6°.

The estimated uncertainties in U_{normal}, Weber number, Reynolds number, and Ohnesorge number based on equations 4.9, 4.10, 4.11, and 4.12, evaluated at the values contributing to the maximum Weber number observed were 0.74%, 20.2%, 20.1%, and 10.3%, respectively. These uncertainty values are quite large; however, the reason behind these high values is due solely to the large estimated uncertainty in droplet diameter. As mentioned before, it is believed that these large uncertainties are considered to be very conservative.

Chapter 5

Conclusions

KELTRACK's current rheological formulation proved to be very effective in ensuring sprayed liquid deposited and remained on the surface of the rail. This superior spray impaction behavior can be attributed to KELTRACK's rheological properties as follows:

1) KELTRACK's viscoelasticity acts to impair atomization, allowing for ligaments to remain intact at a further downstream distance from the nozzle, preventing entrainment of low inertia light weight droplets. In addition, viscoelastic effects prevented secondary droplets from easily expelling themselves away from the parent drop upon impact due to filamentary structures which remained intact to the parent drop. This led to prevention of transfer efficiency losses. Finally, viscoelastic effects act to increase the splash threshold. Due to the time-dependency nature of viscoelastic liquids, droplets impacting a surface take on solid-like deformation due to very high-deformation rates experienced within a very short timescale. This solid-like deformation contributes to the suppression of splash [Crooks and Boger 2000].

2) The degree of spreading of KELTRACK ligaments and droplets is greatly suppressed compared with other test liquids. This behaviour can be partially attributed to the very high viscosity of KELTRACK. This is due to the fact that the majority of its inertial energy is dissipated in overcoming viscous forces during droplet deformation. As a result, very little energy remains to be transferred to surface energy to create new surface area and as a result, droplet spreading is reduced. This however may be one area that can be improved upon to further improve the spray deposition of KELTRACK.

3) KELTRACK's lower surface tension provided a reduced tendency to break up and form discrete droplets. As a result, KELTRACK ligaments had, on average, larger filamentary structures attached to them, when compared with the other elastic liquids. This increased volume provided these filamentary structures with enough inertia to resist the entrainment tendency of the atomizing air jet and thus, settle on the surface of the rail.

4) Although not able to be investigated in this analysis, work by Rafai and Bonn [2005] found that spreading was suppressed with shear-thinning solutions when

compared to Newtonian solutions. Based on this work, the shear thinning behavior of KELTRACK may also be inferred to contribute to its reduced tendency to spread.

Chapter 6

Recommendations

The effect of rail temperature on the spray impaction behavior of KELTRACK was not carried out in this investigation. However, being that KELTRACK's application range spans from extremely cold winter conditions (-40°C) to very warm summer conditions (+40°C), knowledge of the effect of temperature on spray deposition would be considered very beneficial and thus, should be considered for future work.

Surface effects were unfortunately disregarded in this analysis; the effect of rail surface roughness on spray deposition was not accounted for, nor was the rail surface roughness profile measured. For future testing, rail surface roughness should be quantified and surface wettability measurements should be conducted.

It was suggested by an expert in the field to apply an electrostatic charge to the spray as it exits from the nozzle. This would have the effect of lowering liquid surface tension and enhancing droplet deposition on the wall, without the use of surfactants, which could adversely affect polymer structure. This is left as an area for further investigation.

Finally, further work should be conducted in the areas of droplet impact of both shear-thinning liquids and yield-stress liquids. Preliminary work into the effects of these rheological properties has proven beneficial to spray coating processes. As noted by Nigen [2005], upon high velocity droplet impact of a yield-stress liquid, the droplet spreads to a maximum radius and if the presence of a yield-stress is strong enough to outweigh capillary forces, droplet recoil is inhibited, promoting spray coverage.

References

Bai, C., and Gosman, A.D., [1995]: Development of Methodology for Spray Impingement Simulation, SAE paper, no. 950283.

Bai, C.X., Rusche, H., and Gosman, A.D., [2002]: Modeling of gasoline spray impingement, Atomization and Sprays, Vol. 12, pp. 1-27.

Bergeron, V., Bonn, D., Yves Martin, J., and Vovelle, L., [2000]: Controlling droplet deposition with polymer additives, Nature, Vol. 405, pp. 772-775.

Boger, D.V., [1977]: A Highly Elastic Constant-Viscosity Fluid, Journal of Non-Newtonian Fluid Mechanics, Vol. 3(1), pp. 87-91.

Brunello, G., Callera, S., Coghe, A., Cossali, G.E., and Gamma, F., [1991]: LDV and PDA analysis of spray-wall interaction, International Congress on Liquid Atomization and Spray Systems, Gaithersburg, MD, paper 71, pp. 645-652.

Brunton, J.H., and Camus, J.J., [1970]: The flow of a liquid drop during impact, in: A.A. Fyall and R.B. King eds., Proceedings of the 3rd International Conference on Rain Erosion and Associated Phenomena, (Meersburg, West Germany, RAE, Farnborough, UK), pp. 327-352.

Chandra, S., and Avedisian, C.T., [1991]: On the collision of a droplet with a solid surface, Proc. R. Soc. London Ser. A, Vol. 432, pp. 13-41.

Chiddick, K.S., and Eadie, D.T., [1999]: Wheel/Rail Friction Management Solutions, Proceedings of the 14th Int. Conference on Current Problems in Rail Vehicles, PRORAIL 1999, Prague, October 1999, pp. 167-173.

Cooper-White, J.J., Crooks, R., and Boger, D., [2002]: A drop impact study of worm-like viscoelastic surfactant solutions, Colloids and Surfaces A: Physicochemical and Engineering Aspects, Vol. 210, pp. 105-123.

Cossali, G.E., Coghe, A., and Marengo, M., [1997]: The impact of a single drop on a wetted solid surface, Experiments in Fluids, Vol. 22(6), pp. 463-472.

Cotter, J., Eadie, D.T., Elvidge, D., Hooper, N., Roberts, J., Makowsky, T., and Liu, Y., [2005]: Top of Rail Friction Control: Reductions in Fuel and Greenhouse Gas Emissions, Proceedings of the International Heavy Haul Conference, Rio de Janeiro, Brazil, June 2005, pp. 327-334.

Crooks, R., and Boger, D., [2000]: Influence of fluid elasticity on drops impacting on dry surfaces, Journal of Rheology, Vol. 44(4), pp. 973-996.

Crooks, R., Cooper-White, J., and Boger, D., [2001]: The role of dynamic surface tension and elasticity on the dynamics of drop impact, Chemical Engineering Science, Vol. 56, pp. 5575-5592.

CSA Standard Z107.56-94 [1999]: Procedures for the Measurement of Occupational Noise Exposure, CSA International, pp. 1-24.

de Vicente, J., Stokes, J.R., and Spikes, H.A., [2006]: Soft lubrication of model hydrocolloids, Food Hydrocolloids, Vol. 20, pp. 483-491.

Dhiman, R., and Chandra, S., [2005]: Freezing-induced splashing during impact of molten metal droplets with high Weber numbers, International Journal of Heat and Mass Transfer, Vol. 48, pp. 5625-5638.

Eadie, D.T., and Kalousek, J., [2001]: Spray it on, let 'em roll, *Railway Age*, June 2001, pp. 48.

Eadie, D.T., Bovey, E., and Kalousek, J., [2002]: The Role of Friction Control in Effective Management of the Wheel/Rail Interface, Proceedings of The Railway Technology Conference at Railtex, Birmingham, UK, November 2002.

Eadie, D.T., Santoro, M., and Powell, W., [2003]: Local control of noise and vibration with KELTRACK™ friction modifier and Protector® trackside application: an integrated solution, Journal of Sound and Vibration, Vol. 267, Issue 3, pp. 761-772.

Faragó, Z., and Chigier, N., [1992]: Morphological Classification of Disintegration of Round Liquid Jets in a Coaxial Air Stream, Atomization and Sprays, Vol. 2, pp. 137-153.

Figliola, R.S., and Beasley, D.E., [1995]: Theory and Design for Mechanical Measurements, 2nd ed., New York: John Wiley & Sons.

Ford, R.E., and Furmidge, C.G.L., [1967]: Impact and spreading of spray drops on foliar surfaces, in Wetting (Soc. Chem. Industry, Monograph, No. 25), pp. 417-432.

Ghielmetti, C., [2001]: Experimental analysis of a spray impinging on a conical surface, International Journal of Thermal Science, Vol. 40, pp. 249-254.

Goldin, M., Yerushalmi, J., Pfeffer, R., and Shinnar, R., [1969]: Breakup of a laminar capillary jet of a viscoelastic fluid, Journal of Fluid Mechanics, Vol. 38, pp. 689-711, 1969.

Hinds, W.C., [1999]: Aerosol technology: properties, behavior, and measurement of airborne particles, 2nd ed., New York: John Wiley & Sons.

Kalousek, J., Hou, K., and Magel, E., [1997]: The Benefits of Friction Management – A Third-Body Approach, Wear, Vol. 211, pp 134-140.

Kim, H.Y., and Chun, J.H., [2001]: The recoiling of liquid droplets upon collision with solid surfaces, Physics of Fluids, Vol. 13, pp. 643-659.

Lee, H.J., and Kim, H.Y., [2004]: Control of drop rebound with solid target motion, Physics of Fluids, Vol. 16 (10), pp. 3715-3719.

Lefebvre, A.H., [1989]: *Atomization and Sprays*, Taylor and Francis Publishers, United States.

Lesser, M.B., and Field, J.E., [1983]: The impact of compressible liquids, Annual Review of Fluid Mechanics, Vol. 15, pp. 97-122.

Levin, Z., and Hobbs, P.V., [1971]: Splashing of water drops on solid and wetted surfaces: hydrodynamics and charge separation, Philos. Trans. R. Soc. London Ser. A, Vol. 269, pp. 555-585.

Li, L., Dressler, D. M., Green, S. I., and Davy, M. H., [2005]: An Experimental Study of Non-Newtonian Atomization, ILASS Americas 18th Annual Conference on Liquid Atomization and Spray Systems, Session 2A/1, Irvine, CA, May 2005.

Li, L.K.B., [2006]: An Experimental Study on Air-Blast Atomization of Viscoelastic Liquids, MASc. Thesis, University of British Columbia.

Lindgren, R., and Denbratt, I., [2000]: Modeling Gasoline Spray-wall Interaction - A Review of Current Models, SAE paper, no. 2000-01-2808.

Mansour, A., and Chigier, N., [1995]: Air-blast atomization of non-Newtonian liquids, Journal of Non-Newtonian Fluid Mechanics, Vol. 58, pp. 161-194.

Manzello, S.L., and Yang, J.C., [2004]: An experimental investigation of water droplet impingement on a heated wax surface, International Journal of Heat and Mass Transfer, Vol. 47, pp. 1701- 1709.

Mathews, W.S., Lee, C.F., and Peters, J.E., [2003]: Experimental investigations of spray/wall impingement, Atomization and Sprays, Vol. 13, pp. 223-242.

Mercer, T.T., [1973]: Aerosol Technology in Hazard Evaluation, Academic Press, New York.

Mish, S.P., and Hubbard, M., [2001]: Design of a Full Degree-of-Freedom Baseball Pitching Machine, Sports Engineering, Vol. 4, pp. 123-133.

Mohammadi, A., Miwa, K., Kidoguchi, Y., [2000]: High time-space resolution analysis of droplets behaviour and gas entrainment into diesel sprays impinging on a wall, Proceedings of ILASS-Europe 2000, Darmstadt (Germany), VII.5.1–5.6.

Mun, R.P., [1996]: The Breakup and Atomization of Dilute Polymer Solutions, Ph.D. Thesis, University of Melbourne.

Mun, R.P., Young, B.W., and Boger, D.V., [1999]: Atomization of dilute polymer solutions in agricultural spray nozzles, Journal of Non-Newtonian Fluid Mechanics, Vol. 83, pp. 163-178.

Mundo, C., Sommerfeld, M., and Tropea, C., [1995]: Droplet-wall collisions: experimental studies of the deformation and breakup process, International Journal of Multiphase Flows, Vol. 21, pp. 151-173.

Mundo, C., Sommerfeld, M., and Tropea, C., [1998]: On the modeling of liquid sprays impinging on surfaces, Atomization and Sprays, Vol. 8, pp. 625-652.

Mundo, C., Tropea, C., and Sommerfeld, M., [1997]: Numerical and experimental investigation of spray characteristics in the vicinity of a rigid wall, Experimental Thermal and Fluid Science, Vol. 15, pp. 228-237.

Naber, J.D., and Farrell, P.V., [1993]: Hydrodynamics of droplet impingement on a heated surface, SAE paper, no. 930919.

Naber, J.D., and Reitz, R.D., [1988]: Modeling engine spray/wall impingement, SAE paper, no. 880107.

Nigen, S., [2005]: Experimental Investigation of the Impact of an (apparent) Yield-Stress Material, Atomization and Sprays, Vol. 15, pp. 103-117.

Noveon, Inc.: Carbopol® 940 NF Polymer: Technical Literature, Bulletin 14: Formulating Topical Properties, Date accessed: July 24, 2006, pp. 1-16, http://www.pharma.noveon.com/products/carbopol_940_nf.asp.

Panao, M.R.O., and Moreira, A.L.N., [2004]: Experimental study of the flow regimes resulting from the impact of an intermittent gasoline spray, Experiments in Fluids, Vol. 37, pp. 834-855.

Parker, G.J., [1970]: in A.A. Fyall and R.B. King eds., Proceedings of the 3rd International Conference on Rain Erosion and Associated Phenomena, (Meersburg, West Germany, RAE, Farnborough, UK), pp. 349-352 (written contribution to discussion of paper by Brunton and Camus [1970]).

Pasandideh-Fard, M., Qiao, Y.M., Chandra, S., and Mostaghimi, J., [1996]: Capillary Effects during droplet impact on a solid surface, Physics of Fluids, Vol. 8, pp. 650-659.

Povarov, O.A., and Nazarov, O.I., [1976a]: Interaction of drops with boundary layer on rotating surfaces, Journal of Engineering Physics, Vol. 31, pp. 1453-1456.

Povarov, O.A., Shalnev, K.K., Nazarov, O.I., and Shalobasov, I.A. [1976b]: Collision of droplets with a moving plane surface, Sov. Phys. Dokl., Vol. 20(11), pp. 782-783.

Rafai, S., and Bonn, D., [2005]: Spreading of non-Newtonian fluids and surfactant solutions on solid surfaces, Physica A, Vol. 358, pp. 58-67.

Range K., and Feuillebois, F., [1998]: Influence of surface roughness on liquid drop impact, Journal of Colloid and Interface Science, Vol. 203(1), pp. 16-30.

Rein, M., [1993]: Phenomena of liquid drop impact on solid and liquid surfaces, Fluid Dynamics Research, Vol. 12, pp. 61-93.

Rioboo, R., Marengo, M., and Tropea, C., [2002]: Time evolution of liquid drop impact onto solid, dry surfaces, Experiments in Fluids, Vol. 33, pp. 112-124.

Rioboo, R., Tropea, C., and Marengo, M., [2001]: Outcomes from a drop impact on solid surfaces, Atomization and Sprays, Vol. 11, pp. 155-165.

Roisman, I.V., and Tropea, C., [2002]: Impact of a drop onto a wetted wall: description of crown formation and propagation, Journal of Fluid Mechanics, Vol. 472, pp. 373-397.

Roisman, I.V., and Tropea, C., [2005]: Fluctuating flow in a liquid layer and secondary spray created by an impacting spray, International Journal of Multiphase Flow, Vol. 31, pp. 179-200.

Roisman, I.V., Prunet-Foch, B., Tropea, C., and Vignes-Adler, M., [2002]: Multiple drop impact onto a dry solid substrate, Journal of Colloid and Interface Science, Vol. 256, pp. 396-410.

Rozhkov, A., Prunet-Foch, B., Vignes-Adler, M., [2003]: Impact of drops of polymer solutions on small targets, Physics of Fluids, Vol. 15(7), pp. 2006-2019.

Scheller, B.L., and Bousfield, D.W., [1995]: Newtonian drop impact with a solid surface, AIChE J., Vol. 41, pp. 1357-1367.

Schiaffino, S., and Sonin, A.A., [1997]: Molten droplet deposition and solidification at low Weber numbers. Physics of Fluids, Vol. 9, pp. 3172-3187.

Senda, J., Kanda, T., Al-Roub, M., Farrell, P.V., Fukami, T., and Fujimoto, H., [1997]: Modeling spray impingement considering fuel film formation on the wall, SAE paper, no. 970047.

Settles, G., Miller, J., Hartranft, T., and Brandt, A., [1998]: Visualization and Collection of Overspray from Airless Spray Painting, Proceedings of the 8th International Symposium on Flow Visualization, Sorrento, Italy, Sept. 1-4, Paper No. 138.

Sikalo, S., Marengo, M., Tropea, C., Ganic, E.N., [2002]: Analysis of impact of droplets on horizontal surfaces, Experimental Thermal and Fluid Sciences, Vol. 25, pp. 503-510.

Sikalo, S., Tropea, C., Ganic, E.N., [2005a]: Dynamic wetting angle of a spreading droplet, Experimental Thermal and Fluid Science, Vol. 29, pp. 795-802.

Sikalo, S., Tropea, C., Ganic, E.N., [2005b]: Impact of Droplets onto inclined surfaces, Journal of Colloid and Interface Sciences, Vol. 286, pp. 661-669.

Sivakumar, D., and Tropea, C., [2002]: Splashing impact of a spray onto a liquid film, Physics of Fluids, Vol. 14(12), pp. L85-L88.

Stanton, D.W., and Rutland, C.J., [1996]: Modeling fuel film formation and wall interaction in diesel engines, SAE paper, no. 960628.

Stow, C.D., and Hadfield, M.G., [1981]: An experimental investigation of fluid flow resulting from the impact of a water drop with an unyielding dry surface, Proc. R. Soc. London Ser. A, Vol. 373, pp. 419-441.

Tirtaatmadja, V., and Sridhar, T., [1993]: A filament stretching device for measurement of extensional viscosity, Journal of Rheology, Vol. 37, pp. 1081-1102.

Transport Canada: *Canada's Transportation System*, Last updated: November 1, 2005, Date accessed: May 1, 2006, http://www.tc.gc.ca/pol/en/report/brochure/default.htm.

Tropea, C., and Roisman, I.V., [2000]: Modeling of spray impact on solid surfaces, Atomization and Sprays, Vol. 10, pp. 387-408.

Vander Wal, R.L., Berger, G.M., and Mozes, S.D., [2006]: Droplets splashing upon films of the same fluid of various depths, Experiments in Fluids, Vol. 40, pp. 33-52.

Walzel, P., [1980]: Zerteilgrenze beim Tropfenprall. Chem.-Ing.-Tech, Vol. 52, pp. 338.

Weiss, C., [2005]: The liquid deposition fraction of sprays impinging vertical walls and flowing films, International Journal of Multiphase Flow, Vol. 31, pp. 115-140.

White, F.M., [1999]: Fluid Mechanics, 4th Edition, McGraw Hill.

WorkSafeBC Publications Part 7: Noise, Vibration, Radiation, and Temperature, WorkSafeBC, OHS Regulation, Date accessed: December 18, 2005, http://www2.worksafebc.com/publications/OHSRegulation/Part7.asp.

Worthington, A.M. [1876]: On the forms assumed by drops of liquids falling vertically on a horizontal plate, Proceedings of the Royal Society of London, Vol. 25, pp. 261-271.

Worthington, A.M. [1877]: A second paper on the forms assumed by drops of liquids falling vertically on a horizontal plate, Proceedings of the Royal Society of London, Vol. 25, pp. 498-503.

Xing, L.L., Glass, J.E., and Fernando, R.H., [1997]: Spray Application of Waterborne Coatings, Technology for Waterborne Coatings ACS Symposium Series, Vol. 663, pp. 265-295.

Yao, S.C., and Cai, K.Y., [1988]: The dynamics and Leidenfrost temperature of drops impacting on a hot surface at small angles, Experimental Thermal and Fluid Science, Vol. 1, pp. 363-371.

Yarin, A.L., **[2006]:** Drop Impact Dynamics: Splashing, Spreading, Receding, Bouncing…, Annual Review of Fluid Mechanics, Vol. 38, pp. 159-192.

Yarin, A.L., and Weiss, D.A., [1995]: Impact of Drops on solid surfaces: self-similar capillary waves, and splashing as a new type of kinematic discontinuity, Journal of Fluid Mechanics, Vol. 283, pp. 141-173.

Appendix A

Design of Linear Traverse

A.1 Design Options Considered

Numerous approaches were initially looked at when investigating the most plausible and effective design for the linear traverse. Table A.1 briefly outlines these additional approaches and gives reasons for not further pursuing these designs.

Table A.1: Linear traverse design summary

Option	Maximum Velocity	Cost	General Comments
Linear Actuator	10m/s (22.4mph)	$6500 US	Speeds inadequate
Linear Motors	+30m/s (60 – 70mph)	~$50k US	Small accelerations; Large travel; Supply current requirements N/A
Gravity Driven System	~9m/s (20mph) (4m ceiling)	Relatively Cheap	Velocities are height dependent; More vertical space required
Pneumatic System	+20m/s (~45mph)	$4-$6k US	Mechanical linkages combined with pneumatic cylinders; complex design
Angular Rotation Device	+30m/s (60-70mph)	Relatively Cheap	Inadequate ratio between F_{st} and F_{cp} after impact
Pursued Option			
Energy Storage System (pneumatic)	+30m/s (60-70mph)	$4,000	Most practical and easiest to construct

As shown in Table A.1, the pursued option led into the existing linear traverse design, which is to be discussed further in section A.3. Although the details of all these potential design options will not be discussed here, the next section will take a brief look at why one particular option, the angular rotation device, a seemingly simple and logical design, was not used.

A.2 Angular Rotation Device

Previous studies examining droplet impaction on a moving surface have used the relatively simple method of achieving a moving surface with which to impinge upon by using a rotating disk. Initially, this option seemed to be the most logical, least expensive, and easiest to construct and implement, particularly when compared to the other options

available. However, after further examination, this method proved to be somewhat problematic.

A simple analysis was performed as a basic approximation to the physics inherent with this design. Two areas were investigated to determine whether or not a circular rail actuation system would be justified: 1) the effect of the centripetal acceleration before/during the droplet impacted the surface, and 2) the effect of the centripetal acceleration after the droplet impacted the surface, assuming the droplet had adhered to the surface.

Firstly, during droplet impact on the moving surface, the linear deceleration of the droplet was compared against the centripetal acceleration of the droplet. In order to justify that the angular momentum of the spinning disk did not have a detrimental effect on the droplet impingement process, the linear deceleration must be significantly larger than the centripetal acceleration. Assuming an angular rotation of 30 rad/s and a disk radius of 1 meter, and using the following relation:

$$v = r\omega \tag{A.1}$$

a velocity of 30m/s is obtained, which essentially is the max speed that the linear traverse would be required to achieve. Noting the kinematic relation for centripetal acceleration:

$$a_c = v^2 / r \tag{A.2}$$

and substituting (A.1) into (A.2), we note a value of 900 m/s^2. Similarly, for the linear deceleration of the droplet, we have:

$$a_c = v^2 / d \tag{A.3}$$

where d is the droplet diameter and v is the impacting droplet velocity. Being that the linear deceleration is dependent on droplet diameter, the ratio of the two accelerations was plotted as a function of droplet diameter, shown below in Figure A.1. As shown in this figure, the ratio of linear acceleration to centripetal acceleration at all droplet diameters less than or equal to 1.0 mm, assumed to be the maximum extent of the drop size distribution (at this stage of the analysis, no real experimental insight had been gained regarding drop size distribution), is more than sufficient (ratio = 1000 at droplet diameter of 1.0 mm) to justify the use of an angular rotation mechanism for droplets during impact.

However, the second step of the analysis involved comparing the surface tension force to the centripetal force after the droplet had impacted and deposited on the surface.

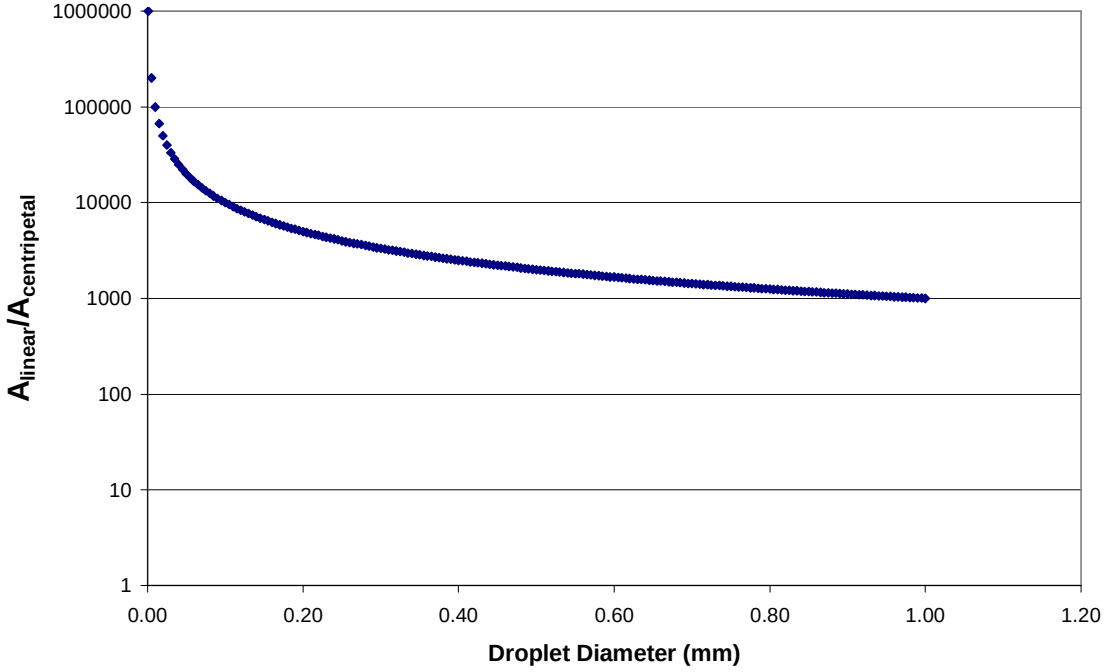

Figure A.1: Ratio of linear to centripetal acceleration as a function of droplet diameter

Assuming the surface tension force acts in a ring on the outer radius of the droplet, assuming water as the liquid impacting the disk, and neglecting the weight of the droplet, as well as contact angle considerations, we can define the force ratio as follows:

$$F_{centripetal} = m_{drop} r_c \omega^2 \tag{A.4}$$

$$F_{surfacetension} = \sigma 2\pi R_d \tag{A.5}$$

$$\frac{F_{st}}{F_c} = \frac{\sigma 2\pi R_d}{m_{drop} r_c \omega^2} = \frac{3\sigma}{2\rho {R_d}^2 r_c \omega^2}. \tag{A.6}$$

Shown in Figure A.2 below is a plot of the ratio of the surface tension force to the centripetal force, after the droplet has impacted the surface, as a function of droplet diameter. It can be seen from this figure that as droplet diameter increases, the ratio of F_{st}/F_c exponentially decreases. Assuming an acceptable ratio of two orders of magnitude ($F_{st}/F_c = 100$), this is only applicable to droplets smaller than approximately 50 microns. It was assumed at this time that the drop size distribution was of course going to extend beyond this value and so therefore, it was deemed that the centripetal acceleration would have too significant an effect on the impacted droplet and may cause it to expel radially

outwards from the surface after impact. Therefore, the angular rotation device was deemed inappropriate for our purposes.

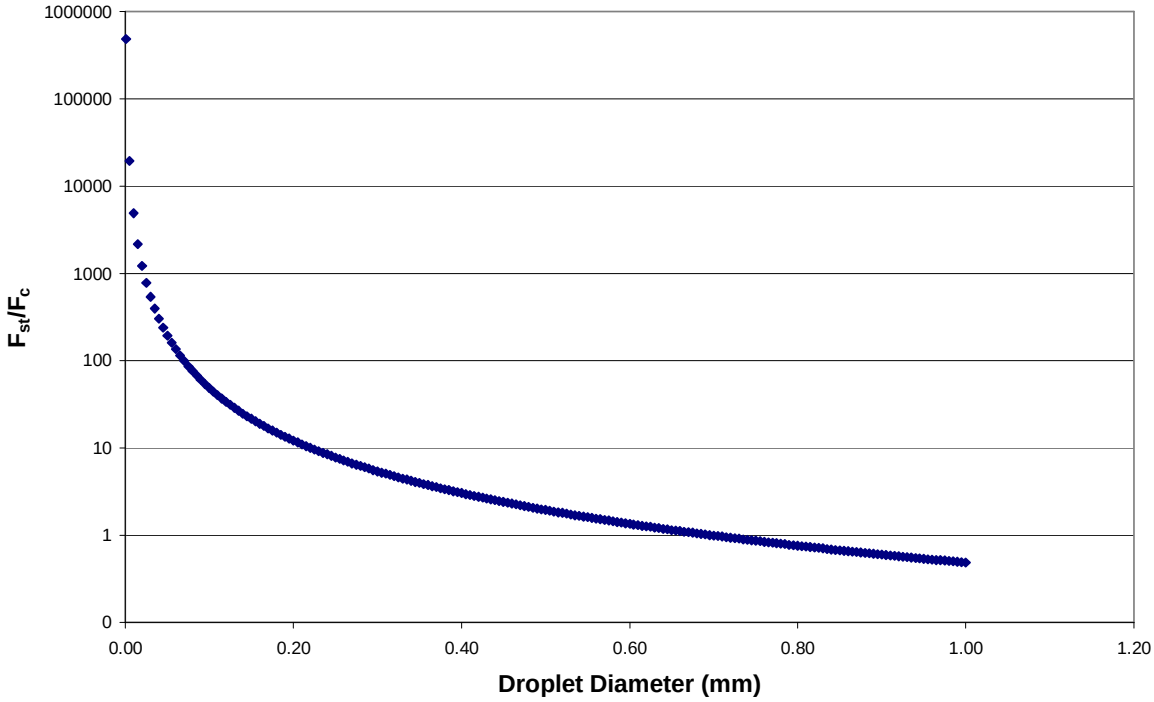

Figure A.2: Ratio of surface tension force to centripetal force as a function of droplet diameter

A.3 Theoretical Design of Linear Traverse

As a first step in the design of the pneumatic propulsion linear traverse, a theoretical thermodynamic model was used as a design tool to establish a relationship between initial tank pressure and final exit velocity. This model was also used to examine the effect of design variables such as air tank volume, air tank outlet diameter, and barrel length on the projectile surface's final velocity. The model was developed in MATLAB™ and the code was written by Mish and Hubbard [2001] at the Sports Biomechanics Laboratory in the Department of Mechanical and Aeronautical Engineering at UC Davis in California. Mish and Hubbard had used the thermodynamic model as a design tool for a similar propulsion system, but to propel a baseball.

The model used Newton's second law, the ideal gas law, conservation of mass and energy, and isentropic thermodynamic relations to establish a set of six differential equations [Mish and Hubbard 2001]. These equations were integrated in time using MATLAB, allowing for the determination of the remaining mass and energy in both the

air tank and the tube/barrel for a given amount of time after initial air release from the storage tank had occurred. For full details of how the model was developed, see Mish and Hubbard [2001].

Using the thermodynamic propulsion model, the theoretical performance of the linear traverse was estimated. Shown in Figures A.3 and A.4 below are two plots showing both the pressures in the air storage tank (P_a) and the barrel (P_b) as a function of time after initial air release, as well as the position and velocity of the projectile surface as a function of time after initial air release. Keep in mind that for the theoretical plots shown below, both friction and air drag have been neglected.

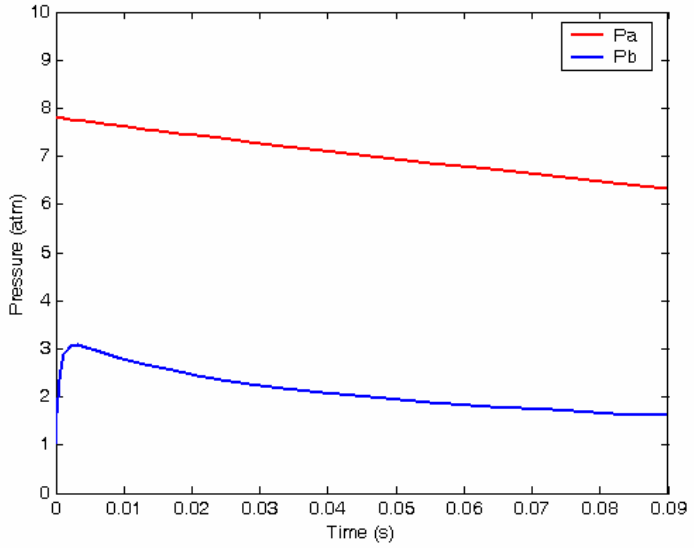

Figure A.3: Pressure in tanks A and B as a function of time

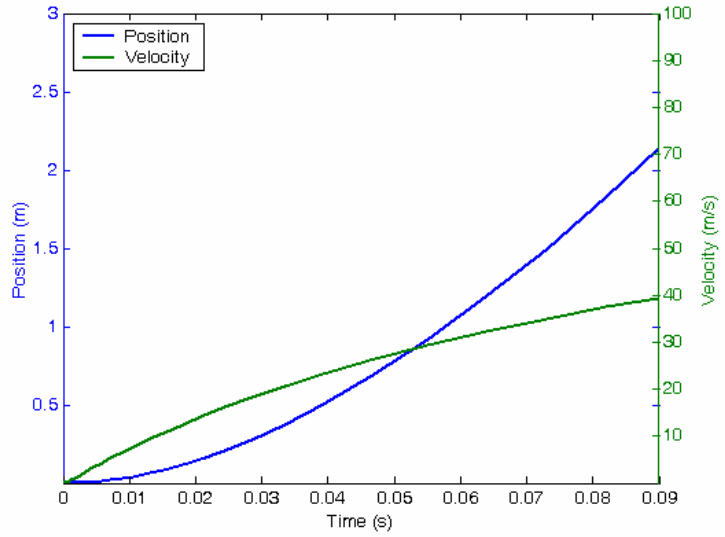

Figure A.4: Position and velocity as a function of time

For this analysis, an initial tank volume of 136L, an initial tank pressure of 7.9 bar (100psig), and a projectile surface mass of 2.5kg was used. In addition, the model became useful when determining the appropriate length for the linear traverse tube (i.e. barrel). Figure A.5 shown below displays the exit velocity as a function of initial tank pressure (gauge) for two barrel lengths.

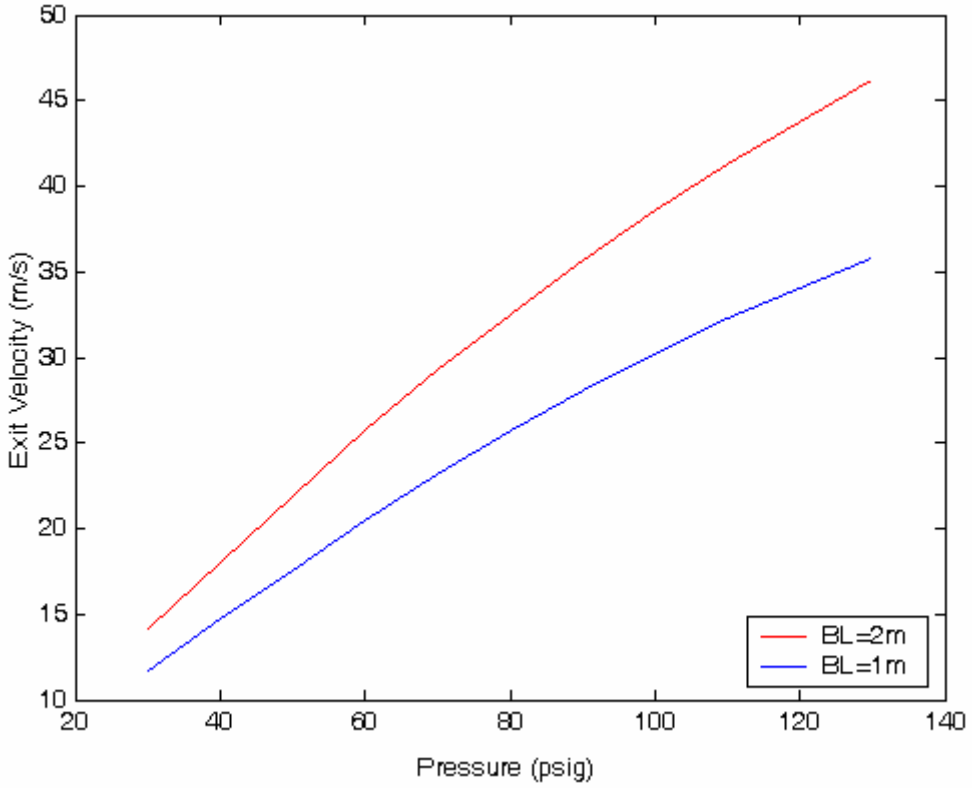

Figure A.5: Exit velocity as a function of initial tank pressure for barrel lengths of 1m and 2m

Based on the above plot and taking into consideration the absence of friction and aerodynamic drag in the above analysis, a barrel length of 2 meters was decided upon as the necessary length in order to be able to consistently provide velocities in the range of 30 m/s.

It was unknown however when the model was constructed how it would compare against experimental results. Once the linear traverse was operational, measurements of velocity at varying pressures were taken using the photodiode assembly and an oscilloscope. Shown below in Figure A.6 is a plot of theoretical and experimental projectile surface velocities as a function of initial tank pressure. As it can be seen the curves follow the same trend however the experimental curve begins to deviate from the

theoretical curve at higher pressures. This is thought to be due to a growing effect of frictional resistance on the bottom of the steel tube, as well as aerodynamic drag at higher velocities.

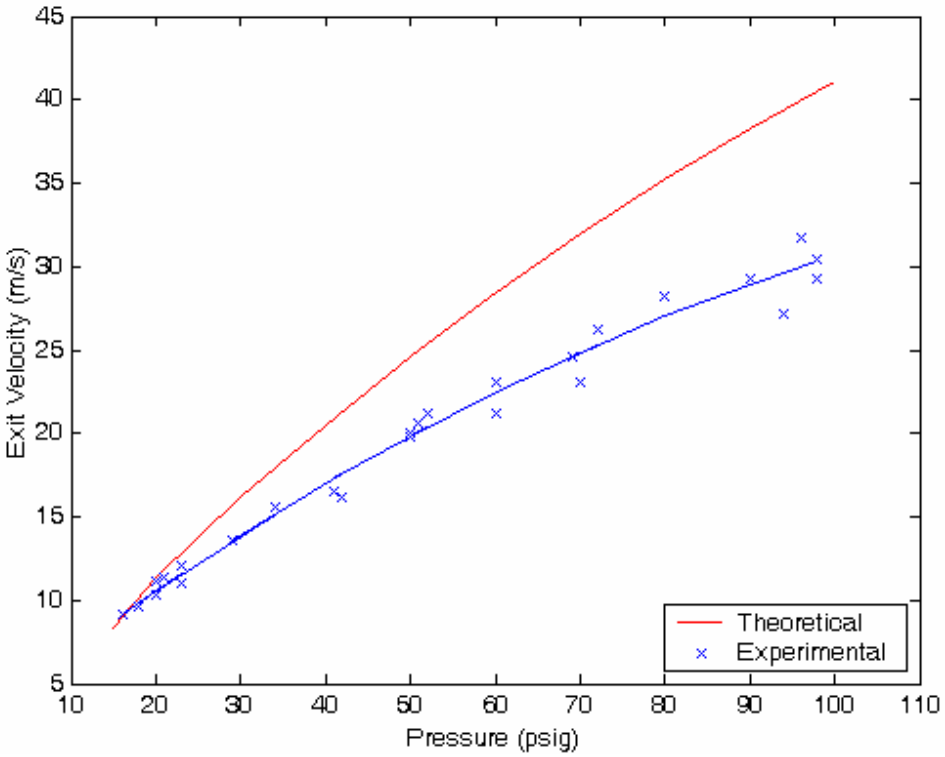

Figure A.6: Velocity as a function of pressure for a barrel length of 2m

A.4 Sound Pressure Level Analysis of Linear Traverse

A.4.1 Purpose:

Upon completion of the linear traverse, it was noticed that the expansion of the air in the tube, particularly upon exit out the tube, caused a relatively loud burst of noise to occur. This, of course, raised concerns that this excessive noise may be harmful to the occupants of Lab 308 in the PPC. Therefore, a sound pressure level analysis was carried out to ensure that the noise exposures in Lab 308 comply with the regulations put forth by the Worker's Compensation Board of British Columbia, with respect to the operation of the linear traverse.

The WCB states the following:

"An employer must ensure that a worker is not exposed to noise levels above either of the following exposure limits:

a) 85 dBA Lex daily noise exposure level;

b) 135 dBA peak sound level."

A.4.2 Equipment:

A Quest Technologies integrating sound level meter, Model 1900, was used for the following testing. The instrument 60dB measurement range was set to 70-130, with the response set to PEAK, providing a 50 microsecond time constant.

The sound level meter was calibrated before testing began using the Quest calibrator.

A.4.3 Test Procedure:

PEAK SPL measurements were taken at 5 locations, on a 1m radius from the centre of the air tank, spanning a total of 180°, at a height approximating ear-level. This is shown in Figure A.7.

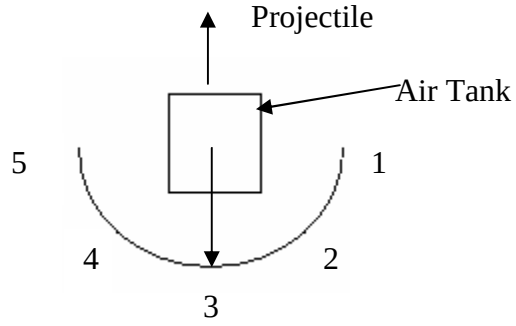

Figure A.7: Test locations

While the tank was filled, the peak SPL measurement was noted and recorded at each of the locations. This was also done while the traverse was fired.

A.4.4 Sound Enclosure:

In order to reduce the sound pressure level experienced by lab patrons, a sound absorption enclosure was built to encompass the air tank, hose, and valve. The enclosure was constructed out of ½" plywood and lined with Acoustimax® sound absorption foam. The enclosure dimensions are approximately 6' x 3' x 3'. SPL measurements taken with the enclosure on are shown below in Table A.2.

A.4.5 Data:

The SPL values measured at each location are shown below in Tables A.2 and A.3.

Table A.2: SPL measurements - no enclosure

Without Enclosure		
Location	Tank Filling (dBA)	Traverse Firing (dBA)
1	106.5	123.4
2	106.2	122.2
3	105.1	123.2
4	105.2	121.6
5	104.8	120.9

Table A.3: SPL measurements - with enclosure

With Enclosure		
Location	Tank Filling (dBA)	Traverse Firing (dBA)
1	90.0	122.6
2	86.0	121.3
3	88.8	120.9
4	86.0	121.7
5	84.3	121.9

From Tables A.1 and A.2, it can be seen that there are slightly higher SPL readings to the right of the traverse as opposed to behind or to the left of it. This may be due to the close proximity of objects to the left of the traverse.

Note: For simplicity in performing the above tests, no projectile was fired (just air release from the exit of the barrel). However, for comparison purposes, SPL tests were later conducted (results not shown) with the projectile being fired from the traverse. In doing this, it was found that there was no significant difference in SPL measurement between the two test conditions.

A.4.6 Analysis:

Recall that the peak sound level measured must be under 135 dBA to remain in compliance with WCB regulations. In examining Tables A.1 and A.2, we can see that we clearly are under a peak sound level of 135 dBA, with the maximum SPL measured to be 123.4 dBA, occurring when the traverse is fired.

In regards to the daily exposure level (dBA Lex is referred to as the level of a worker's total exposure to noise in dBA, averaged on an energy basis over the entire workday and adjusted to an equivalent 8 hour exposure), and based on *CSA Z107.56-94: Procedures for the Measurement of Occupational Noise Exposure*, the measured equivalent sound level was determined for the combined duration of the noise due to the filling tank and the firing of the traverse.

Without the enclosure, and using the loudest measurement of the five, assuming the loudest noise from the tank filling lasts for approximately 2s and the noise due to the firing of the traverse lasts for 3s, we obtain (3s at 123.4dBA is 60% of the total time of noise exposure):

$$L_{eq,t} = 10\log((1/100)\Sigma(P_i * 10^{L_{eq,i}/10}))$$
$$L_{eq,t} = 10\log((1/100)(60 * 10^{123.4/10} + 40 * 10^{106.5/10}))$$
$$L_{eq,t} = 121.2dBA$$

Then assuming the worst case scenario of the peak sound lasts for 5s and we fire every 5 minutes for 8hrs/day (leading us to a total peak continuous time of 8 minutes), the daily exposure level (Lex) can be calculated as follows:

$$L_{ex,8} = 10\log((T_w/8) * 10^{L_{eq,t}/10})$$
$$L_{ex,8} = 10\log((0.13/8) * 10^{121.2/10})$$

$$\boxed{L_{ex,8} = 103.3dBA}$$

Similarly, with the enclosure on these values are:

$$L_{eq,t} = 120.4dBA$$

$$\boxed{L_{ex,8} = 102.5dBA}$$

It can be seen that these values are well above the WCB regulations of 85 dBA Lex.

A.4.7 Conclusions:

Although the daily exposure noise level is higher than it should be, a few conclusions can be made:

1) It was obvious that the greatest sound produced was near the exit of the barrel. Thus, the addition of the enclosure did not provide significant overall sound reduction.

2) Ear plugs and ear muffs currently existing in the lab provide attenuations of approximately 36 and 25 dBA, respectively. In redoing the calculations shown

above after subtracting a 25 dBA attenuation due to earmuffs from the measured values, it was found that the daily exposure level was **77.6dBA**, below the exposure limit specified in the WCB regulations.

3) For the calculations, assumptions had to be made regarding the daily duty cycle of the traverse. This estimate is very conservative as it is extremely unlikely that testing will occur as frequently as every five minutes for eight consecutive hours.

4) One can also keep in mind the inverse square law, which states that for every doubling of distance, the SPL decreases by 6 dBA. (Note: This is generally only true in a reflection-free environment; in a room, the decrease is between 4 and 6 dBA close to a source and closer to 3 dBA several meters away.) Given that our SPL testing took place only 1m from the tank (4m from the traverse barrel exit) and the fact that the closest lab 308 patron from the linear traverse is approximately 3m away from where the measurements were taken, this will provide a slight reduction (between 4 and 6dBA) in SPL. In addition, it can be noted that the majority of other Lab 308 patrons are situated at a substantial distance from where the linear traverse sits and thus the SPL at these locations will be reduced further.

A.4.8 Recommendations:

It is recommended that Lab 308 attendants be notified when testing with the linear traverse is to commence. If they are within close proximity of the traverse, they should be equipped with hearing protection. In addition, in order to fulfill the requirement for a Noise Control and Hearing Conservation Program (already implemented noise measurement, engineered noise control, and hearing protection), signs notifying lab patrons of noise hazard areas shall be posted.

Appendix B

Experimental Testing Procedures

B.1 Preparing and Loading the Projectile Surface with Tail Plug

1. Ensure after each test, or before the initial test is ran, that the polished steel surface is wiped clean of any deposited sprayed material and/or additional contaminants, including fingerprints. Use either acetone or alcohol to wipe the surface clean with either paper towel or a clean cloth. Acetone and alcohol are located in the tin holding shelf, attached to the left side of the energy dissipation device.
2. Place the tail plug into the linear traverse tube, underneath the nozzle. Push it back into the enclosed section of the tube so that approximately half the tail plug is sticking out of the end of the tube.
3. Place the projectile surface into the linear traverse tube. Push it back against the tail plug and push both the tail plug and the projectile surface into the tube, just until the nose of the projectile surface enters the enclosed portion of the tub.
4. Place one end of the grey broom handle onto the very front of the nose of the projectile surface and push both the projectile surface and the tail plug to the back of the tube. NOTE: Pushing these two objects to the back of the tube is not an easy task and may require a lot of force, especially if the tail plug has been recently repaired.

B.2 Preparing the Energy Dissipation Device

The energy dissipation device consists of a number of cushions and sandbags however only one sandbag is actually used as the primary means of energy absorption. This sandbag is wrapped in Kevlar®, as well as canvas. The other sandbags and cushions are used primarily as a further means to stop the projectile surface if necessary and prevent it from bouncing around and getting damaged inside the plywood enclosure.

1. Pick up the canvas wrapped sandbag and reposition the sand to the centre of the bag, as if fluffing a pillow.
2. Replace the sandbag on the tube right near the entrance of the plywood enclosure. Be sure that the canvas is not bunched up around the sandbag but is instead wrapped uniformly around.

3. Ensure that the sandbag does not sit in the tube but instead, rests on it, allowing approximately a 2 inch gap between the bottom of the tube and the bottom of the sandbag. This is done to ensure that the bag is not punctured by the nose of the projectile surface when contact occurs.
4. If higher speeds are used (i.e. $\geq$ 20m/s), place a second sandbag behind this one on the back end of the linear traverse tube.

B.3 Computer Equipment and Imaging Setup

1. Turn on the computer located in the lab. Login password: *spray*.
2. Connect the camera to the power, ethernet, and trigger cables available with the camera. The other end of the power cable is plugged into the power outlet by the computer, the ethernet cable is connected directly to the computer allowing communication between the computer and the camera, and the trigger cable is connected directly to the first sensor in the photodiode assembly through use of a BNC cable and a male-to-male BNC connector.
3. Open the Phantom Ver605.2 software.
4. Go to “Acquisition”, “Setup and Recording”.
5. Set the desired sample rate, exposure time, resolution, and post trigger.
6. Precisely position both the camera and the lighting until the optimal lighting/imaging setup has been achieved. This is done by viewing the image capture area through use of the Phantom software.
    a. Adjust the settings on the lens (i.e. aperture and zoom) in order to obtain desired field of view and depth of field dimensions.
    b. Adjust the position of the PALLITE® as necessary in order to achieve optimal lighting.
7. When ready to trigger the camera using the photodiode assembly, press the “Capture” button. A message at the bottom of the window will appear “Preview + Recording… Waiting for Trigger”. The camera and software are now ready to capture images and will automatically be triggered through the 5V pulse sent to the camera when the photodiode assembly has sensed the passing by of the projectile.

B.4 Photodiode Assembly and Oscilloscope Readings

The photodiode assembly is a critical component in the effective operation of the linear traverse. It performs two functions:

1. Determines the velocity of the projectile surface. (By measuring the time separation between the triggering of the two laser diodes, a velocity can be determined, knowing the separation distance between the two lasers.)
2. Triggers the imaging system using a 5V TTL signal. (Attached to laser 1 is a voltage inverter and a BNC cable which hooks up directly to the trigger output cable for the high-speed camera. When this laser is triggered, a 5V signal is sent to the camera, thus triggering the camera and allowing for image capture.)

In order to use the photodiode system effectively:

1. Plug in the power supply for the photodiode assembly into the power bar located near the pump. Also ensure that the other end of the power supply is plugged into the back of the little black box located on the metal photodiode holder. The lasers should now be lasing.
2. Ensure that the laser beams line up directly with the associated sensor on the opposite side of the linear traverse tube.
3. Unplug the power supply for the photodiode assembly. Only plug it in when ready to fire as the lasers have a limited life and so it is best to not use them when not necessary.
4. Plug in the oscilloscope and turn it on.
5. Press the “Trigger Menu” button. Set-up the oscilloscope as follows:
6. Source: “Ch.1”.
7. Slope: “Dropping Edge”.
8. Trigger voltage: “1V”.
9. Set the reading to “DC”.
10. Position the horizontal output lines from Ch.1 and Ch.2 on top of each other using the vertical position dial.
11. Set the time separation to be 20ms.
12. Press the “Run/Stop” button, then followed by the “Single Sequence” button.
13. Initiate a test run by running a solid object (such as a piece of wood) in front of the sensors to see if the oscilloscope has sensed the breaking of the laser light.

14. The time separation can be measured by moving the vertical alignment bar to where the first breakage of light is sensed (drop of 5V in the signal), taking note of this time, and then moving this bar to where the second breakage of light has been sensed. This is your time separation.
15. If this test works successfully, then the oscilloscope is now set up to both determine velocities and trigger the camera. If not, recheck the orientation of the laser diodes, the intensity of the lasers, and/or the oscilloscope setup to ensure everything is setup correctly.

B.5 Liquid Preparation

1. Place the open end of the pump hose into the container of liquid desired to be pumped.
2. Plug-in the pump.
3. Make sure to connect the opposite end of the pump hose (with the valve on it) to the corresponding quick connect, located on the end of the liquid hose connecting to the nozzle.
4. Open this ball valve.
5. Place a beaker underneath the nozzle to catch the liquid.
6. Turn on the pump and turn the dial to approximately the 6th notch (this is based on previous tests where it was found that this setting yielded a flow rate of approximately 60ml/min, depending on liquid). Allow time for the nozzle to reach steady state flow (liquid flowing through the lines and out of the nozzle in a consistent manner with no sputters or air bubbles).
7. Measure the flow rate of the liquid being pumped.
    a. Place the 50ml beaker underneath the flowing liquid and at the exact same time, start the stopwatch.
    b. Time for 30s and estimate the volume of liquid in the beaker (i.e. for 60ml/min, we should have approximately 30ml of liquid in the beaker).
    c. Adjust the dial on the pump to either increase or decrease the flow as necessary to reach desired flow rate. Make sure to have put another beaker underneath the liquid stream to catch the depositing liquid.
    d. Repeat steps a, b, and c until desired flow rate is reached.

8. Turn off the pump and close the valve until testing is ready to commence. This is done in order to conserve liquid and avoid a more extensive cleanup. (NOTE: It may be necessary to check and readjust the flow rate each time the pump is shut off and restarted. This is dependent solely on the liquid being pumped (i.e. viscous liquids maintain flow rate more easily than when compared to less viscous liquids such as water). If after a couple tests are run with the pump being turned on and off and the flow rate is staying relatively constant, it is no longer necessary to test the flow rate before each test.)
9. Clean pump thoroughly after each test liquid or when completed testing for the day.

B.6 Filling the Linear Traverse Tank

1. Open the horizontally positioned red-handled valve located near the wall by the wind tunnel just above the power outlets. This will be referred to as the Primary Air Access Valve (PAAV). The air has now filled the air hoses leading up to the tank.
2. Set the regulator on the tank to the desired pressure, located at the end of the linear traverse, outside the plywood enclosure.
3. Open the ball-valve located next to the regulator. Air will now enter the tank until the desired pressure has been reached. Once this has occurred, close this valve.
4. The air tank is now filled and the linear traverse is considered to be “loaded” and potentially dangerous at this time.
5. The PAAV can remain open through the duration of the tests; however, for consistency purposes, please ensure this valve is closed when finished testing for the day.

NOTE: Always make sure to fill the air tank after the projectile surface has been loaded.

B.7 Using the Atomizing Air

1. Set the pressure regulator on the nozzle to the desired atomizing pressure.
2. Open the PAAV (see step 1 above).
3. Open the vertically positioned red-handled valve, known as the Atomizing Air Valve (AAV). The atomizing air should now be activated.
4. Close the AAV when spray testing has been completed.

B.8 Firing the Linear Traverse

1. The linear traverse is activated through a solenoid-actuated pilot valve. Plug-in the transformer for the pilot valve into the wall outlet by the wind tunnel. This is the two-pronged plug-in connected to the circular-shaped plastic trigger device for the linear traverse, usually located on top of the plywood sound-proofing enclosure.
2. When all of the previous steps have been completed (i.e. air tank is filled, projectile surface and tail plug are loaded, liquid is being pumped into traverse tube at set flow rate, photodiode assembly is initialized, imaging and computer equipment are properly prepared, energy dissipation device is properly positioned, atomizing air is activated), switch the trigger knob from "OFF" to "KABOOM", thus firing the linear traverse. Ensure that nothing is in the path of the rapidly moving projectile surface, other than the energy dissipation device.
3. Immediately after firing, re-close the pilot valve by switching the trigger back to the "OFF" position. This must be done in order to ensure that the air is maintained in the tank and not allowed to release while the tank is being filled in preparation for the next test.
4. Unplug the trigger when not in use or when finished testing at the end of the day.

B.9 Linear Traverse Testing Brief Summary

1. Load the clean projectile surface, with tail plug, into linear traverse tube.
2. Reposition sandbag in energy dissipation device.
3. Ensure computer is on, Phantom software is activated, camera settings are correct, image area is as desired, lighting is sufficient.
4. Turn on atomizing air, check atomizing pressure, and turn off air.
5. Turn pump on with beaker underneath, ensure desired flow rate, turn pump off, and remove beaker. (NOTE: If the flow rate changes with the turning on/off of the pump, just leave the pump running with beaker underneath until time of fire. Just remember to remove the beaker before firing!)
6. Fill linear traverse tank to desired pressure.
7. Plug-in photodiode assembly.
8. Press "Capture" button on computer. Run hand through lasers to make sure camera is properly triggered. Press "Capture" button again to reinitialize.

9. Turn on PALLITE®.
10. Turn on liquid pump. (Remove beaker if necessary.)
11. Turn on atomizing air and spray for 3-4 seconds.
12. Fire linear traverse, immediately closing valve after firing.
13. Turn off atomizing air.
14. Shut off pump.
15. Turn off PALLITE®.
16. Unplug photodiode assembly.
17. Save video using Phantom software.
18. Clean up sprayed liquid inside linear traverse tube.

B.10 Care and Maintenance

It is essential that all components of the linear traverse remain in top operating condition to ensure repeatability, as well as efficient and effective operation.

B.10.1 Projectile Surface

1. Ensure that there is no major damage to the aerodynamic nose or any other parts of the wooden carrier base. If so, fill the holes/dents with wood putty.
2. Ensure at all times the rail surface is securely screwed on to the wooden carrier base. There are two attachment points, one on either end of the rail. The attachment point at the front of the rail is not visible as the screw is covered up with wood putty. If you need to remove this screw for any reason, remove the wood putty by digging it out (using a pick or a chisel with a hammer). Make sure to replace the screw when finished, recovering the hole with new wood putty.
3. If the rail surface has to be removed from the wooden carrier base, ensure that it is once again level when secured.
4. Ensure that the pieces of PEEK®, located both on the sides and bottom of the rail surface, remain firmly attached to the wooden carrier base at all times. Currently, these pieces of PEEK® are attached to the carrier base through use of screws, as well as double-sided tape.

B.10.2 Tail Plug

1. Ensure that the tail plug fits as snugly as possible inside the linear traverse tube, without making loading the linear traverse an impossible task. The resistance felt when loading the linear traverse should be strong, requiring significant force to push the objects in the tube, however not unmanageable.
2. To ensure that the tail plug remains snug inside the tube, some basic maintenance and repair is required on the tail plug after a certain number of tests.
    a. If the existing tape coating tends to get tattered and starts falling off, rewrap the tail plug in packing tape, ensuring a uniform coating of tape around the surface of the tail plug. A sufficient coating of tape will be noticed when you place the tail plug in the open part of the tube and it slides in snugly along the sides.
    b. At the back of the tail plug there exists a wiper, designed to rub along the upper and corner surfaces of the inner traverse tube, so as to minimize air leakage from around the tail plug. When this wiper becomes worn, tattered, or diminished, it is essential that a new wiper be constructed out of the gasket material existing in the lab. This wiper is attached to the back of the polystyrene plug through use of approximately six to ten screws. Remove these screws, remove the old wiper, reposition new wiper, and reinsert screws into polystyrene base, thus securing the wiper to the plug.
    c. Finally, if the front end of the tail plug gets damaged (i.e. pushed in or dented in any way), this may cause the projectile surface to not sit flat when being pushed down the linear traverse tube, thus causing adverse effects when trying to visualize spray impingement. If this happens, it may be necessary to cut the damaged portion off of the plug and resurface the front of the tail plug. NOTE: The existing tail plug has a length of approximately 11 inches and its length is designed specifically to ensure that the projectile surface has opportunity to travel beneath and beyond the spray before the rapidly expanding air from inside the barrel was allowed to exit and disrupt the trajectories of airborne droplets. Therefore, if the tail plug is cut back, it may be necessary to construct an entire new tail plug to ensure it has the necessary length required for the projectile

surface to completely travel beneath the spray nozzle without worry of expanding air adversely affecting spray trajectories.

B.10.3 Photodiode Assembly

1. Ensure at all times that the laser beams line up directly with the associated sensor on the opposite side of the linear traverse tube. If they are off slightly, reposition them by just moving the laser diode inside its mounting hole until they are correctly lined up.
2. If one diode starts to dim, meaning that it is burning out, it must be replaced otherwise the sensor will not be able to read such a low intensity of light. (NOTE: The second laser diode is notoriously known for burning out on a regular basis; this will be obvious by the lack of an intense laser beam. Be prepared!) When this occurs:
    a. Purchase a new laser from the dollar store on campus in the village.
    b. Cut back the aluminum shell until the actual diode is exposed.
    c. Remove the old laser diode from its holder.
    d. Examine this laser diode as to how it is connected before removing the wires from it.
    e. Solder the POSITIVE output wire from the photodiode assembly to the bottom of the diode to one of the front terminals. At the same time, reconnect the NEGATIVE terminal to the outer aluminum shell.
    f. Reposition the new laser diode back into the holder and realign laser beam with associated sensor.

B.10.4 PALLITE® VIII

1. Make sure to take extreme caution when working with the PALLITE®. This light gets extremely hot very quickly.
2. Be very careful not to touch the bulbs in any way, nor bump the lamp while it is on. Either one of these may cause bulbs to burn out.
3. PALLITE® bulbs will eventually burn out and they will need to be replaced. Currently, bulbs have been purchased through The Optikon Corporation (www.optikon.ca), located in Kitchener, Ontario.

B.10.5 Liquid Pump

Make sure the pump is cleaned thoroughly after consecutive set of tests by cycling a significant amount of water through the pump. This is especially critical when pumping KELTRACK® as if left for longer periods of time (i.e. 24 hours), the KELTRACK® will harden and cause a plugging of the pump lines.

B.10.6 Linear Traverse Tube

After a sufficient number of tests, particularly with KELTRACK®, the bottom surface of the tube beneath the nozzle tends to become coated with a thin coating of sprayed material. Remove this coating as per necessitated with alcohol or acetone as this coating causes deceleration of the rail before it is required and also may cause the back end of the rail to lift up, therefore making consistent imaging rather difficult.

B.10.7 Nozzle

Over time and after significant testing, the nozzle may need to be cleaned to ensure no blockage of either the liquid or air streams is occurring. This is essential in ensuring effective nozzle operation.

B.10.8 Energy Dissipation Device

If the canvas wrapped sandbag is ever slightly positioned inaccurately on the traverse tube, puncture of the bag may occur, causing sand to spill out in the traverse tube and elsewhere. Remove the sand from the tube and repair the puncture in the bag by applying duct tape to the tear.

Appendix C

Test Liquid Ink Addition Justification

As mentioned in Chapter 3, as a means of increasing the image contrast of the finely atomized liquid features, red food dye was added to both the elastic and inelastic test liquids. Measurements of the shear viscosities of a water sample, an 80 wt.% glycerin sample, and a 300K PEO sample, before and after addition of the food dye, were conducted to ensure that the properties of the liquid were not significantly affected by the addition of the food dye. It was assumed that if the liquid properties of these three representative samples were not significantly affected, the same would apply for the 50 wt.% glycerin, the 100K PEO, and the 1000K PEO solutions and thus, only three samples were used for testing. The graphs obtained from the shear viscosity measurements are shown below as Figures C.1, C.2, and C.3 for water, 80 wt.% glycerin, and 300K PEO, respectively.

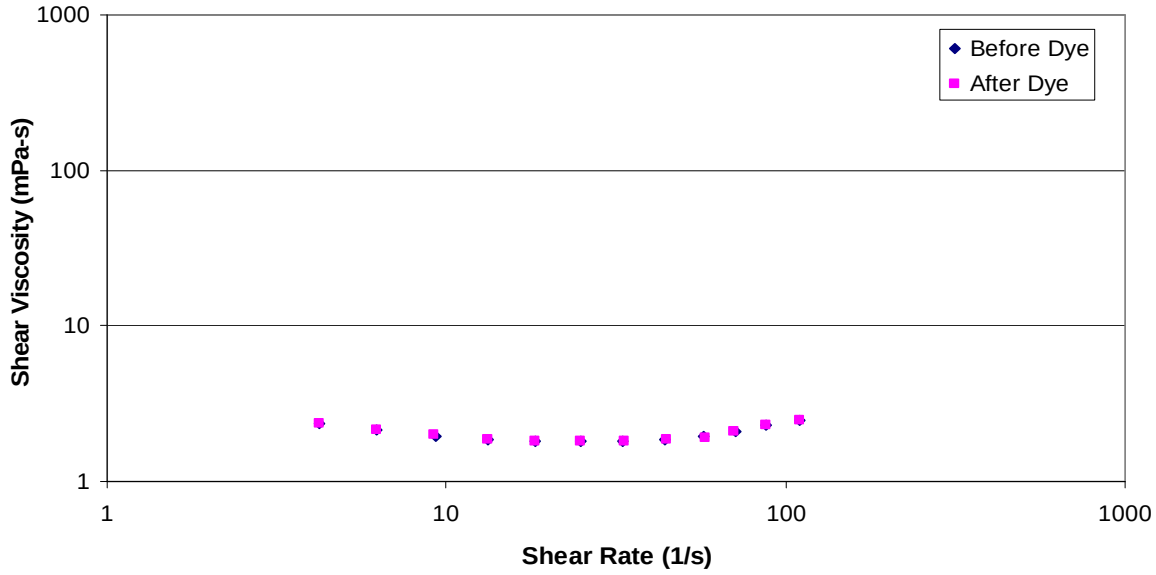

Figure C.1: Viscosity as a function of shear rate for water at 20°C

It can be seen from Figure C.1, that although the viscosity values obtained for water are slightly higher than the internationally accepted value (differences can be attributed to the measurement of such a low viscosity liquid), both curves pertaining to water with and without ink lie on top of each other.

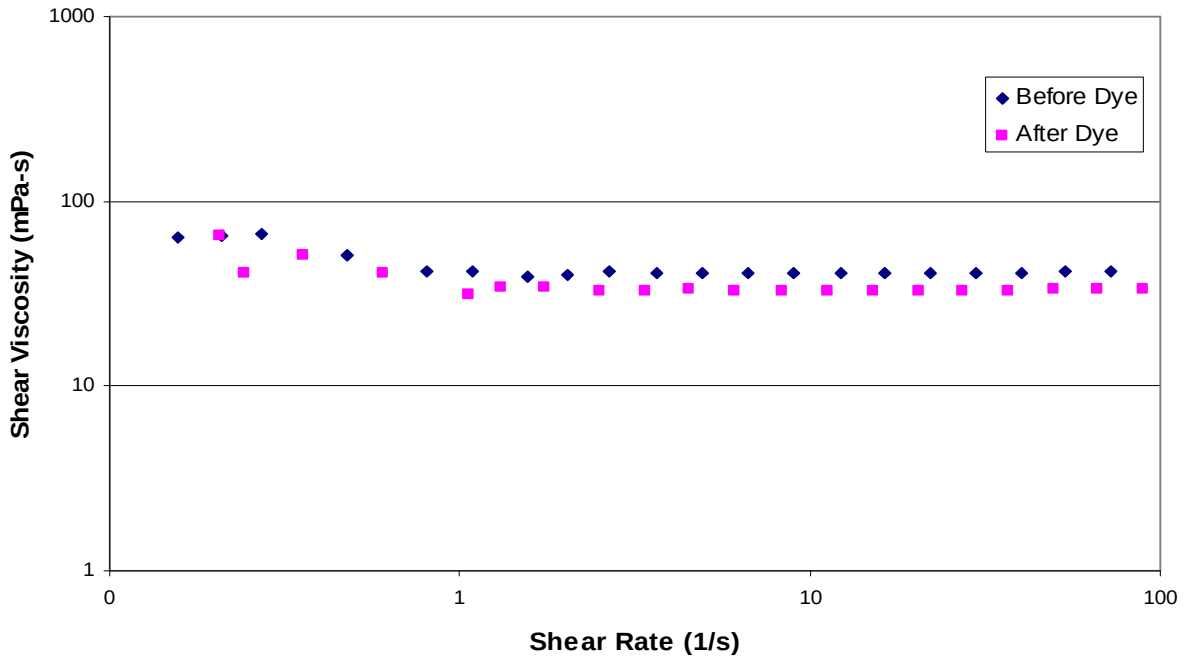

Figure C.2: Viscosity as a function of shear rate for 80 wt.% glycerin at 20°C

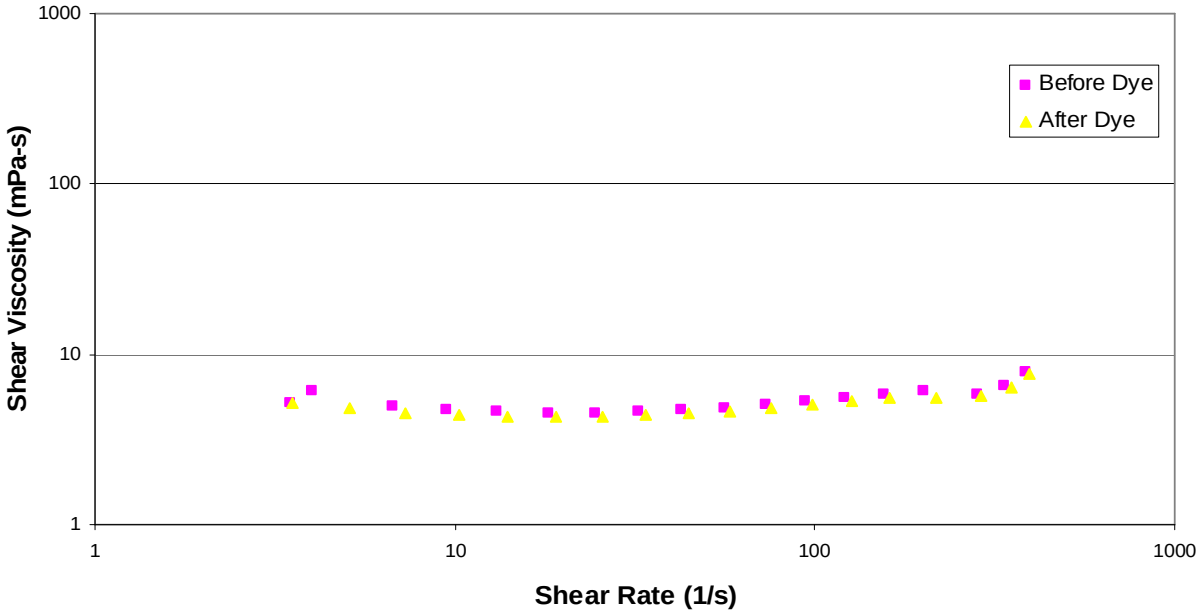

Figure C.3: Viscosity as a function of shear rate for 300K PEO at 20°C

Similarly, as seen from Figures C.2, and C.3, the addition of the food dye showed very little, if no effect, on the shear viscosities of both the 80 wt.% glycerin and the 300K PEO solutions. The slight decrease in shear viscosity with the dyed 80 wt.% glycerin solution may be due to the fact that the weight percentage of water was slightly increased by the addition of the food dye (comprised primarily of water), thus decreasing the

relative concentration of glycerin and thus, lowering the shear viscosity by a minute amount. In any case, this slight decrease will not affect the tests performed as the dyed 80 wt.% glycerin solution still shows a substantial increase in shear viscosity over the 50 wt.% glycerin solution and the water, essentially the motivation behind using these test liquids in the first place.

Ideally, extensional viscosity and surface tension measurements of all the liquids should have been taken both before and after food dye addition to examine the effect of the ink on the polymer structure; this however, was not possible due to the lack of an extensional rheometer at time of testing and time constraints. For this reason, it was assumed that if the shear viscosity was not significantly affected, neither would be these additional liquid properties. Thus, based on the above results and assuming the same trends can be applied to the other three dyed test liquids mentioned above, it can be considered justifiable to use this coloring agent to aid spray visualization.

In addition, as mentioned above, phenol red was used to color the Carbopol® solution after it was realized that the ink, due to its acidic nature, significantly affected the polymer structure. As shown in Figure C.4, the addition of phenol red to the Carbopol® solution is shown to have negligible effect on the Carbopol® shear curve.

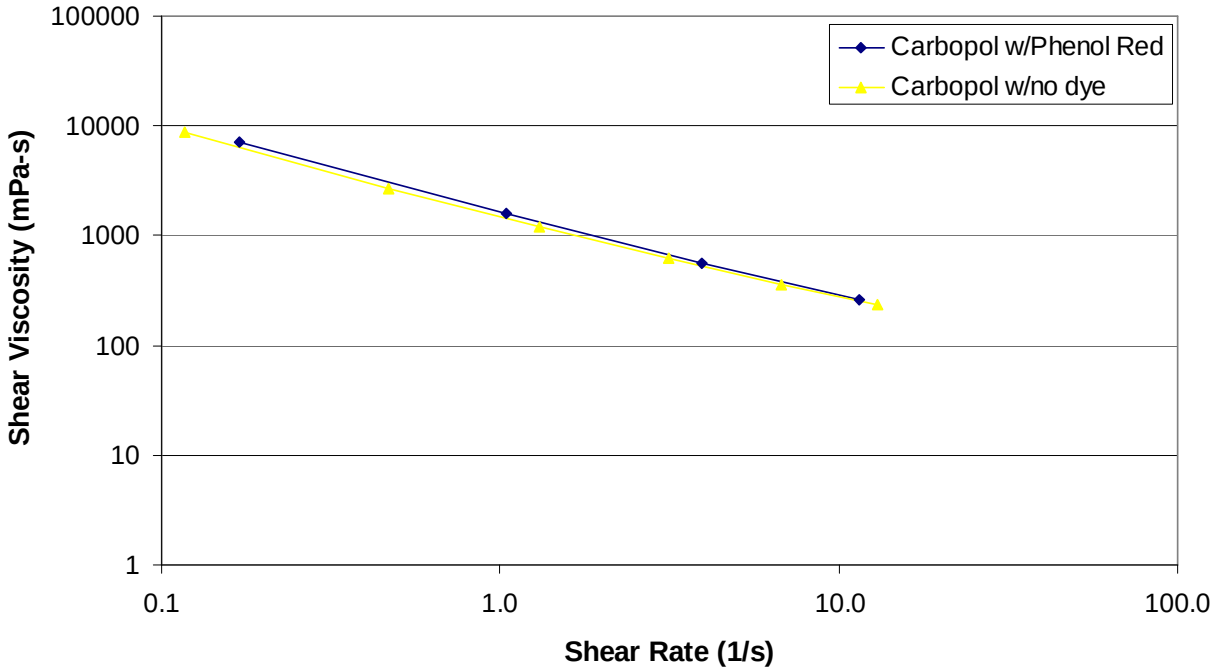

Figure C.4: Viscosity as a function of shear rate for Carbopol® at 20°C

Appendix D

Determination of Droplet Diameter and Velocity

D.1 Droplet Diameter

In order to examine droplet impact behavior, information pertaining to both the droplet diameter and velocity was needed in order to calculate impacting Reynolds and Weber numbers. Using individual images extracted from the cine videos taken with the Phantom high-speed camera and with the development of a MATLAB image processing program, droplet diameters for all test liquids could be determined in a repeatable and consistent manner. Similarly, droplet velocities were determined by examining sequential images extracted from the cine videos using the Phantom software.

The MATLAB code worked as follows: an image (i.e. KELTRACK is used for presentation purposes), having been prior selected and extracted using the Phantom software, is read into MATLAB, shown in Figure D.1.

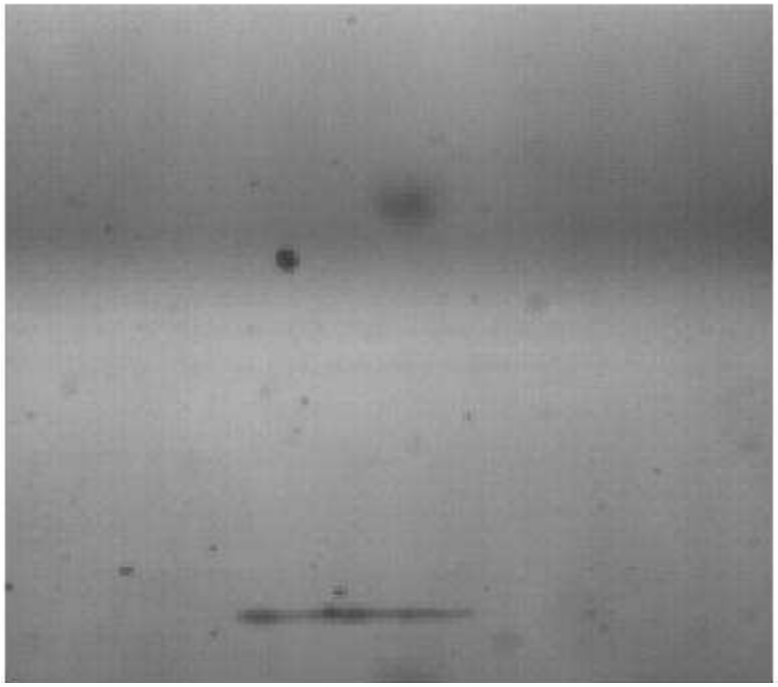

Figure D.1: Original image

This image is then inverted (i.e. black pixels go to white, white to black), shown in Figure D.2, and is used to estimate the background intensity using a morphological estimating function with a certain size structuring element (disk, 10), shown in Figure D.3.

Figure D.2: Inverted image

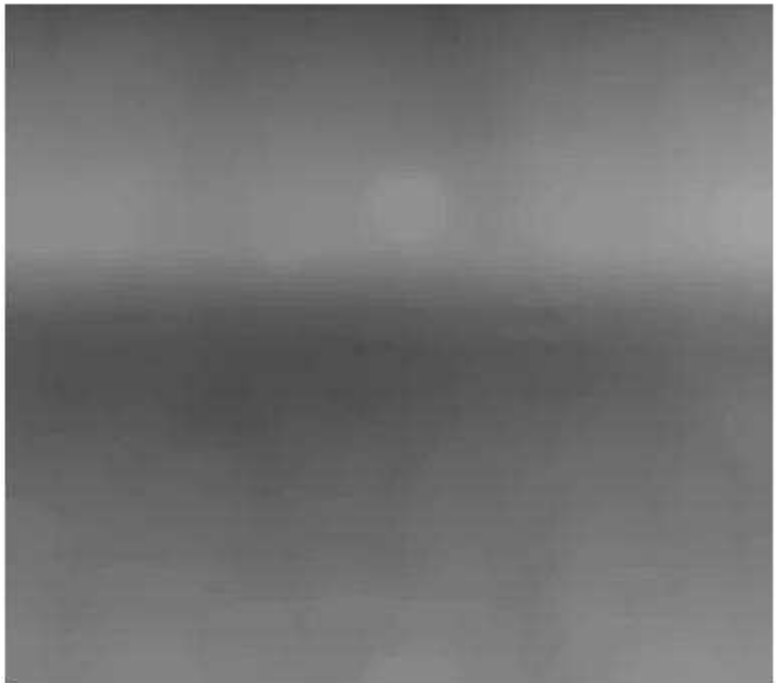

Figure D.3: Background estimation

This background is then subtracted from Figure D.2, yielding Figure D.4.

Figure D.4: Background subtracted from image

The droplet of interest is then selected by using the cursor and dragging a box around it (Figure D.5).

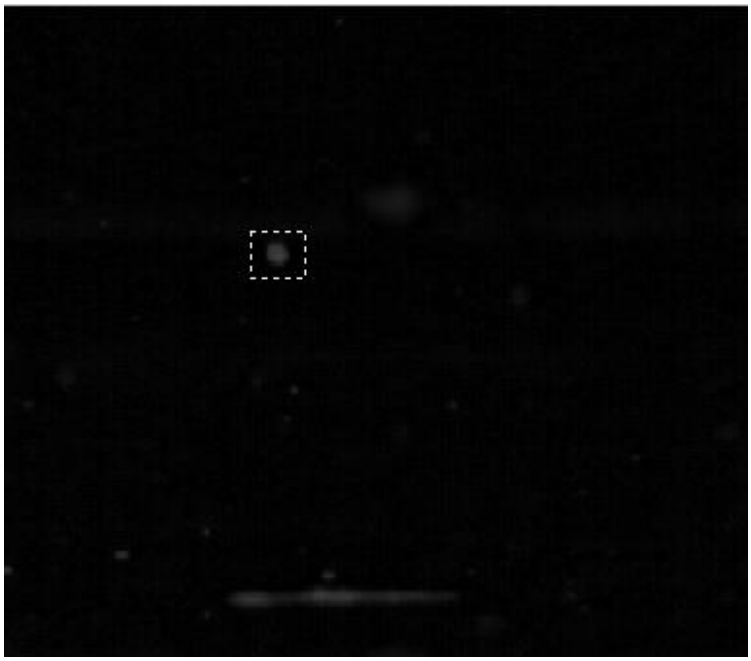

Figure D.5: Cropping droplet of interest

Once the droplet has been selected, the image is inverted once again for thresholding (Figure D.6).

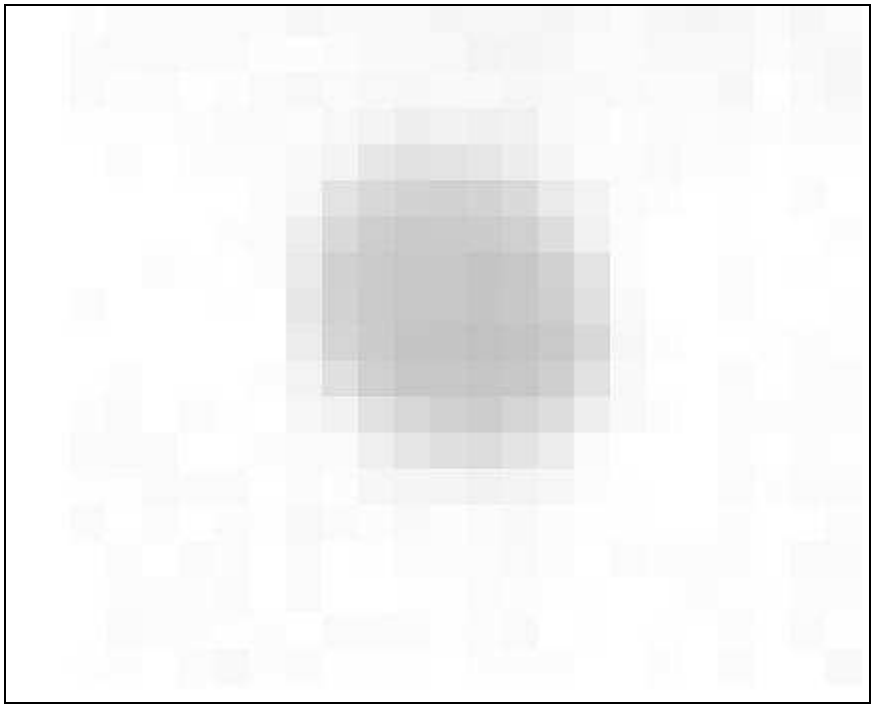

Figure D.6: Inverted droplet

At this time, the maximum and minimum pixel intensities are determined and this pixel intensity range is then remapped to a range between 128 and 255. This is done to ensure that all droplets, regardless of liquid or video illumination, have the same contrast range for thresholding.

A pixel intensity threshold of 205 was then selected by analyzing a minimum of four images for all nine test liquids and selecting the most appropriate threshold. This threshold of 205 was determined primarily by using the Image Tool (Figure D.7) to examine the pixel intensity range of the droplet, but also by examining the image histogram (Figure D.8) and approximating the region where the background ends and the droplet begins.

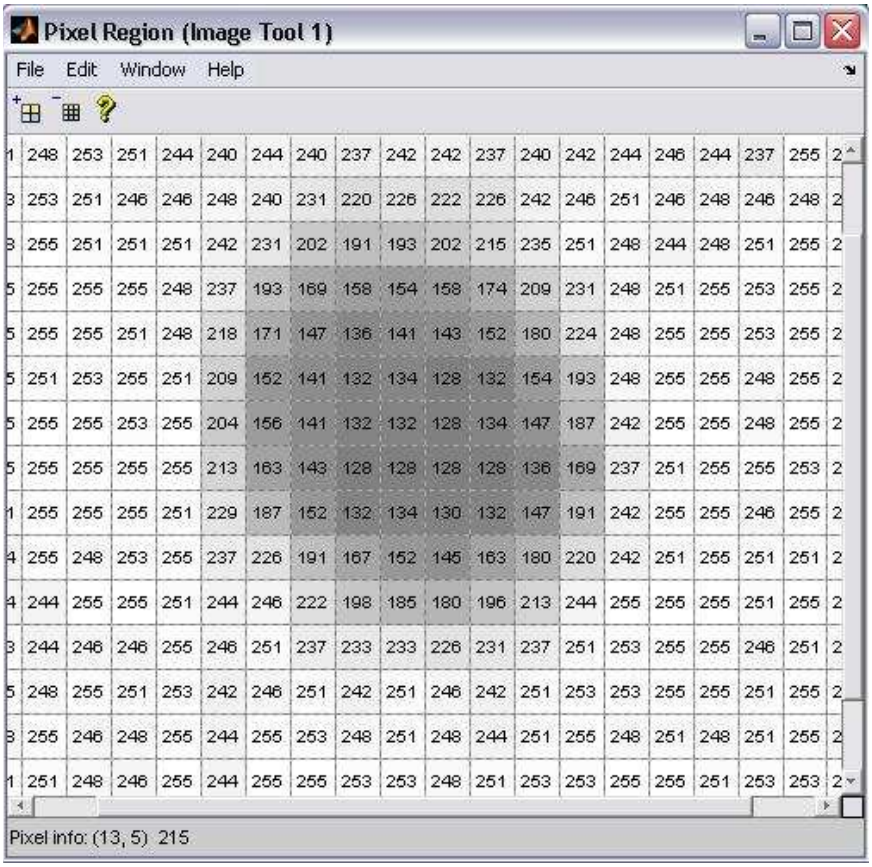

Figure D.7: Pixel intensities for droplets

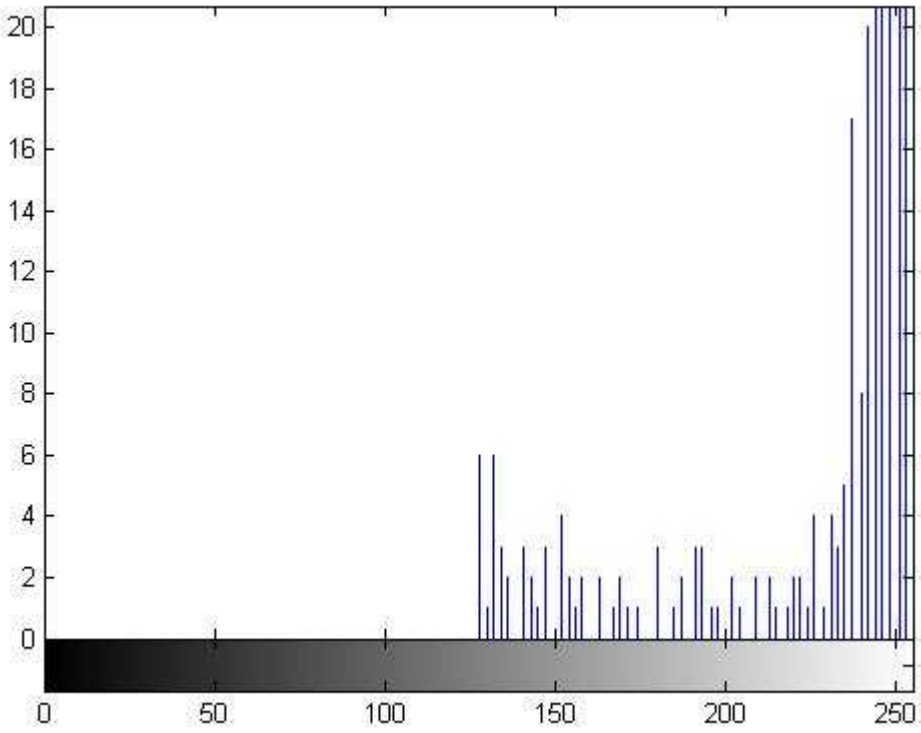

Figure D.8: Image histogram

With the new threshold set, all pixel intensities below this value were converted to black and all above were converted to white. The image was once again inverted (Figure D.9) and the number of white pixels were counted (white area determination).

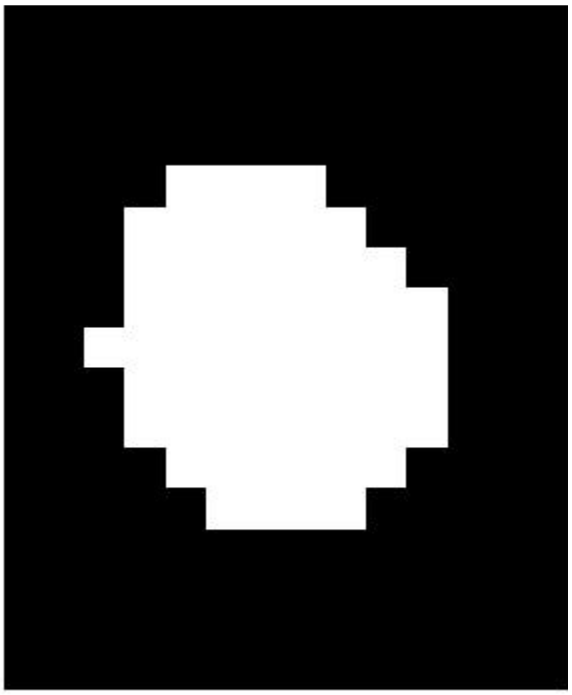

Figure D.9: Inverted droplet

All images were taken at a resolution of 288 x 256 pixels, yielding a total pixel area of 73728 pixels. Using the abovementioned calculated number of white pixels and the total pixel area, a pixel area percentage for the droplet can be obtained. Then, in knowing the exact FOV of the videos, yielding an area in mm^2, the area percentage of white pixels can be used to determine a scaled area of the droplet. By assuming the droplet to be spherical, thus having the frontal area of that of a circle, the diameter of the droplet is approximated and is output to the MATLAB command window.

D.2 Droplet Velocity

Droplet velocities were determined using the Phantom software. As a measure of scale for all videos, an initial cine video was taken encompassing a small nail with a known diameter (1.83mm ± 0.03mm). In opening this video in the Phantom cine viewing window, the scaling for all video analysis could be determined. Firstly, under the dropdown menu **Measure**, the measurement units for distance, velocity, and angle are set

to be in millimeters, meters per second, and degrees, respectively. Next, the **Scaling** dialog box is opened and the nail diameter is input, shown in Figure D.10.

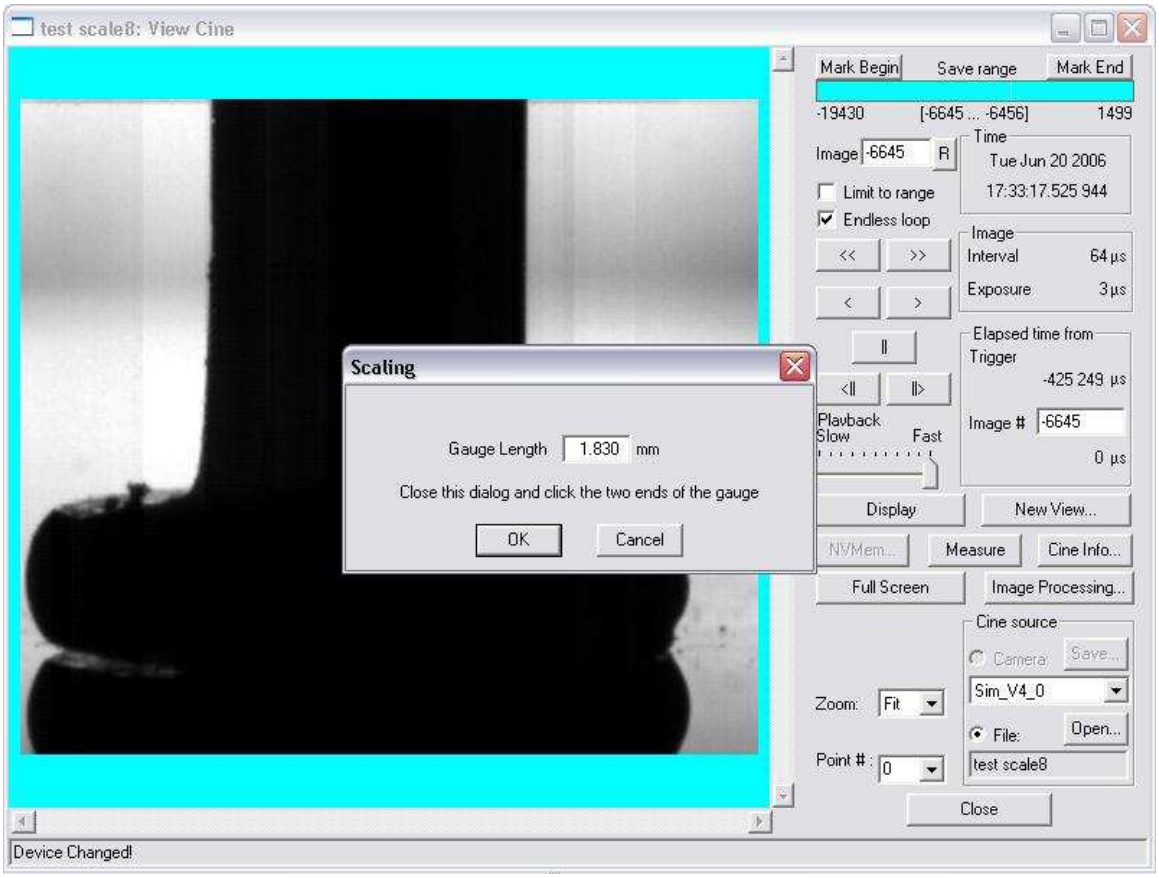

Figure D.10: Setting the video scale

Then, by zooming in on the top right and left corners of the nail and selecting the edge of the nail as precisely as possible, the nail in the video is given a diameter of 1.83mm.

Being that the scale has now been set, droplet velocities can be determined. Once the droplet to be analyzed has been noted in the spray impingement video under examination, select the **Distance and Speed**, **2 points**, option under the **Measure** dropdown. Select a point on the droplet using the cursor, advance the video by one or multiple frames, and then again select the same point on the droplet (in order to minimize error by more precisely selecting the exact same point in both frames, zoom in on the droplet of interest). The droplet velocity is then output on the bottom of the cine viewing window in the status bar, with units of meters per second. Note however that this is the absolute velocity of the droplet (i.e. velocity irrespective of impact angle) and therefore, the impact angle must also be determined in order to be able to break up the impact velocity into its *x* and *y* components.

The impact angle of the droplet is also determined using the Phantom analysis software. In the cine viewing window, select **Angle and Angular Speed** from the **Measure** dropdown menu. The **Angle Measurements** dialog box will appear and then select **2 points + x axis**. The user will then be prompted to select the first reference point of interest. At this time, select a point on the droplet whose impact angle you wish to measure, precisely locating a specific point by zooming in on the droplet. Advance the video by one or two frames and select the same point on the droplet as previously selected, once again by zooming in on the object. The angle is then displayed in the status bar at the bottom of the cine video. This angle is measured however from the horizontal axis placed at the first point of selection in a clockwise motion. Therefore, based on the droplets being analyzed in this analysis, all angles will have a measured impaction angle between 0 and -90° (normal to the surface), as shown in Figure D.11 (please note however that in this figure, two consecutive images have been superimposed on one another for presentation purposes of measurement of impact angle).

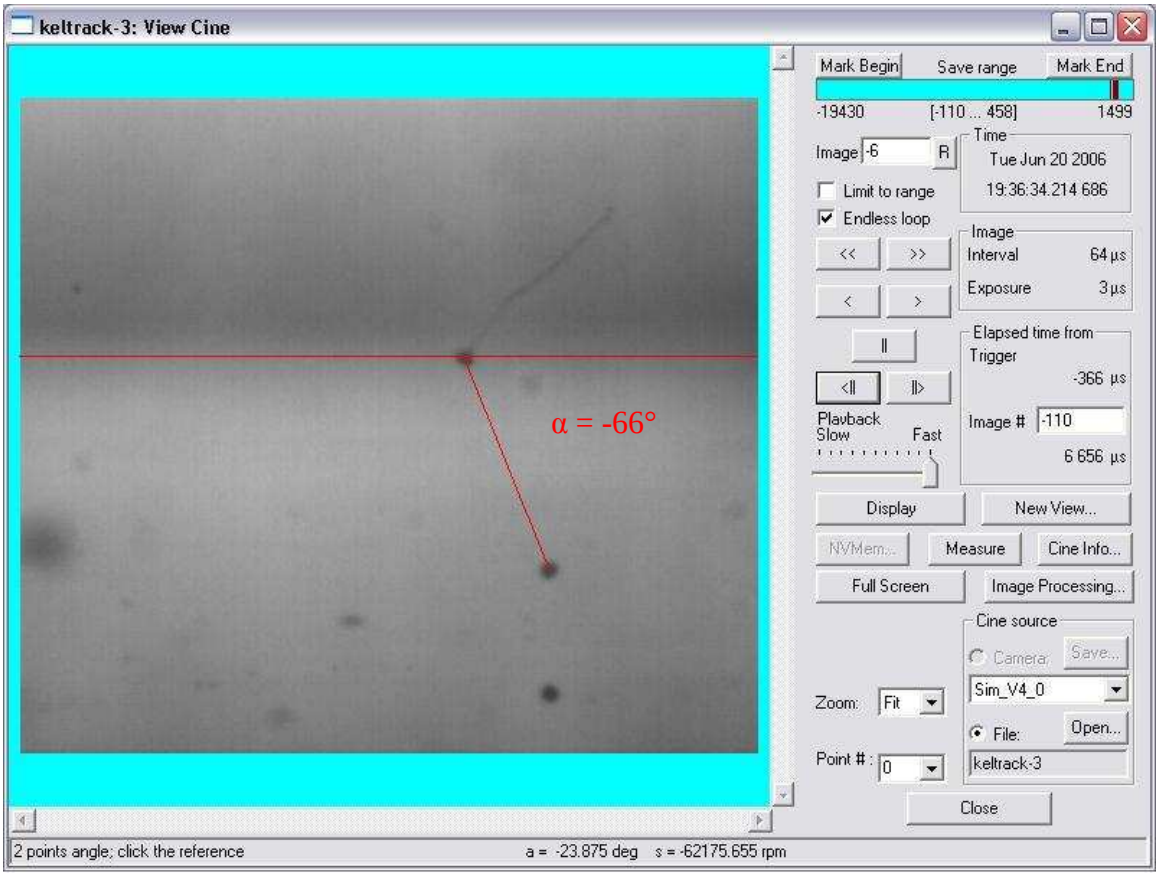

Figure D.11: Determination of impact angle

D.3 Droplet Sizing MATLAB® Code

```
%% Image Processing Code for Determination of Droplet Size
clear all
close all

%Read in the initial image.
D1 = imread('keltrack5.bmp');
figure(1), imshow(D1,'InitialMagnification','fit');

%Invert the image.
D2 = imcomplement(D1);
figure(2), imshow(D2,'InitialMagnification','fit');

%Estimate the background intensity.
background = imopen(D2,strel('disk',10));
figure(3), imshow(background,'InitialMagnification','fit');

%Subtract the background from the inverted image.
D3 = imsubtract(D2,background);
figure(4), imshow(D3,'InitialMagnification','fit');

%Crop the image around the droplet of interest.
D4 = imcrop;
imshow(D4,'InitialMagnification','fit');

%Invert the image a second time.
D5 = imcomplement(D4);
imshow(D5,'InitialMagnification','fit');

%Remap the image intensities to a new range; this is done so all images
%can be analyzed on the same range, with a similar contrast.
low_high = stretchlim(D5);
Dmap = imadjust(D5,stretchlim(D5),[0.5 1]);
low_high = stretchlim(Dmap);
imtool(Dmap,'InitialMagnification','fit');
figure(6), imhist(Dmap);

%Set the threshold level and convert image to black and white.
normthresh = 205/255;
D6 = im2bw(Dmap, normthresh);

%Invert the image for a third time in order to calculate area.
D7 = imcomplement(D6);

%Label the black/white regions and calculate the # of pixels in each
%labeled region.
L = bwlabel(D7);
stats = regionprops(L,'Area');
stats

%Determine the droplet diameter based on image resolution and FOV.
str = stats(1).Area;
totalpixels = 73728; %total # of pixels in 256 x 288 image
percentpixelarea = str/totalpixels; % percentage of white pixels
totalarea = 1.558e-5; %image area in m^2 based on approx. 3.8mm x 4.1mm
FOV
```

```
%this value changed for each set of videos with a slightly different
scale.
droparea = percentpixelarea*totalarea;
diameter = ((4*droparea)/pi)^0.5; %assume area of a circle.
diameter

%Determine the droplet image area based on a higher threshold.
normthresh = 215/255;
D6 = im2bw(Dmap, normthresh);

%Invert the image for a third time in order to calculate area.
D7 = imcomplement(D6);

%Label the black/white regions and calculate the # of pixels in each
%labeled region.
L = bwlabel(D7);
griff = regionprops(L,'Area');
griff

%Determine the droplet diameter based on image resolution and FOV.
str2 = griff(1).Area;

%Determine a skewness level which will determine an approximate number
%relationship between the number of pixels in the original set
threshold
%(under 205) compared to the number of pixels under the higher
threshold of 215.
%This value should be relatively high (i.e. >80%).
skewness=str/str2
```

Appendix E

Spray Label Analysis MATLAB® Code

```
%% Spray Deposition Code for Label Analysis
clear all
close all
clc

%Read in the initial image.
D1 = imread('10mps12psig.bmp');
figure(1), imshow(D1);

%Crop the image to a rectangle specified by the user.
D2 = imcrop(D1);
figure(2), imshow(D2, 'truesize');

%Zoom in on the top left hand pixel of the label. Then hit enter to
continue program after pause.
%Then select the furthest most left edge of the label (i.e. pixel on
outer edge of label).
zoom;
pause
[x,y] = ginput(1);

%Crop the image to a specified size of 1124x650 pixels for all labels.
%All labels were measured to have a width of approximately 1146 pixels.
%By cropping the image 11 pixels from either end, the majority of the
noise on the border is removed.
D3 = imcrop(D2,[x+11 y 1124 650]);

%Threshold the image and convert it to black and white. Then invert it.
H = imcomplement(D3);
normthresh = 165/255;
I = im2bw(H,normthresh);
figure(4), imshow(I,'truesize');
D4 = imcomplement(I); %must be done for bwarea function to work.

%Break up the image into four equally spaced interrogation areas.
D5=imcrop(D4,[0 0 281 650]);
figure(6), imshow(D5,'truesize');
D6=imcrop(D4,[281 0 281 650]);
figure(7), imshow(D6,'truesize');
D7=imcrop(D4,[562 0 281 650]);
figure(8), imshow(D7,'truesize');
D8=imcrop(D4,[843 0 281 650]);
figure(9), imshow(D8,'truesize');

%Calculate the total # of pixels that are FM. Then calculate the total
# of pixels that are FM in each interrogation area.
statstotal = bwarea(D4);
stats1 = bwarea(D5);
stats2 = bwarea(D6);
stats3 = bwarea(D7);
stats4 = bwarea(D8);

%Determine the spray % area covered.
```

```
totalpixels = 730600; %this is based on 1124x650 label for analysis
totalspraypercentage = statstotal/totalpixels*100 %given as a
percentage
totallabelarea = 1313.69; %total label area in mm^2, based on a label
width of 1124x650 pixels, and a dpi of 599
totalspraycoverage = (totalspraypercentage/100)*totallabelarea %in mm^2

%Determine the spray percentage in each of the four interrogation
areas.
area1 = (stats1/statstotal)*100
area2 = (stats2/statstotal)*100
area3 = (stats3/statstotal)*100
area4 = (stats4/statstotal)*100
```